CENTRO DE INVESTIGACIONES
EN OPTICA, A.C.

“AB-INITIO CALCULATION OF TWO-PHOTON ABSORPTION FOR SEMICONDUCTORS”

A thesis submitted in partial fulfillment of the requirements for the degree of Doctor in Science (Optics).

***Student:* Alan Bernal Ramírez**

Advisor: *Dr. Bernardo Mendoza Santoyo*

León · Guanajuato · México
December 2022

Versión final.
Incluye las sugerencias de los sinodales.

B. Mendoza S.

Dr. Bernardo Mendoza Santoyo

"Physics isn't the most important thing. Love is."
RICHARD FEYNMAN

Abstract

A theoretical derivation of two-photon absorption (2PA) from bulk, surface and 2 dimensional (2D) semiconductors, based on the length gauge analysis and the electron density operator, is formulated; the *intraband* $\boldsymbol{r}_i$ part and the *interband* $\boldsymbol{r}_e$ part of the position operator $\boldsymbol{r}$ are properly accounted for. Within the independent particle approximation, the nonlinear third order susceptibility tensor $\chi^{\mathrm{abcd}}(-\omega;-\omega,-\omega,\omega)$ and the two-photon absorption coefficient are calculated, including the scissors correction needed to correct the well-known underestimation of the local-density-approximation band gap. Using time-reversal symmetry, it is shown that the expression for $\chi^{\mathrm{abcd}}(-\omega;-\omega,-\omega,\omega)$ is finite at $\omega = 0$, avoiding nonphysical divergences presented in previous calculations when $\omega \to 0$. *Ab initio* band structure calculations using different pseudopotential schemes that include spin-orbit coupling are used to calculate the 2PA for several semiconductors, and the calculations are compared with available experimental results for photon energies that are below the optical band gap. The TPA results for the chosen bulk semiconductors cover a wide range of wavelengths as well as a wide intensity range, in such a way that depending on the sought application one would be able to chose among the studied materials. For instance, the semiconductors with the biggest absorption could be used as components in flourophores for two-photon excitation microscopy, also these materials could be used in multiphoton microfabrication and lithography technologies. Moreover, the materials with wide band gap could be used for optical power limiting, optical data storage, or two-photon photodynamic therapy technologies. In addition, the 2PA susceptibilities for the following surface structures GaAs-1×1(110):Sb, Si-1×1(111):H and clean GaAs-1×1-110 were calculated, obtaining a spectral range that shows a remarkable widening of bandwidth for GaAs-1×1(110):Sb and Si-1×1(111):H structures compared with the corresponding bulk response, and for clean GaAs-1×1-110 surface the spectral shape shows a resonance in the terahertz region. Finally, we calculated the 2PA susceptibility for the following 2D monochalcogenides materials GeSe, SnSe, SnS and GeS. These materials are commonly used in optoelectronic devices and our study motivates the experimental investigation of 2PA in 2D structures. The 2PA susceptibility of above surfaces and 2D materials is as large as the standard bulk semiconductors, thus opening a myriad of application for 2PA, such as non-invasive terahertz medical applications. In the future, we are going to calculate 2PA for other crystalline structures besides FCC, extending the calculation to more types of semiconductors. In addition to our numerical results presented in this work, the theoretical derivation of 2PA presented in this thesis opens the possibility of the study of other third-order nonlinear optical phenomena. For example, four-wave mixing, Raman scattering, third harmonic generation, and the calculation to the nonlinear third order susceptibility in order to obtain the nonlinear refractive index.

I dedicate this work to my family and my beautiful life partner, Yeshenia.
To my son: I want you to believe deep in your heart that you are capable of achieving anything you put in your mind.

ACKNOWLEDGEMENTS

First of all, I would like to thank Bernardo, for providing guidance and feedback throughout this project, his knowledge and almost religious dedication motivated me to accomplish this thesis.
I extend thanks to my doctoral committee, Dr. Norberto Arzate Plata and Dr. Eden Morales Narváez. Their expediency, comments, and suggestions were invaluable for this work.
I am very grateful to my colleagues and friends at Medusa laboratory, Sean and Ulises. Thank you for your invaluable friendship.
I would like to express a special mention to my colleague and friend Brandon Furey thanks for their pleasant talks and time spent out of CIO.
Me gustaría agradecer especialmente a mis padres y hermanos por su apoyo y amor incondicional, nada hubiera sido posible sin ellos gracias a Mario y Crintina, Aidé, Aldo, Abel y Adán.
Words cannot express my gratitude to Yeshenia.
And finally, I thank everyone who was part of this project and to each of the people who in one way or another were part of my life during the doctorate. Thank you all. This work was supported by Consejo Nacional de Ciencia y Tecnología under Scholarship No. 636376 (A.B.R.).

CONTENTS

List of Figures

List of Tables

1 INTRODUCTION

Outline

Since the development of the two-photon absorption (2PA) theory in 1931 by Maria Göppert-Mayer [7], a new field of research emerged, as she was the first to predict the quantum mechanical process that explains the simultaneous absorption of two photons of the same energy as the impinge to excite a material. These new optical phenomena opened the gate to better understand optical processes and to develop potential technologies based on 2PA. In this sense, there are current technologies related to 2PA phenomena, such as two-photon excitation microscopy [8] and multiphoton microfabrication and lithography [9–11]; also, work on applications such as optical power limiting [12], optical data storage [13, 14], or two-photon photodynamic therapy [15] is being done, as well as research on bioimaging using materials at the nanoscale [16, 17]. For this, it is mandatory to conduct experimental and theoretical research on 2PA phenomena in materials; in particular, the explanation and prediction of the microscopic third-order optical response in materials are theoretical targets.

1.1 Experimental background

Related to the experimental point of view of 2PA, there are diverse factors that contribute to the difficulty in characterizing materials in the nonlinear regime. Third-order nonlinear susceptibility related to 2PA is obtained through the measurement of nonlinear absorption in materials, and several variables are involved in these kinds of experiments, such as laser-pulse duration and repetition rate, peak power, laser coherence, the presence of free carriers, and competition between nonlinear and linear absorption phenomena, which increases the complexity of material characterization. Hence reported values for the 2PA coefficient are only within a narrow region of the light spectrum and are often varied over orders of magnitude [18], and even more, experimental work only reports the 2PA coefficient instead of the imaginary part of third-order 2PA susceptibility; to our knowledge, only

Furey et al. [2] have reported the value of all independent nonzero components of the imaginary part of 2PA susceptibility tensors for GaAs, GaP, and Si in the vicinity of the half band gap for each material. The complex measurement of 2PA third-order susceptibility motivates theoretical investigation of this phenomenon.

1.2 Theoretical background

To theoretically describe nonlinear optical responses at the microscopic scale and, in specific, to describe 2PA, some research has been done. Hutchings and Van Stryland [19] calculated the 2PA coefficient in zinc-blende semiconductors by means of the Kane band structure model; such a calculation is a more comprehensive study than the two- band model used by Aversa *et al.* to describe 2PA [20]. Additionally, Hutchings and Wherrett [21] first calculated the polarization dependence of 2PA by means of the four-band Kane band structure model and later calculated the anisotropy parameter, including the influence of higher conduction bands, by using the Luttinger-Kohn band structure model [22]. The band structure models cited have the disadvantage of being semiempirical approximations and of describing the absorption phenomena in a vicinity near the center of the Brillouin zone, with a limited number of electronic bands. Alternatively, Aversa and Sipe [23] have cemented the formalism to obtain linear and nonlinear optical responses based on the perturbation theory under the length gauge analysis and the electron density operator. This formalism allowed the accurate calculation of nonlinear optical responses, such as the second-harmonic generator (SHG) [24], and they also suggested computing higher-order optical responses. Related to *ab initio* 2PA calculations, to our knowledge, only Murayama and Nakayama [1, 25, 26] have presented *ab initio* full band structure calculations; they presented the two-photon absorption spectra and anisotropy of GaAs, ZnSe, and Si using the density-matrix theory, and nonlocal corrections to the local momentum operator and a correction to the self-energy were presented. These calculations have the disadvantage of presenting apparent unphysical divergences in the infrared regime.

The theoretical derivation of 2PA microscopic susceptibility is presented in this thesis under the *ab initio* perturbative approach in the independent-particle approximation using a full band structure. This work uses the length gauge approximation as the perturbative interaction between materials and light to obtain the imaginary part of the third-order nonlinear susceptibility, which describes third-order nonlinear absorption. The well-known band-gap underestimation in density functional theory with the local-density approximation (DFT-LDA) is corrected at the scissors operator level, and the inclusion of the spin-orbit coupling (SOC) is taken into account. Also, we show that the unphysical divergences are analytically demonstrated to be zero when $\omega \to 0$, which was not considered in previous *ab initio* calculations; moreover, the 2ω and 1ω terms of $\chi^{\mathrm{abcd}}(-\omega; -\omega, -\omega, \omega)$ are analyzed to obtain a complete third-order optical response, where the position matrix elements are distinguished in the *intraband* $\boldsymbol{r}_i$ part and the *interband* $\boldsymbol{r}_e$ part [23, 27, 28]; this differentiation allows us to disregard nonsignificant terms in $\chi^{\mathrm{abcd}}(-\omega; -\omega, -\omega, \omega)$.

1.3 Outline

This thesis is divided into 5 chapters including this introduction. Chapter 2 presents the theoretical derivation of explicit expressions for the nonlinear two-photon absorption (2PA) susceptibility, based on quantum mechanical time-dependent perturbation theory. Chapter 3 presents the theoretical calculated 2PA spectroscopy for several bulk semiconductors in particular for Si, GaAS and GaP, for which a detailed comparison with experimental data is presented, finding that the results from our derived theory compares very well to the experimental spectra. In Chapter 4 we extend the general theory of 2PA susceptibility to the derivation for the nonlinear two-photon absorption surface susceptibility. The theoretical expression is then used to calculate 2PA for three surface structures and four mono-layer materials along with corresponding explanation. Chapter 5 is dedicated to the final conclusions and remarks. Appendix A contains the derivation of the scissored velocity matrix elements necessary to calculate the surface 2PA. Appendix B presents the disclaimer of the paper “Ab initio calculation of two-photon absorption in semiconductors”, by Alan Bernal Ramírez and Bernardo S. Mendoza, published in Physical Review B **106**, 125201 (2022), whose results are used in this thesis. Finally, the complete bibliography is located at the end of the thesis for easy reference.

2 THEORY

Outline

In this chapter, we present the scheme used to calculate the third-order nonlinear response $\chi^{\mathrm{abcd}}(-\omega;-\omega,-\omega,\omega)$ using the length gauge formalism, within the independent-particle approach. Some detail is given, since it is important to distinguish between the so-called *intraband* and *interband* transitions. In the Sec. 2.4, we show all the steps of the perturbation approach taken, and, in particular, we show how through time reversal invariance, the expression for $\chi^{\mathrm{abcd}}(-\omega;-\omega,-\omega,\omega)$ is divergence-free at $\omega=0$. We mention that the expression for $\chi^{\mathrm{abcd}}(-\omega;-\omega,-\omega,\omega)$ presented in Ref. [1] diverges at $\omega=0$.

2.1 Two-photon absorption

The absorption of two photons of the same frequency is characterized through the third-order nonlinear polarization, written as

$$\mathbf{P}(t)=\epsilon_0\chi^{(3)}\mathbf{E}^3(t), \tag{2.1}$$

where the tensorial character of susceptibility $\chi^{(3)}$ is suppressed for convenience, and the perturbing electric field $\mathbf{E}(t)$ is given by

$$\mathbf{E}(t)=\mathbf{E}_+(\omega)e^{-i\tilde{\omega}t}+\mathbf{E}_-(\omega)e^{i\tilde{\omega}t}, \tag{2.2}$$

where $\mathbf{E}_+(\omega)=E(\omega)\hat{\varepsilon}$ and $\mathbf{E}_-(\omega)=E(\omega)\hat{\varepsilon}^*$. Then, $E(\omega)$ gives the magnitude and $\hat{\varepsilon}$ the polarization of the electric field. For linear polarization $\hat{\varepsilon}=\hat{\varepsilon}^*$, but for elliptical polarization, $\hat{\varepsilon}$ will have an opposite helicity to $\hat{\varepsilon}^*$. Also, $\tilde{\omega}=\omega+i\eta$, and $\eta=0^+$ adiabatically switches on the interaction with the electric field. At the end of the calculation, we take $\eta\to 0$. The above field is such that

$\mathbf{E}_+(\omega)e^{-i\tilde{\omega}t}$ induces the absorption of a photon with energy $\hbar\omega$, whereas $\mathbf{E}_-(\omega)e^{i\tilde{\omega}t}$ induces the emission of a photon with energy $\hbar\omega$. Then,

$$\begin{aligned}\mathbf{P}(t) = \epsilon_0\chi^{(3)}\Big(&\mathbf{E}_+(\omega)\mathbf{E}_+(\omega)\mathbf{E}_+(\omega)e^{-i3\tilde{\omega}t} + 3\mathbf{E}_+(\omega)\mathbf{E}_+(\omega)\mathbf{E}_-(\omega)e^{-i\tilde{\omega}t}\\ &+ 3\mathbf{E}_+(\omega)\mathbf{E}_-(\omega)\mathbf{E}_-(\omega)e^{i\tilde{\omega}t} + \mathbf{E}_-(\omega)\mathbf{E}_-(\omega)\mathbf{E}_-(\omega)e^{i3\tilde{\omega}t}\Big),\end{aligned} \tag{2.3}$$

where the two-photon absorption (2PA) is given by

$$\mathbf{P}(t) = 3\epsilon_0\chi^{(3)}\mathbf{E}_+(\omega)\mathbf{E}_+(\omega)\mathbf{E}_-(\omega)e^{-i\tilde{\omega}t}, \tag{2.4}$$

where two photons, each of frequency ω, are simultaneously absorbed through $\mathbf{E}_+(\omega)$, and the resulting polarization oscillates at ω. The above equation leads to

$$P^{\mathrm{a}}(\omega) = 3\epsilon_0\chi^{\mathrm{abcd}}(-\omega;-\omega,-\omega,\omega)E_+^{\mathrm{b}}(\omega)E_+^{\mathrm{c}}(\omega)E_-^{\mathrm{d}}(\omega), \tag{2.5}$$

with $\chi^{\mathrm{abcd}}(-\omega;-\omega,-\omega,\omega)$ being the degenerate third-order nonlinear optical susceptibility tensor describing a polarization density response at the same frequency as the incident frequency. [29] It describes 2PA whose units are those of m^2/V^2. The roman superscripts denote Cartesian components, where we use the Einstein convention for repeated indices, and ϵ_0 is the vacuum permittivity.

2.2 Perturbation approach

In order to derive the analytic expression for the 2PA susceptibility of Eq. (2.5), we assume that electrons may be described through an independent-particle approximation, although we do allow for many-body effects through an effective Hamiltonian that depends on all the occupied states, as in density functional theory. The electrons interact with an electromagnetic field, which we assume is a classical field. Thus, we describe quantum mechanical matter interacting with classical fields. We neglect the local fields and excitonic effects [30], and we write the one-electron Hamiltonian

$$\hat{H}(t) = \hat{H}_0 + \hat{\mathcal{H}}(t) \tag{2.6}$$

as the sum of an unperturbed effective time-independent Hamiltonian $\hat{H}_0$ that describes the interaction of an electron with the crystalline lattice and its effective interaction with the other electrons, as well as an interaction Hamiltonian $\hat{\mathcal{H}}(t)$, which describes the interaction of the electron with a time-dependent electromagnetic field. We mention that $\hat{H}_0$ includes the scissors operator that allows for the energy correction of the pseudopotentials gap E_{gap} to the experimental energy of the gap $E_{\texttt{expt}}$ [5]. We describe the state of the system through the one electron density operator $\hat{\rho}$, with which we can calculate the expectation value of any single-particle observable $\hat{\mathcal{O}}$ as $\langle\hat{\mathcal{O}}\rangle = \mathrm{Tr}(\hat{\rho}\hat{\mathcal{O}})$ with Tr denoting the trace. Within the interaction picture (I), the density operator evolves in time due to the interaction Hamiltonian according to

$$i\hbar\frac{d}{dt}\hat{\rho}_I(t) = [\hat{\mathcal{H}}_I(t), \hat{\rho}_I(t)], \tag{2.7}$$

while the operators that correspond to all observables evolve through $\hat{H}_0$ according to

$$\hat{\mathcal{O}}_I(t) = \hat{U}^\dagger(t)\hat{\mathcal{O}}(t)\hat{U}(t), \tag{2.8}$$

where $\hat{\mathcal{O}}(t)$ is the same observable in the Schrödinger picture, given by $\hat{\mathcal{O}}(0)$ for operators that do not depend explicitly on time, and

$$\hat{U}(t) = \exp(-i\hat{H}_0 t/\hbar) \tag{2.9}$$

is the nonperturbed unitary time-evolution operator. Assuming the field is turned on adiabatically, we may integrate (2.7) to yield

$$\hat{\rho}_I(t) = \hat{\rho}_{I0} + \frac{1}{i\hbar}\int_{-\infty}^{t} dt'[\hat{\mathcal{H}}_I(t'), \hat{\rho}_I(t')], \tag{2.10}$$

where $\hat{\rho}_{I0}$ is the unperturbed, time-independent equilibrium density matrix. We look for the standard perturbation series solution, $\hat{\rho}_I(t) = \hat{\rho}_{I0} + \hat{\rho}_I^{(1)}(t) + \hat{\rho}_I^{(2)}(t) + \ldots$, where the superscript denotes the order (power) with which each term depends on perturbation $\hat{\mathcal{H}}_I(t)$. The $(N+1)$-th order solution is given as

$$\hat{\rho}_I^{(N+1)}(t) = \frac{1}{i\hbar}\int_{-\infty}^{t} dt'[\hat{\mathcal{H}}_I(t'), \hat{\rho}_I^{(N)}], \quad N \geq 0, \tag{2.11}$$

where $\hat{\rho}_I^{(N)}$ is the density matrix of the previous order perturbation term. For 2PA, $N+1=3$, and then, we need to know $\hat{\rho}_I^{(0)}$, $\hat{\rho}_I^{(1)}$, and $\hat{\rho}_I^{(2)}$ to obtain $\hat{\rho}_I^{(3)}$.

We take our system as a solid described by a nonperturbed periodic Hamiltonian, whose eigenfunctions are Bloch states, $|m\boldsymbol{k}\rangle$, characterized by a band index m and a crystal momentum $\boldsymbol{k}$. For $\hat{\mathcal{H}}_I(t)$, we take the interaction with an electromagnetic field with a wavelength much larger than the crystal unit cell dimension. Thus, electronic transitions due to this interaction are vertical; that is, they conserve $\boldsymbol{k}$. Taking the matrix elements between Bloch states of Eq. (2.8), we obtain

$$\langle n\boldsymbol{k}|\hat{\mathcal{O}}_I|m\boldsymbol{k}\rangle \equiv \mathcal{O}_{I,nm}(\boldsymbol{k},t) = e^{i\omega_{nm}(\boldsymbol{k})t}\langle n\boldsymbol{k}|\hat{\mathcal{O}}|m\boldsymbol{k}\rangle = e^{i\omega_{nm}(\boldsymbol{k})t}\mathcal{O}_{nm}(\boldsymbol{k},t), \tag{2.12}$$

where $\omega_{nm}(\boldsymbol{k}) \equiv \omega_n(\boldsymbol{k}) - \omega_m(\boldsymbol{k})$ and $E_n(\boldsymbol{k}) = \hbar\omega_n(\boldsymbol{k})$ are the unperturbed energy eigenvalues corresponding to the stationary Schrödinger's equation $\hat{H}_0\,|n\boldsymbol{k}\rangle = E_n(\boldsymbol{k})\,|n\boldsymbol{k}\rangle$, where the Bloch states $|n\boldsymbol{k}\rangle$ are chosen so that $\langle \boldsymbol{r}|n\boldsymbol{k}\rangle = u_{n\boldsymbol{k}}(\boldsymbol{r})e^{i\boldsymbol{k}\cdot\boldsymbol{r}}$, with $u_{n\boldsymbol{k}}(\boldsymbol{r})$ being cell periodic and $\langle n\boldsymbol{k}|m\boldsymbol{k}'\rangle = \delta_{nm}\delta(\boldsymbol{k}-\boldsymbol{k}')$.

Within the dipole approximation, the interaction Hamiltonian in the length gauge is given by [5]

$$\hat{\mathcal{H}}_I(t) = -e\hat{\boldsymbol{r}}_I(t)\cdot\boldsymbol{E}(t), \tag{2.13}$$

where $\hat{\boldsymbol{r}}_I(t) = \hat{U}_0^\dagger(t)\hat{\boldsymbol{r}}U(t)$ is the position operator of the electron at time t, and from Eq. (2.2), $\boldsymbol{E}(t) = \boldsymbol{E}_\pm(\omega)e^{\mp i\tilde{\omega}t}$, the time dependent perturbing classical electric field that, as explained in the previous section, induces two-photon absorption through the correct choices of $\boldsymbol{E}(t)$, as given in Eq. (2.5). Then, from Eqs. (2.11) and (2.12) we obtain

$$\rho_{I,nm}^{(N+1)}(\boldsymbol{k},t) = \frac{ie}{\hbar}\int_{-\infty}^{t} dt' e^{i\omega_{nm}(\boldsymbol{k})t'}\,\langle n\mathbf{k}|[\hat{\boldsymbol{r}}, \hat{\rho}^{(N)}]|m\boldsymbol{k}\rangle\cdot\boldsymbol{E}(t'), \tag{2.14}$$

where it is convenient to represent the position operator in the coordinate space $\hat{\boldsymbol{r}} \to \boldsymbol{r}$ when calculating its *interband* matrix elements, and in the reciprocal space $\hat{\boldsymbol{r}} \to i\nabla_{\boldsymbol{k}}$ when calculating its *intraband* matrix elements, so that following Refs. [23,31,32], the matrix elements of $\mathbf{r}$ are split between the *intraband* ($\mathbf{r}_i$) and *interband* ($\mathbf{r}_e$) parts, where $\mathbf{r} = \mathbf{r}_i + \mathbf{r}_e$ and

$$\langle n\boldsymbol{k}|\,\hat{\mathbf{r}}_i\,|m\boldsymbol{k}'\rangle = \delta_{nm}\left[\delta(\boldsymbol{k}-\boldsymbol{k}')\boldsymbol{\xi}_{nn}(\boldsymbol{k}) + i\nabla_{\boldsymbol{k}}\delta(\boldsymbol{k}-\boldsymbol{k}')\right], \tag{2.15}$$

$$\langle n\boldsymbol{k}|\,\hat{\mathbf{r}}_e\,|m\boldsymbol{k}'\rangle = (1-\delta_{nm})\delta(\boldsymbol{k}-\boldsymbol{k}')\boldsymbol{\xi}_{nm}(\boldsymbol{k}), \tag{2.16}$$

with

$$\boldsymbol{\xi}_{nm}(\boldsymbol{k}) \equiv i\frac{(2\pi)^3}{\Omega}\int_\Omega d\mathbf{r}\, u^*_{n\boldsymbol{k}}(\mathbf{r})\nabla_{\boldsymbol{k}} u_{m\boldsymbol{k}}(\mathbf{r}) \tag{2.17}$$

being the Berry connection, where Ω is the unit cell volume. The well-known commutator

$$\hat{\boldsymbol{v}} = \dot{\hat{\boldsymbol{r}}} = \frac{1}{i\hbar}[\hat{\boldsymbol{r}}, \hat{H}_0] \tag{2.18}$$

allows us to write the interband matrix element as

$$\boldsymbol{r}_{nm}(\boldsymbol{k}) = \frac{\boldsymbol{v}_{nm}(\boldsymbol{k})}{i\omega_{nm}(\boldsymbol{k})} \quad (n \neq m), \tag{2.19}$$

where $\hat{\boldsymbol{v}}$ is the velocity operator related to the momentum operator by $\hat{\boldsymbol{p}} = \mathrm{m}\hat{\boldsymbol{v}}$, with m being the mass of the electron. For $\boldsymbol{r}_e$, we obtain that

$$\begin{aligned}\langle n\boldsymbol{k}|\,[\hat{r}^{\mathrm{a}}, \hat{\rho}^{(N)}(t)]\,|m\boldsymbol{k}\rangle &= \sum_{\ell\neq m,n}\left(r^{\mathrm{a}}_{n\ell}(\boldsymbol{k})\rho^{(N)}_{\ell m}(\boldsymbol{k},t) - \rho^{(N)}_{n\ell}(\boldsymbol{k},t)r^{\mathrm{a}}_{\ell m}(\boldsymbol{k})\right)(1-\delta_{nm})\\ &\equiv R^{\mathrm{a},(N)}_{nm}(\boldsymbol{k},t),\end{aligned} \tag{2.20}$$

where we used the closure relationship $\sum_n |n\boldsymbol{k}\rangle\langle n\boldsymbol{k}| = 1$. When $\mathbf{r}_i$ appears in commutators, we use

$$\langle n\boldsymbol{k}|\,[\hat{r}^{\mathrm{a}}_i, \hat{\rho}^{(N)}(t)]\,|m\boldsymbol{k}\rangle = i\rho^{(N)}_{nm;k^{\mathrm{a}}}(\boldsymbol{k},t) \equiv R^{\mathrm{a},(N)}_{i,nm}(\boldsymbol{k},t) \tag{2.21}$$

with

$$\rho^{(N)}_{nm;\boldsymbol{k}}(\boldsymbol{k},t) = \nabla_{\boldsymbol{k}}\rho^{(N)}_{nm}(\boldsymbol{k},t) - i\rho^{(N)}_{nm}(\boldsymbol{k},t)\left(\boldsymbol{\xi}_{nn}(\boldsymbol{k}) - \boldsymbol{\xi}_{mm}(\boldsymbol{k})\right), \tag{2.22}$$

where "$;\boldsymbol{k}$" denotes the generalized derivative with respect to $\boldsymbol{k}$, and $\rho^{(N)}_{nm}(\boldsymbol{k},t)$ could be replaced by any function.

From Eq. (2.14), we obtain

$$\rho^{(N+1)}_{I,nm}(\boldsymbol{k},t) = \frac{ie}{\hbar}\int_{-\infty}^{t} dt' e^{i(\omega_{nm\boldsymbol{k}}\pm\tilde{\omega}_p)t'}\left[\,R^{\mathrm{b},(N)}_{nm}(\boldsymbol{k},t') + R^{\mathrm{b},(N)}_{i,nm}(\boldsymbol{k},t')\right]E^{\mathrm{b}}_{\mp}(\omega_p), \tag{2.23}$$

where sublabel p is a tag to keep track of the frequency ω_p that belongs to the Cartesian direction b.

The perturbation series is generated by the unperturbed density operator

$$\langle n\boldsymbol{k}|\hat{\rho}^{(0)}|m\boldsymbol{k}\rangle = \delta_{nm}f(\hbar\omega_n(\boldsymbol{k})) \equiv f_n(\boldsymbol{k}), \tag{2.24}$$

with $f_n(\boldsymbol{k})$ being the Fermi-Dirac distribution; for a clean, cold semiconductor $f_n(\boldsymbol{k}) = 1$ when n is a valence (v) or occupied band, and zero when n is a conduction (c) or empty band. This defines the distribution functions $f_n(\boldsymbol{k})$ in reciprocal space, one for each band. Also, following Ref. [23], we can readily show that

$$\langle n\boldsymbol{k}|[\hat{\mathbf{r}}, \hat{\rho}^{(0)}]|m\boldsymbol{k}\rangle = f_{mn}(\boldsymbol{k})\boldsymbol{r}_{nm}(\boldsymbol{k}) + i\delta_{nm}\nabla_{\boldsymbol{k}} f_n(\boldsymbol{k}), \tag{2.25}$$

where $f_{nm}(\boldsymbol{k}) = f_n(\boldsymbol{k}) - f_m(\boldsymbol{k})$. For a clean, cold semiconductor, $\nabla_{\boldsymbol{k}} f_n(\boldsymbol{k}) = 0$, and thus, there are no intraband contributions to the optical response; however, this term is finite for metallic systems and gives rise to their low-frequency optical behavior through the so-called Drude Tensor [33]. From Eq. (2.20), $R^{\mathrm{a},(0)}_{nm}(\boldsymbol{k},t) = f_{mn}(\boldsymbol{k})r^{\mathrm{a}}_{nm}(\boldsymbol{k})(1-\delta_{nm})$, and from Eq. (2.21), $R^{\mathrm{a},(0)}_{i,nm}(\boldsymbol{k},t) = 0$, which when used in Eq. (2.23), leads to $\rho^{(1)}_{I,nm}(\boldsymbol{k},t) = e^{i\omega_{nm}(\boldsymbol{k})t}\rho^{(1)}_{nm}(\pm\omega_p, t)$, where

$$\rho^{(1)}_{nm}(\pm\omega_p, \boldsymbol{k}, t) = B^{\mathrm{b}}_{nm}(\pm\omega_p, \boldsymbol{k})(1-\delta_{nm})E^{\mathrm{b}}_{\mp}(\omega_p)e^{\pm i\tilde{\omega}_p t}, \tag{2.26}$$

with

$$B^{\mathrm{b}}_{nm}(\pm\omega_p, \boldsymbol{k}) = \frac{e}{\hbar}\frac{f_{mn}(\boldsymbol{k})r^{\mathrm{b}}_{nm}(\boldsymbol{k})}{\omega_{nm}(\boldsymbol{k}) \pm \tilde{\omega}_p}. \tag{2.27}$$

For the linear response, $\rho^{(1)}_{nm}(-\omega_p, \boldsymbol{k}, t)$ ($\rho^{(1)}_{nm}(+\omega_p, \boldsymbol{k}, t)$) would lead to the absorption (emission) of a photon with energy $\hbar\omega_p$.

We proceed with the second-order terms, and from Eq. (2.20) and (2.21), we obtain

$$R^{\mathrm{b}(1)}_{e,nm}(\boldsymbol{k},t) = \frac{e}{\hbar}\sum_{\ell\neq m,n}\left(r^{\mathrm{b}}_{n\ell}(\boldsymbol{k})B^{\mathrm{c}}_{\ell m}(\boldsymbol{k},\pm\omega_q) - B^{\mathrm{c}}_{n\ell}(\boldsymbol{k},\pm\omega_q)r^{\mathrm{b}}_{\ell m}(\boldsymbol{k})\right)(1-\delta_{nm})E^{\mathrm{c}}_{\mp\omega_q}e^{\pm i\tilde{\omega}_q t} \tag{2.28}$$

and

$$R^{\mathrm{b}(1)}_{i,nm}(\boldsymbol{k},t) = \frac{ie}{\hbar}B^{\mathrm{c}}_{nm;k^{\mathrm{b}}}(\boldsymbol{k},\pm\omega_q)(1-\delta_{nm})E^{\mathrm{c}}_{\mp\omega_q}e^{\pm i\tilde{\omega}_q t}, \tag{2.29}$$

where we use ω_q to differentiate it from ω_p, since it is associated to the electrical field along the c direction. From Eq. (2.23), we obtain that $\rho^{(2)}_{I,nm}(\boldsymbol{k},t) = e^{i\omega_{nm}(\boldsymbol{k})t}\rho^{(2)}_{nm}(\pm\tilde{\omega}_p \pm \tilde{\omega}_q, \boldsymbol{k}, t)$, where $\rho^{(2)}_{nm}(\pm\omega_p \pm \omega_q, \boldsymbol{k}, t) = \rho^{(2)}_{nm}(\pm\omega_p \pm \omega_q, \boldsymbol{k})E^{\mathrm{b}}_{\mp p}E^{\mathrm{c}}_{\mp q}e^{i(\pm\tilde{\omega}_p \pm\tilde{\omega}_q)t}$, with

$$\begin{aligned}\rho^{(2)}_{nm}(\pm\omega_p \pm \omega_q, \boldsymbol{k}) = \frac{e^2}{\hbar^2}\frac{1}{\omega_{nm\boldsymbol{k}} \pm \tilde{\omega}_p \pm \tilde{\omega}_q}\Bigg[&iB^{\mathrm{c}}_{nm;k^{\mathrm{b}}}(\pm\omega_q, \boldsymbol{k}) \\ &+ \sum_{\ell\neq nm}\left(r^{\mathrm{b}}_{n\ell}B^{\mathrm{c}}_{\ell m}(\pm\omega_q, \boldsymbol{k}) - B^{\mathrm{c}}_{n\ell}(\pm\omega_q, \boldsymbol{k})r^{\mathrm{b}}_{\ell m}\right)\Bigg](1-\delta_{nm}).\end{aligned} \tag{2.30}$$

We mention that the above expression would lead to second-harmonic generation by taking $-\omega_q = -\omega_p = -\omega$ [5,34].

Finally, we proceed with the third-order nonlinear response. Then, from Eqs. (2.20) and (2.21)

$$R^{\mathrm{d}(2)}_{e,nm}(\boldsymbol{k},t) = \sum_{\ell\neq nm}\left(r^{\mathrm{d}}_{n\ell}(\boldsymbol{k})\rho^{(2)}_{\ell m}(\pm\omega_p \pm \omega_q, \boldsymbol{k}) - \rho^{(2)}_{n\ell}(\pm\omega_p \pm \omega_q, \boldsymbol{k})r^{\mathrm{d}}_{\ell m}(\boldsymbol{k})\right)E^{\mathrm{b}}_{\mp p}E^{\mathrm{c}}_{\mp q}e^{i(\pm\omega_p \pm\omega_q - i\eta)t}(1-\delta_{nm}), \tag{2.31}$$

and

$$R^{\mathrm{d}(2)}_{i,nm}(\boldsymbol{k},t) = i\rho^{(2)}_{nm;k^{\mathrm{d}}}(\pm\omega_p \pm \omega_q, \boldsymbol{k}) E^{\mathrm{b}}_{\mp p} E^{\mathrm{c}}_{\mp q} (1-\delta_{nm}) e^{i(\pm\omega_p \pm\omega_q - i\eta)t}. \tag{2.32}$$

Then, from Eq. (2.23) $\rho^{(3)}_{I,nm}(\boldsymbol{k},t) = e^{i\omega^{\Sigma}_{nm\boldsymbol{k}}t}\rho^{(3)}_{nm}(\pm\omega_p \pm \omega_q \pm \omega_s, \boldsymbol{k}, t)$, where

$$\rho^{(3)}_{nm}(\pm\omega_p \pm \omega_q \pm \omega_s, \boldsymbol{k}, t) = \rho^{(3)}_{nm}(\pm\omega_p \pm \omega_q \pm \omega_s, \boldsymbol{k}) E^{\mathrm{d}}_{\mp s} E^{\mathrm{b}}_{\mp p} E^{\mathrm{c}}_{\mp q} e^{i(\pm\omega_p \pm\omega_q \pm\omega_s - i\eta)t}, \tag{2.33}$$

and

$$\begin{aligned}\rho^{(3)}_{nm}(\pm\omega_p \pm \omega_q \pm \omega_s, \boldsymbol{k}) = \frac{e}{\hbar}\Big[\sum_{\ell\neq nm} \Big(r^{\mathrm{d}}_{n\ell}(\boldsymbol{k}) \rho^{(2)}_{\ell m}(\pm\omega_p \pm \omega_q, \boldsymbol{k}) - \rho^{(2)}_{n\ell}(\pm\omega_p \pm \omega_q, \boldsymbol{k}) r^{\mathrm{d}}_{\ell m}(\boldsymbol{k}) \Big) \\ + i\rho^{(2)}_{nm;k^{\mathrm{d}}}(\pm\omega_p \pm \omega_q, \boldsymbol{k}) \Big] \frac{1-\delta_{nm}}{\omega_{nm}(\boldsymbol{k}) \pm \tilde{\omega}_p \pm \tilde{\omega}_q \pm \tilde{\omega}_s},\end{aligned} \tag{2.34}$$

where now, ω_s is associated with the Cartesian direction d of the electric field.

From Eq. (2.5), 2PA is given by this combination of fields, $E^{\mathrm{b}}_{+}(\omega)E^{\mathrm{c}}_{+}(\omega)E^{\mathrm{d}}_{-}(\omega)$, which in turn implies that $\omega_p = -\omega$, $\omega_q = -\omega$, and $\omega_s = \omega$, so that from Eq. (2.34), the third-order density matrix that describes 2PA is given by

$$\rho^{(3)}_{nm}(-\omega, \boldsymbol{k}) = \frac{e}{\hbar} \sum_{\ell\neq mn} \Big[\Big(r^{\mathrm{d}}_{n\ell}(\boldsymbol{k}) \rho^{(2)}_{\ell m}(-2\omega, \boldsymbol{k}) - \rho^{(2)}_{n\ell}(-2\omega, \boldsymbol{k}) r^{\mathrm{d}}_{\ell m}(\boldsymbol{k}) \Big) + i\rho^{(2)}_{nm;k^{\mathrm{d}}}(-2\omega, \boldsymbol{k}) \Big] \frac{1-\delta_{nm}}{\omega_{nm}(\boldsymbol{k}) - \omega}, \tag{2.35}$$

where, from Eq. (2.30),

$$\rho^{(2)}_{nm}(-2\omega, \boldsymbol{k}) = \frac{e^2}{\hbar^2} \frac{\mathcal{G}^{\mathrm{bc}}_{nm}(-\omega, \boldsymbol{k})}{\omega_{nm}(\boldsymbol{k}) - 2\tilde{\omega}} \tag{2.36}$$

with

$$\mathcal{G}^{\mathrm{bc}}_{nm}(-\omega, \boldsymbol{k}) = iB^{\mathrm{c}}_{nm;k^{\mathrm{b}}}(-\omega, \boldsymbol{k}) + \sum_{\ell\neq mn} \Big(r^{\mathrm{b}}_{n\ell}(\boldsymbol{k}) B^{\mathrm{c}}_{\ell m}(-\omega, \boldsymbol{k}) - B^{\mathrm{c}}_{n\ell}(-\omega, \boldsymbol{k}) r^{\mathrm{b}}_{\ell m}(\boldsymbol{k}) \Big), \tag{2.37}$$

and $B^{\mathrm{c}}_{nm}(-\omega, \boldsymbol{k})$ is given in Eq. (2.27), with the generalized derivative $;\boldsymbol{k}$ in Eq. (2.22).

2.3 Two-photon absorption susceptibility

To obtain the 2PA response, we look for the expectation value of the macroscopic polarization density $\boldsymbol{P}$, whose time derivative yields the current density, $\boldsymbol{J}$, as

$$\frac{\partial}{\partial t}\boldsymbol{P} = \boldsymbol{J} = \frac{e}{\Omega}\mathrm{Tr}\left(\hat{\boldsymbol{v}}\hat{\rho}^{(3)}(t)\right). \tag{2.38}$$

where Ω is the volume of the unit cell, from Eq. (2.33),

$$\boldsymbol{P}(\omega) = \frac{ie}{\omega} \int \frac{d\boldsymbol{k}}{8\pi^3} \sum_{mn} \boldsymbol{v}_{mn}(\boldsymbol{k}) \rho^{(3)}_{nm}(-\omega, \boldsymbol{k}) E^{\mathrm{b}}_{+} E^{\mathrm{c}}_{+} E^{\mathrm{d}}_{-}, \tag{2.39}$$

and using Eq. (2.5), we obtain that

$$\chi^{\mathrm{abcd}}(-\omega;-\omega,-\omega,\omega) = \frac{ie^2}{\hbar\omega}\int\frac{d\boldsymbol{k}}{8\pi^3}\sum_{m\neq n} v^{\mathrm{a}}_{mn}(\boldsymbol{k})\Big[\sum_{\ell\neq mn}\Big(r^{\mathrm{d}}_{n\ell}(\boldsymbol{k})\rho^{(2)}_{\ell m}(-2\omega,\boldsymbol{k}) - \rho^{(2)}_{n\ell}(-2\omega,\boldsymbol{k})r^{\mathrm{d}}_{\ell m}(\boldsymbol{k})\Big) + i\rho^{(2)}_{nm;k^{\mathrm{d}}}(-2\omega,\boldsymbol{k})\Big]\frac{1}{\omega_{nm}(\boldsymbol{k})-\tilde{\omega}} \tag{2.40}$$

is the third-order nonlinear susceptibility that describes 2PA in semiconductors; integration over $\boldsymbol{k}$ is over the Brillouin Zone (BZ). In Sec. 2.4, we show how to obtain explicit expressions for $\chi^{\mathrm{abcd}}(-\omega;-\omega,-\omega,\omega)$ that we use to calculate 2PA. Those expressions are composed of terms that resonate when the external frequency of the incoming beam of light $\hbar\omega \geq E_{\mathrm{gap}}$ or $\hbar\omega \geq E_{\mathrm{gap}}/2$, where E_{gap} is the energy gap of the semiconductor. We mention that the factor of 3 that appears in Eq. (2.5) is the factor of 3 that is given in the numerator of Eq. (3.1) as obtained in Ref. [2].

In this work, we are mainly interested in 2PA for $E_{\mathrm{gap}}/2 \leq \hbar\omega < E_{\mathrm{gap}}$, which, according to Sec. (2.4), would correspond to the 2ω expression for $\chi^{\mathrm{abcd}}(-\omega;-\omega,-\omega,\omega)$ given in Eq. (2.62), (2.66), (2.76), and (2.79), so that

$$\mathrm{Im}[\chi^{\mathrm{abcd}}_{2\omega}] = \frac{\pi e^4}{\hbar^3}\int\frac{d\boldsymbol{k}}{8\pi^3}\sum_{vc}\Bigg(\frac{16\Delta^{\mathrm{d}}_{cv}(\boldsymbol{k})\mathrm{Im}[r^{\mathrm{c}}_{cv;k^{\mathrm{b}}}(\boldsymbol{k})v^{\mathrm{a}}_{vc}(\boldsymbol{k})]}{\omega^4_{cv}(\boldsymbol{k})} - \frac{32\Delta^{\mathrm{b}}_{cv}(\boldsymbol{k})\Delta^{\mathrm{d}}_{cv}(\boldsymbol{k})\mathrm{Im}[v^{\mathrm{a}}_{vc}(\boldsymbol{k})r^{\mathrm{c}}_{cv}(\boldsymbol{k})]}{\omega^5_{cv}(\boldsymbol{k})} - \frac{8\mathrm{Im}[v^{\mathrm{a}}_{vc;k^{\mathrm{d}}}(\boldsymbol{k})r^{\mathrm{c}}_{cv;k^{\mathrm{b}}}(\boldsymbol{k})]}{\omega^3_{cv}(\boldsymbol{k})} + \frac{16\Delta^{\mathrm{b}}_{cv}(\boldsymbol{k})\mathrm{Im}[r^{\mathrm{c}}_{cv}(\boldsymbol{k})v^{\mathrm{a}}_{vc;k^{\mathrm{d}}}(\boldsymbol{k})]}{\omega^4_{cv}(\boldsymbol{k})}\Bigg)\delta(\omega_{cv}(\boldsymbol{k})-2\omega), \tag{2.41}$$

where we have suppressed the argument $(-\omega;-\omega,-\omega,\omega)$ to save space; the generalized derivatives of $v^a_{nm;k^b}(\boldsymbol{k})$ and $r^a_{nm;k^b}(\boldsymbol{k})$ are given in Eqs. (2.50) and (2.51), respectively. It is worth mentioning that the expression involves transitions only from valence (v) to conduction (c) states. Indeed, as it turns out, the terms of $\chi^{\mathrm{abcd}}_{2\omega}(-\omega;-\omega,-\omega,\omega)$ that have summations that involve three and four energy states (see Sec. 2.4), are 10^5 times smaller than what Eq. (2.41) gives; therefore, we could ignore them throughout this work. Finally, as described in Ref. [5], the scissors operator would lead to the following modifications:

$$\omega^{\Sigma}_n(\boldsymbol{k}) = \omega^{\mathrm{LDA}}_n(\boldsymbol{k}) + (1-f_n(\boldsymbol{k}))\Sigma, \tag{2.42}$$

with $\omega^{\mathrm{LDA}}_n(\boldsymbol{k})$ being the LDA energy of band n at point $\boldsymbol{k}$, and Σ the energy or "scissors shift" required to obtain the experimental energy gap of the semiconductor in question. Also,

$$\boldsymbol{v}^{\Sigma}_{nm}(\boldsymbol{k}) = \boldsymbol{v}^{\mathrm{LDA}}_{nm}(\boldsymbol{k}) + i\Sigma f_{nm}(\boldsymbol{k})\boldsymbol{r}_{nm}(\boldsymbol{k}) \tag{2.43}$$

gives the scissor shift to the velocity matrix elements.

To summarize the procedure used to obtain the 2PA susceptibility, in Fig. 2.1 we show a tree diagram of the electronic density $\rho^{(N)}_{i,e}$ and its intraband $\boldsymbol{r}_i$ and interband $\boldsymbol{r}_e$ contributions to every order in the perturbation scheme presented above. As mentioned before, for a clean cold semiconductor, $\nabla_{\boldsymbol{k}} f_n(\boldsymbol{k}) = 0$, and there are no intraband contributions to $\rho^{(1)}_i$, for which the left branch of Fig. 2.1 vanishes; however, this branch is finite for a metal. On the other hand, the right branch of the tree is always finite for both semiconductors and metals. As shown in Sec. 3, the contributions

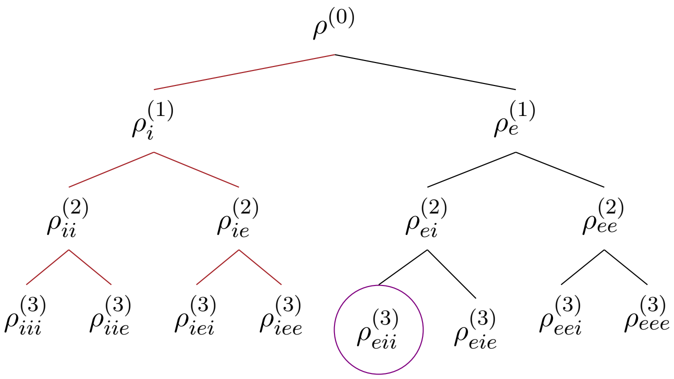

Figure 2.1: Tree diagram of the electronic density $\rho_{i,e}^{(N)}$ and its intraband $\boldsymbol{r}_i$ and interband $\boldsymbol{r}_e$ contributions to every order in the perturbation scheme presented in Sec. 2.2. The $\rho_{eii}^{(3)}$, $\rho_{eie}^{(3)}$, $\rho_{eei}^{(3)}$ and $\rho_{eee}^{(3)}$ are given in Eqs. (2.93)-(2.96), respectively. The only contributing term to 2PA susceptibility of the tree is term $\rho_{eii}^{(3)}$, circled in violet, which is composed of only two-band transitions. The $\rho_{eie}^{(3)}$, $\rho_{eei}^{(3)}$ and $\rho_{eee}^{(3)}$ branches are related to three- and four-band transitions, and although finite, they are negligible, as shown in Sec. 3 . For a semiconductor, the left branch of the tree in red vanishes identically.

from three bands and four bands to 2PA are negligible with respect to the contributions from two bands, that is why the only contributing term to 2PA susceptibility is the branch circled in the tree, and it corresponds to $\rho_{eii}^{(3)}$, which involves "one" contribution from $\boldsymbol{r}_e$ and "two" from $\boldsymbol{r}_i$. Indeed, in Eqs. (2.93)-(2.96) we identify each of the contributions of the last right branch of Fig. 2.1 given by $\rho_{eii}^{(3)}$, $\rho_{eie}^{(3)}$, $\rho_{eei}^{(3)}$ and $\rho_{eee}^{(3)}$. As we show in Sec. 3 $\rho_{eii}^{(3)}$ dominates the 2PA response for the semiconductors used in this work.

2.4 Derivation of $\chi^{\mathbf{abcd}}(-\omega;-\omega,-\omega,\omega)$

In this section, we give the main steps to obtain the 2PA $\chi^{\mathrm{abcd}}(-\omega;-\omega,-\omega,\omega)$ susceptibility of Eq. (2.40). Using Eq. (2.36) and the chain rule,

$$\rho^{(2)}_{nm;k^{\mathrm{d}}}(-2\omega,\boldsymbol{k}) = \frac{e^2}{\hbar^2}\left(\frac{\mathcal{G}^{\mathrm{bc}}_{nm;k^{\mathrm{d}}}(-\omega,\boldsymbol{k})}{\omega_{nm}(\boldsymbol{k})-2\tilde{\omega}} + \mathcal{G}^{\mathrm{bc}}_{nm}(-\omega,\boldsymbol{k})\left(\frac{1}{\omega_{nm}(\boldsymbol{k})-2\tilde{\omega}}\right)_{;k^{\mathrm{d}}}\right), \tag{2.44}$$

which from Eq. (2.40) leads to

$$\begin{aligned}\chi^{\mathrm{abcd}}(-\omega;-\omega,-\omega,\omega) &= \frac{ie^4}{\hbar^3\tilde{\omega}}\int\frac{d\boldsymbol{k}}{8\pi^3}\sum_{m\neq n\neq \ell}\Bigg(\frac{v^{\mathrm{a}}_{mn}(\boldsymbol{k})r^{\mathrm{d}}_{n\ell}(\boldsymbol{k})\mathcal{G}^{\mathrm{bc}}_{\ell m}(-\omega,\boldsymbol{k})}{\omega_{\ell m}(\boldsymbol{k})-2\tilde{\omega}} - \frac{v^{\mathrm{a}}_{mn}(\boldsymbol{k})\mathcal{G}^{\mathrm{bc}}_{n\ell}(-\omega,\boldsymbol{k})r^{\mathrm{d}}_{\ell m}(\boldsymbol{k})}{\omega_{n\ell}(\boldsymbol{k})-2\tilde{\omega}}\\ &+ i\frac{v^{\mathrm{a}}_{mn}(\boldsymbol{k})\mathcal{G}^{\mathrm{bc}}_{nm;k^{\mathrm{d}}}(-\omega,\boldsymbol{k})}{\omega_{nm}(\boldsymbol{k})-2\tilde{\omega}} + iv^{\mathrm{a}}_{mn}(\boldsymbol{k})\mathcal{G}^{\mathrm{bc}}_{nm}(-\omega,\boldsymbol{k})\left(\frac{1}{\omega_{nm}(\boldsymbol{k})-2\tilde{\omega}}\right)_{;k^d}\Bigg)\frac{1}{\omega_{nm}(\boldsymbol{k})-\tilde{\omega}}.\end{aligned} \tag{2.45}$$

Integrating by parts the last term of above equation, we obtain that

$$\chi^{\mathrm{abcd}}(-\omega;-\omega,-\omega,\omega) = \frac{ie^4}{\hbar^3\tilde{\omega}}\int\frac{d\boldsymbol{k}}{8\pi^3}\sum_{m\neq n}\Bigg[\Bigg(-i\frac{v^{\mathrm{a}}_{mn;k^{\mathrm{d}}}(\boldsymbol{k})\mathcal{G}^{\mathrm{bc}}_{nm}(-\omega,\boldsymbol{k})}{(\omega_{nm}(\boldsymbol{k})-2\tilde{\omega})(\omega_{nm}(\boldsymbol{k})-\tilde{\omega})}\|_1 \tag{2.46}$$

$$\begin{aligned}&+ i\frac{v^{\mathrm{a}}_{mn}(\boldsymbol{k})\Delta^{\mathrm{d}}_{nm}(\boldsymbol{k})\mathcal{G}^{\mathrm{bc}}_{nm}(-\omega,\boldsymbol{k})}{(\omega_{nm}(\boldsymbol{k})-2\tilde{\omega})(\omega_{nm}(\boldsymbol{k})-\tilde{\omega})^2}\|_2\Bigg)\\ &+ \sum_{\ell\neq m,n}\Bigg(-\frac{v^{\mathrm{a}}_{mn}(\boldsymbol{k})r^{\mathrm{d}}_{n\ell}(\boldsymbol{k})\mathcal{G}^{\mathrm{bc}}_{\ell m}(-\omega,\boldsymbol{k})}{(\omega_{\ell m}(\boldsymbol{k})-2\tilde{\omega})(\omega_{nm}(\boldsymbol{k})-\tilde{\omega})}\|_3 + \frac{v^{\mathrm{a}}_{mn}(\boldsymbol{k})r^{\mathrm{d}}_{\ell m}(\boldsymbol{k})\mathcal{G}^{\mathrm{bc}}_{n\ell}(-\omega,\boldsymbol{k})}{(\omega_{n\ell}(\boldsymbol{k})-2\tilde{\omega})(\omega_{nm}(\boldsymbol{k})-\tilde{\omega})}\|_4\Bigg)\Bigg],\end{aligned} \tag{2.47}$$

where we have labeled the four terms from 1 to 4 and used the fact that [5]

$$\omega_{m;k^{\mathrm{a}}}(\boldsymbol{k}) = v^{\mathrm{a}}_{mm}(\boldsymbol{k}) \tag{2.48}$$

is the velocity of band m, and we defined

$$\Delta^{\mathrm{a}}_{mn}(\boldsymbol{k}) \equiv v^{\mathrm{a}}_{mm}(\boldsymbol{k}) - v^{\mathrm{a}}_{nn}(\boldsymbol{k}). \tag{2.49}$$

From Eq. (2.19),

$$v^{\mathrm{a}}_{nm;k^{\mathrm{b}}} = i\Delta^{\mathrm{b}}_{nm}r^{\mathrm{a}}_{nm} + i\omega_{nm}r^{\mathrm{a}}_{nm;k^b}, \tag{2.50}$$

where [23, 34]

$$r^{\mathrm{b}}_{nm;k^{\mathrm{a}}} = \frac{r^{\mathrm{a}}_{nm}\Delta^{\mathrm{b}}_{mn} + r^{\mathrm{b}}_{nm}\Delta^{\mathrm{a}}_{mn}}{\omega_{nm}} + \frac{i}{\omega_{nm}}\sum_{\ell\neq m,n}\Big(\omega_{\ell m}r^{\mathrm{a}}_{n\ell}r^{\mathrm{b}}_{\ell m} - \omega_{n\ell}r^{\mathrm{b}}_{n\ell}r^{\mathrm{a}}_{\ell m}\Big). \tag{2.51}$$

Apparently, Eq. (2.46) diverges as ω goes to zero; however, in what follows, this divergence will be shown to cancel out by invoking time-reversal symmetry (TRS) [6]. To show the mathematical steps involved in reducing Eq. (2.46) into a $1/\omega$-divergent-less expression, we take as an example its second term, χ^{abcd}_2 (omitting the ω arguments), and write

$$\chi^{\mathrm{abcd}}_2 = -\frac{e^4}{\hbar^3\tilde{\omega}}\int\frac{d\boldsymbol{k}}{8\pi^3}\sum_{m\neq n}\frac{v^{\mathrm{a}}_{mn}(\boldsymbol{k})\Delta^{\mathrm{d}}_{nm}(\boldsymbol{k})\mathcal{G}^{\mathrm{bc}}_{nm}(-\omega,\boldsymbol{k})}{(\omega_{nm}(\boldsymbol{k})-2\tilde{\omega})(\omega_{nm}(\boldsymbol{k})-\tilde{\omega})^2}, \tag{2.52}$$

where from Eqs. (2.27) and (2.37), we obtain that

$$\mathcal{G}^{\mathrm{bc}}_{nm} = \frac{i f_{mn} r^{\mathrm{c}}_{nm;k^{\mathrm{b}}}}{\omega_{nm} - \tilde{\omega}} - \frac{i f_{mn} r^{\mathrm{c}}_{nm} \Delta^{\mathrm{b}}_{nm}}{(\omega_{nm} - \tilde{\omega})^2} + \sum_{\ell \neq mn} \Big(\frac{f_{m\ell} r^{\mathrm{c}}_{\ell m} r^{\mathrm{b}}_{n\ell}}{\omega_{\ell m} - \tilde{\omega}} - \frac{f_{\ell n} r^{\mathrm{c}}_{n\ell} r^{\mathrm{b}}_{\ell m}}{\omega_{n\ell} - \tilde{\omega}} \Big), \tag{2.53}$$

where we omitted the $(-\omega, \boldsymbol{k})$ and $(\boldsymbol{k})$ arguments to save space. After substituting Eq. (2.53) into (2.52), we split the result into three terms and perform a partial fraction expansion on ω, for each of the three terms. For the first term, we obtain that

$$\chi^{\mathrm{abcd}}_{2,1} \propto \frac{1}{\tilde{\omega}(\omega_{nm} - 2\tilde{\omega})(\omega_{nm} - \tilde{\omega})^3} \equiv \tilde{W}^{(2,1)}_{nm} = \frac{1}{\omega^4_{nm}\tilde{\omega}} + W^{(2,1)}_{nm,\omega} + W^{(2,1)}_{nm,2\omega}, \tag{2.54}$$

where

$$W^{(2,1)}_{nm,\omega} = -\frac{7}{\omega^4_{nm}(\omega_{nm} - \tilde{\omega})} - \frac{3}{\omega^3_{nm}(\omega_{nm} - \tilde{\omega})^2} - \frac{1}{\omega^2_{nm}(\omega_{nm} - \tilde{\omega})^3}, \tag{2.55}$$

and

$$W^{(2,1)}_{nm,2\omega} = \frac{16}{\omega^4_{nm}(\omega_{nm} - 2\tilde{\omega})}. \tag{2.56}$$

In Eq. (2.54), the $1/\tilde{\omega}$ divergent term is isolated from the rest of the nondivergent $\tilde{\omega}$ and $2\tilde{\omega}$ terms given in $W^{(2,1)}_{nm,\omega}$ and $W^{(2,1)}_{nm,2\omega}$, respectively. Using the TRS relations shown in Table 2.1, we obtain that

$$\begin{aligned}
\chi^{\mathrm{abcd}}_{2,1} &= -i\frac{e^4}{\hbar^3} \int_{\boldsymbol{k}>0} \frac{d\boldsymbol{k}}{8\pi^3} \sum_{m\neq n} f_{mn}(\boldsymbol{k}) \tilde{W}^{(2,1)}_{nm}(\boldsymbol{k}) \Big(r^{\mathrm{c}}_{nm;k^{\mathrm{b}}}(\boldsymbol{k}) v^{\mathrm{a}}_{mn}(\boldsymbol{k}) \Delta^{\mathrm{d}}_{nm}(\boldsymbol{k}) + r^{\mathrm{c}}_{nm;k^{\mathrm{b}}}(-\boldsymbol{k}) v^{\mathrm{a}}_{mn}(-\boldsymbol{k}) \Delta^{\mathrm{d}}_{nm}(-\boldsymbol{k}) \Big) \\
&= \frac{e^4}{\hbar^3} \int \frac{d\boldsymbol{k}}{8\pi^3} \sum_{m\neq n} f_{mn}(\boldsymbol{k}) \tilde{W}^{(2,1)}_{nm}(\boldsymbol{k}) \Delta^{\mathrm{d}}_{nm}(\boldsymbol{k}) \mathrm{Im}[r^{\mathrm{c}}_{nm;k^{\mathrm{b}}}(\boldsymbol{k}) v^{\mathrm{a}}_{mn}(\boldsymbol{k})],
\end{aligned} \tag{2.57}$$

and using $\sum_{mn} \mathcal{F}_{mn} = \sum_{m<n} (\mathcal{F}_{mn} + \mathcal{F}_{nm})$, the above equation is converted into

$$\chi^{\mathrm{abcd}}_{2,1} = \frac{e^4}{\hbar^3} \int \frac{d\boldsymbol{k}}{8\pi^3} \sum_{m<n} f_{mn}(\boldsymbol{k}) \Delta^{\mathrm{d}}_{nm}(\boldsymbol{k}) \mathrm{Im}[r^{\mathrm{c}}_{nm;k^{\mathrm{b}}}(\boldsymbol{k}) v^{\mathrm{a}}_{mn}(\boldsymbol{k})] (\tilde{W}^{(2,1)}_{nm}(\boldsymbol{k}) - \tilde{W}^{(2,1)}_{mn}(\boldsymbol{k})), \tag{2.58}$$

where we used the fact that $\mathcal{O}_{nm} = \mathcal{O}^*_{mn}$, with $\hat{\mathcal{O}}$ being a Hermitian operator, and that $\mathrm{Im}[z^*] = -\mathrm{Im}[z]$. From Eq. (2.54)

$$\begin{aligned}
\tilde{W}^{(2,1)}_{nm} - \tilde{W}^{(2,1)}_{mn} &= W^{(2,1)}_{nm,\omega} + W^{(2,1)}_{nm,2\omega} + \frac{1}{\omega^4_{nm}\omega} - W^{(2,1)}_{mn,\omega} - W^{(2,1)}_{mn,2\omega} - \frac{1}{\omega^4_{mn}\omega} \\
&= W^{(2,1)}_{nm,\omega} + W^{(2,1)}_{nm,2\omega} - W^{(2,1)}_{mn,\omega} - W^{(2,1)}_{mn,2\omega},
\end{aligned} \tag{2.59}$$

since $\omega^4_{nm} = \omega^4_{mn}$, and therefore, the divergent $1/\omega$ cancels out due to TRS. Thus,

$$\chi^{\mathrm{abcd}}_{2,1} = \frac{e^4}{\hbar^3} \int \frac{d\boldsymbol{k}}{8\pi^3} \sum_{vc} \Delta^{\mathrm{d}}_{cv}(\boldsymbol{k}) \mathrm{Im}[r^{\mathrm{c}}_{cv;k^{\mathrm{b}}}(\boldsymbol{k}) v^{\mathrm{a}}_{vc}(\boldsymbol{k})] (W^{(2,1)}_{cv,\omega}(\boldsymbol{k}) - W^{(2,1)}_{vc,\omega}(\boldsymbol{k}) + W^{(2,1)}_{cv,2\omega}(\boldsymbol{k}) - W^{(2,1)}_{vc,2\omega}(\boldsymbol{k})), \tag{2.60}$$

$$\begin{aligned}
\omega_{nm}(-\boldsymbol{k}) &= \omega_{nm}(\boldsymbol{k}),\\
r^{\mathrm{a}}_{nm}(-\boldsymbol{k}) &= r^{\mathrm{a}}_{mn}(\boldsymbol{k})\\
r^{\mathrm{a}}_{nm}(-\boldsymbol{k})_{;k^{\mathrm{b}}} &= -r^{\mathrm{a}}_{mn}(\boldsymbol{k})_{;k^{\mathrm{b}}}\\
v^{\mathrm{a}}_{mn}(-\boldsymbol{k}) &= -v^{\mathrm{a}}_{nm}(\boldsymbol{k})\\
v^{\mathrm{a}}_{mn}(-\boldsymbol{k})_{;k^{\mathrm{b}}} &= v^{\mathrm{a}}_{nm}(\boldsymbol{k})_{;k^{\mathrm{b}}}\\
\Delta^{a}_{nm}(-\boldsymbol{k}) &= -\Delta^{a}_{nm}(\boldsymbol{k})
\end{aligned}$$

Table 2.1: Relations obtained from time-Reversal symmetry [6].

since $m < n$ implies from $f_{mn}(\boldsymbol{k})$ that $m = v$ and $n = c$, with v and c being valence and conduction states, respectively. We see that $\chi^{\mathrm{abcd}}_{2,1}$ could be split into 1ω and 2ω terms, as follows,

$$\chi^{\mathrm{abcd}}_{2,1,p\omega} = \frac{e^4}{\hbar^3}\int \frac{d\boldsymbol{k}}{8\pi^3}\sum_{vc}\Delta^{\mathrm{d}}_{cv}(\boldsymbol{k})\mathrm{Im}[r^{\mathrm{c}}_{cv;k^{\mathrm{b}}}(\boldsymbol{k})v^{\mathrm{a}}_{vc}(\boldsymbol{k})](W^{(2,1)}_{cv,p\omega}(\boldsymbol{k}) - W^{(2,1)}_{vc,p\omega}(\boldsymbol{k})), \tag{2.61}$$

where $p = 1, 2$ and $\chi^{\mathrm{abcd}}_{2,1} = \chi^{\mathrm{abcd}}_{2,1,\omega} + \chi^{\mathrm{abcd}}_{2,1,2\omega}$.

Since we are mainly interested in 2PA for photon energies below the gap, we focus on the 2ω term. Then, taking $\eta \to 0$ upon $W^{(2,1)}_{vc,2\omega}(\boldsymbol{k})$ leads to a nonresonant denominator, and from $W^{(2,1)}_{cv,2\omega}(\boldsymbol{k})$, we obtain

$$\mathrm{Im}[\chi^{\mathrm{abcd}}_{2,1,2\omega}] = \frac{\pi e^4}{\hbar^3}\int \frac{d\boldsymbol{k}}{8\pi^3}\sum_{vc}\frac{16\Delta^{\mathrm{d}}_{cv}(\boldsymbol{k})\mathrm{Im}[r^{\mathrm{c}}_{cv;k^{\mathrm{b}}}(\boldsymbol{k})v^{\mathrm{a}}_{vc}(\boldsymbol{k})]}{\omega^4_{cv}(\boldsymbol{k})}\delta(\omega_{cv}(\boldsymbol{k}) - 2\omega), \tag{2.62}$$

which is a closed expression that can be readily evaluated, and through its Kramers-Kroning transformation, the real part of $\chi^{\mathrm{abcd}}_{2,1,2\omega}$ could be calculated.

Using the above procedure, we obtain that

$$\chi^{\mathrm{abcd}}_{2,2,p\omega} = -\frac{e^4}{\hbar^3}\int \frac{d\boldsymbol{k}}{8\pi^3}\sum_{vc}\Delta^{\mathrm{b}}_{cv}(\boldsymbol{k})\Delta^{\mathrm{d}}_{cv}(\boldsymbol{k})\mathrm{Im}[v^{\mathrm{a}}_{vc}(\boldsymbol{k})r^{\mathrm{c}}_{cv}(\boldsymbol{k})]\Big(W^{(2,2)}_{cv,p\omega}(\boldsymbol{k}) + W^{(2,2)}_{vc,p\omega}(\boldsymbol{k})\Big), \tag{2.63}$$

with

$$W^{(2,2)}_{nm,\omega} = -\frac{15}{\omega^5_{nm}(\omega_{nm} - \omega)} - \frac{7}{\omega^4_{nm}(\omega_{nm} - \omega)^2} - \frac{3}{\omega^3_{nm}(\omega_{nm} - \omega)^3} - \frac{1}{\omega^2_{nm}(\omega_{nm} - \omega)^4}, \tag{2.64}$$

and

$$W^{(2,2)}_{nm,2\omega} = \frac{32}{\omega^5_{nm}(\omega_{nm} - 2\omega)}. \tag{2.65}$$

The 2ω term is given by

$$\mathrm{Im}[\chi^{\mathrm{abcd}}_{2,2,2\omega}] = -\frac{\pi e^4}{\hbar^3}\int \frac{d\boldsymbol{k}}{8\pi^3}\sum_{vc}\frac{32\Delta^{\mathrm{b}}_{cv}(\boldsymbol{k})\Delta^{\mathrm{d}}_{cv}(\boldsymbol{k})\mathrm{Im}[v^{\mathrm{a}}_{vc}(\boldsymbol{k})r^{\mathrm{c}}_{cv}(\boldsymbol{k})]}{\omega^5_{cv}(\boldsymbol{k})}\delta(\omega_{cv}(\boldsymbol{k})-2\omega). \tag{2.66}$$

Lastly,

$$\chi^{\mathrm{abcd}}_{2,3,p\omega} = -\frac{e^4}{\hbar^3}\int \frac{d\boldsymbol{k}}{8\pi^3}\sum_{m\neq n\neq \ell} f_{m\ell}(\boldsymbol{k})\Delta^{\mathrm{d}}_{nm}(\boldsymbol{k})\mathrm{Re}[r^{\mathrm{c}}_{\ell m}(\boldsymbol{k})r^{\mathrm{b}}_{n\ell}(\boldsymbol{k})v^{\mathrm{a}}_{mn}(\boldsymbol{k})]\Big(W^{(2,3,1)}_{nm\ell,p\omega}(\boldsymbol{k}) - W^{(2,3,2)}_{mn\ell,p\omega}(\boldsymbol{k})\Big), \tag{2.67}$$

where

$$\begin{aligned}W^{(2,3,1)}_{nm\ell,\omega} = &-\frac{3\omega_{\ell m}-4\omega_{nm}}{\omega^3_{nm}(\omega_{nm}-\omega_{\ell m})^2(\omega_{nm}-\tilde{\omega})} + \frac{1}{\omega^2_{nm}(\omega_{nm}-\omega_{\ell m})(\omega_{nm}-\tilde{\omega})^2}\\ &-\frac{1}{\omega_{\ell m}(\omega_{\ell m}-\omega_{nm})^2(2\omega_{\ell m}-\omega_{nm})(\omega_{\ell m}-\tilde{\omega})},\end{aligned} \tag{2.68}$$

$$W^{(2,3,1)}_{nm\ell,2\omega} = -\frac{16}{\omega^3_{nm}(\omega_{nm}-2\omega_{\ell m})(\omega_{nm}-2\tilde{\omega})}, \tag{2.69}$$

$$\begin{aligned}W^{(2,3,2)}_{nm\ell,\omega} = &-\frac{3\omega_{n\ell}-4\omega_{nm}}{\omega^3_{nm}(\omega_{nm}-\omega_{n\ell})^2(\omega_{nm}-\tilde{\omega})} + \frac{1}{\omega^2_{nm}(\omega_{nm}-\omega_{n\ell})(\omega_{nm}-\tilde{\omega})^2}\\ &-\frac{1}{\omega_{n\ell}(\omega_{n\ell}-\omega_{nm})^2(2\omega_{n\ell}-\omega_{nm})(\omega_{n\ell}-\tilde{\omega})},\end{aligned} \tag{2.70}$$

and

$$W^{(2,3,2)}_{nm\ell,2\omega} = -\frac{16}{\omega^3_{nm}(\omega_{nm}-2\omega_{n\ell})(\omega_{nm}-2\tilde{\omega})}. \tag{2.71}$$

Then,

$$\chi^{\mathrm{abcd}}_{2} = \sum_{p=1}^{2}\left(\chi^{\mathrm{abcd}}_{2,1,p\omega} + \chi^{\mathrm{abcd}}_{2,2,p\omega} + \chi^{\mathrm{abcd}}_{2,3,p\omega}\right). \tag{2.72}$$

Following the same steps that lead to χ^{abcd}_{2}, we obtain that

$$\chi^{\mathrm{abcd}}_{1} = \sum_{p=1}^{2}\Big(\chi^{\mathrm{abcd}}_{1,1,p\omega} + \chi^{\mathrm{abcd}}_{1,2,p\omega} + \chi^{\mathrm{abcd}}_{1,3,p\omega}\Big), \tag{2.73}$$

where, for $\chi^{\mathrm{abcd}}_{1,1,p\omega}$ we obtain

$$\chi^{\mathrm{abcd}}_{1,1,p\omega} = -\frac{e^4}{\hbar^3}\int \frac{d\boldsymbol{k}}{8\pi^3}\sum_{m\neq n} f_{mn}\mathrm{Im}[v^{\mathrm{a}}_{mn;k^{\mathrm{d}}}(\boldsymbol{k}))r^{\mathrm{c}}_{nm;k^{\mathrm{b}}}(\boldsymbol{k})]W^{(1,1)}_{nm,p\omega}, \tag{2.74}$$

with

$$W^{(1,1)}_{nm,\omega} = \frac{-3}{\omega^3_{nm}(\omega_{nm}-\tilde{\omega})} - \frac{1}{\omega^2_{nm}(\omega_{nm}-\tilde{\omega})^2},$$
$$W^{(1,1)}_{nm2,\omega} = \frac{8}{\omega^3_{nm}(\omega_{nm}-2\tilde{\omega})}, \tag{2.75}$$

and

$$\chi^{\mathrm{abcd}}_{1,1,2\omega} = -\frac{e^4}{\hbar^3}\int \frac{d\boldsymbol{k}}{8\pi^3}\sum_{vc}\frac{8\mathrm{Im}[v^{\mathrm{a}}_{vc;k^{\mathrm{d}}}(\boldsymbol{k})r^{\mathrm{c}}_{cv;k^{\mathrm{b}}}(\boldsymbol{k})]}{\omega^3_{cv}(\boldsymbol{k})}\delta(\omega_{cv}(\boldsymbol{k})-2\tilde{\omega}). \tag{2.76}$$

$\chi^{\mathrm{abcd}}_{1,2,p\omega}$ is given by

$$\chi^{\mathrm{abcd}}_{1,2,p\omega} = \frac{e^4}{\hbar^3}\int \frac{d\boldsymbol{k}}{8\pi^3}\sum_{m\neq n} f_{mn}\Delta^{\mathrm{b}}_{nm}\mathrm{Im}[r^{\mathrm{c}}_{nm}v^{\mathrm{a}}_{mn;k^{\mathrm{d}}}]W^{(1,2)}_{nm,p\omega}, \tag{2.77}$$

with

$$W^{(1,2)}_{nm,\omega} = \frac{-7}{\omega^4_{nm}(\omega_{nm}-\tilde{\omega})} - \frac{3}{\omega^3_{nm}(\omega_{nm}-\tilde{\omega})^2} - \frac{1}{\omega^2_{nm}(\omega_{nm}-\tilde{\omega})^3},$$
$$W^{(1,2)}_{nm,2\omega} = \frac{16}{\omega^4_{nm}(\omega_{nm}-2\omega)}, \tag{2.78}$$

and

$$\chi^{\mathrm{abcd}}_{1,2,2\omega} = \frac{e^4}{\hbar^3}\int \frac{d\boldsymbol{k}}{8\pi^3}\sum_{vc}\frac{16\Delta^{\mathrm{b}}_{cv}(\boldsymbol{k})\mathrm{Im}[r^{\mathrm{c}}_{cv}(\boldsymbol{k})v^{\mathrm{a}}_{vc;k^{\mathrm{d}}}(\boldsymbol{k})]}{\omega^4_{cv}(\boldsymbol{k})}\delta(\omega_{cv}(\boldsymbol{k})-2\omega). \tag{2.79}$$

$\chi^{\mathrm{abcd}}_{1,3,p\omega}$ is given by

$$\chi^{\mathrm{abcd}}_{1,3,p\omega} = \frac{e^4}{\hbar^3}\int \frac{d\boldsymbol{k}}{8\pi^3}\sum_{m\neq n\neq \ell} f_{m\ell}\mathrm{Re}[v^{\mathrm{a}}_{mn;k^{\mathrm{d}}}r^{\mathrm{c}}_{\ell m}r^{\mathrm{b}}_{n\ell}]\Big(W^{(1,3,1)}_{nm\ell,p\omega} - W^{(1,3,2)}_{mn\ell,p\omega}\Big), \tag{2.80}$$

where

$$W^{(1,3,1)}_{nm\ell,\omega} = \frac{1}{\omega^2_{nm}\omega_{n\ell}(\omega_{nm}-\tilde{\omega})} - \frac{1}{\omega_{\ell m}\omega_{\ell n}(\omega_{nm}-2\omega_{\ell m})(\omega_{\ell m}-\tilde{\omega})}$$
$$W^{(1,3,1)}_{nm\ell,2\omega} = -\frac{8}{\omega^2_{nm}(\omega_{nm}-2\omega_{\ell m})(\omega_{nm}-2\tilde{\omega})},$$
$$W^{(1,3,2)}_{nm\ell,\omega} = \frac{1}{\omega^2_{nm}\omega_{\ell m}(\omega_{nm}-\tilde{\omega})} + \frac{1}{\omega_{n\ell}\omega_{m\ell}(2\omega_{n\ell}-\omega_{nm})(\omega_{n\ell}-\tilde{\omega})},$$
$$W^{(1,3,2)}_{nm\ell,2\omega} = -\frac{8}{\omega^2_{nm}(\omega_{nm}-2\omega_{n\ell})(\omega_{nm}-2\tilde{\omega})}. \tag{2.81}$$

For χ_3^{abcd} and χ_4^{abcd}, we write

$$\chi_3^{\mathrm{abcd}}+\chi_4^{\mathrm{abcd}}=\sum_{p=1}^{2}\Big((\chi_{3,1,p\omega}^{\mathrm{abcd}}+\chi_{4,1,p\omega}^{\mathrm{abcd}})+(\chi_{3,2,p\omega}^{\mathrm{abcd}}+\chi_{4,2,p\omega}^{\mathrm{abcd}})+(\chi_{3,3,2,p\omega}^{\mathrm{abcd}}+\chi_{4,3,1,p\omega}^{\mathrm{abcd}})+(\chi_{3,3,1,p\omega}^{\mathrm{abcd}}+\chi_{4,3,2,p\omega}^{\mathrm{abcd}})\Big), \tag{2.82}$$

where we have grouped the χ's that have common factors within the small parentheses. We have that

$$\chi_{3,1,p\omega}^{\mathrm{abcd}}+\chi_{4,1,p\omega}^{\mathrm{abcd}}=-\frac{e^4}{\hbar^3}\int\frac{d\boldsymbol{k}}{8\pi^3}\sum_{m\neq n\neq l}f_{nl}\mathrm{Re}\big[v_{nm}^{\mathrm{a}}r_{ml}^{\mathrm{d}}r_{ln;k^{\mathrm{b}}}^{\mathrm{c}}\big]\Big(W_{nml,p\omega}^{(4,1)}-W_{nml,p\omega}^{(3,1)}\Big), \tag{2.83}$$

where

$$\begin{aligned}
W_{nml,\omega}^{(3,1)}&=\frac{1}{\omega_{nl}^2\omega_{ml}(\omega_{nl}-\tilde{\omega})}+\frac{1}{\omega_{nm}\omega_{lm}(2\omega_{nm}-\omega_{nl})(\omega_{nm}-\tilde{\omega})},\\
W_{nml,2\omega}^{(3,1)}&=-\frac{8}{\omega_{nl}^2(\omega_{nl}-2\omega_{nm})(\omega_{nl}-2\tilde{\omega})},\\
W_{nml,\omega}^{(4,1)}&=\frac{1}{\omega_{ln}^2\omega_{lm}(\omega_{ln}-\tilde{\omega})}+\frac{1}{\omega_{mn}\omega_{ml}(2\omega_{mn}-\omega_{ln})(\omega_{mn}-\tilde{\omega})},\\
W_{nml,2\omega}^{(4,1)}&=-\frac{8}{\omega_{ln}^2(\omega_{ln}-2\omega_{mn})(\omega_{ln}-2\tilde{\omega})}.
\end{aligned} \tag{2.84}$$

Now,

$$\chi_{3,2,p\omega}^{\mathrm{abcd}}+\chi_{4,2,p\omega}^{\mathrm{abcd}}=\frac{e^4}{\hbar^3}\int\frac{d\boldsymbol{k}}{8\pi^3}\sum_{m\neq n\neq l}f_{nl}\Delta_{ln}^{\mathrm{b}}\mathrm{Re}\big[v_{nm}^{\mathrm{a}}r_{ml}^{\mathrm{d}}r_{ln}^{\mathrm{c}}\big]\Big(W_{nml,p\omega}^{(4,2)}-W_{nml,p\omega}^{(3,2)}\Big), \tag{2.85}$$

with

$$\begin{aligned}
W_{nml,\omega}^{(3,2)}&=-\frac{3\omega_{nm}-4\omega_{nl}}{\omega_{nl}^3(\omega_{nl}-\omega_{nm})^2(\omega_{nl}-\tilde{\omega})}+\frac{1}{\omega_{nl}^2(\omega_{nl}-\omega_{nm})(\omega_{nl}-\tilde{\omega})^2}-\frac{1}{\omega_{nm}(\omega_{nm}-\omega_{nl})^2(2\omega_{nm}-\omega_{nl})(\omega_{nm}-\tilde{\omega})},\\
W_{nml,2\omega}^{(3,2)}&=-\frac{16}{\omega_{nl}^3(\omega_{nl}-2\omega_{nm})(\omega_{nl}-2\tilde{\omega})},\\
W_{nml,\omega}^{(4,2)}&=-\frac{3\omega_{mn}-4\omega_{ln}}{\omega_{ln}^3(\omega_{ln}-\omega_{mn})^2(\omega_{ln}-\tilde{\omega})}+\frac{1}{\omega_{ln}^2(\omega_{ln}-\omega_{mn})(\omega_{ln}-\tilde{\omega})^2}-\frac{1}{\omega_{mn}(\omega_{mn}-\omega_{ln})^2(2\omega_{mn}-\omega_{ln})(\omega_{mn}-\tilde{\omega})},\\
W_{nml,2\omega}^{(4,2)}&=-\frac{16}{\omega_{ln}^3(\omega_{ln}-2\omega_{mn})(\omega_{ln}-2\tilde{\omega})}.
\end{aligned} \tag{2.86}$$

Next,

$$\chi_{3,3,1,p\omega}^{\mathrm{abcd}}=\chi_{4,3,2,p\omega}^{\mathrm{abcd}}=\frac{e^4}{\hbar^3}\int\frac{d\boldsymbol{k}}{8\pi^3}\sum_{m\neq n\neq l\neq q}f_{ql}\mathrm{Im}\big[v_{nm}^{\mathrm{a}}r_{ml}^{\mathrm{d}}r_{lq}^{\mathrm{c}}r_{qn}^{\mathrm{b}}\big]\big(W_{nmlq,p\omega}^{(4,3,2)}+W_{nmlq,p\omega}^{(3,3,1)}\big), \tag{2.87}$$

where

$$\begin{aligned}
W^{(3,3,1)}_{nmlq,\omega} &= \frac{1}{\omega_{nm}(2\omega_{nm}-\omega_{nl})(\omega_{nm}-\omega_{ql})(\omega_{nm}-\tilde{\omega})} + \frac{1}{\omega_{ql}(2\omega_{ql}-\omega_{nl})(\omega_{ql}-\omega_{nm})(\omega_{ql}-\tilde{\omega})} \\
W^{(3,3,1)}_{nmlq,2\omega} &= \frac{8}{\omega_{nl}(\omega_{nl}-2\omega_{nm})(\omega_{nl}-2\omega_{ql})(\omega_{nl}-2\tilde{\omega})}, \\
W^{(4,3,2)}_{nmlq,\omega} &= \frac{1}{\omega_{mn}(2\omega_{mn}-\omega_{ln})(\omega_{mn}-\omega_{lq})(\omega_{mn}-\tilde{\omega})} + \frac{1}{\omega_{lq}(2\omega_{lq}-\omega_{ln})(\omega_{lq}-\omega_{mn})(\omega_{lq}-\tilde{\omega})}, \\
W^{(4,3,2)}_{nmlq,2\omega} &= \frac{8}{\omega_{ln}(\omega_{ln}-2\omega_{mn})(\omega_{ln}-2\omega_{lq})(\omega_{ln}-2\tilde{\omega})}.
\end{aligned} \tag{2.88}$$

Finally,

$$\chi^{\mathrm{abcd}}_{3,3,2,p\omega} + \chi^{\mathrm{abcd}}_{4,3,1,p\omega} = -\frac{e^4}{\hbar^3} \sum_{m\neq n\neq l\neq q\boldsymbol{k}} f_{nq} \mathrm{Im}[v^{\mathrm{a}}_{nm} r^{\mathrm{d}}_{ml} r^{\mathrm{c}}_{qn} r^{\mathrm{b}}_{lq}] \left(W^{(4,3,1)}_{nmlq,p\omega} + W^{(3,3,2)}_{nmlq,p\omega} \right), \tag{2.89}$$

where

$$\begin{aligned}
W^{(3,3,2)}_{nmlq,\omega} &= \frac{1}{\omega_{nm}\omega_{qm}(2\omega_{nm}-\omega_{nl})(\omega_{nm}-\tilde{\omega})} + \frac{1}{\omega_{nq}\omega_{mq}(2\omega_{nq}-\omega_{nl})(\omega_{nq}-\tilde{\omega})} \\
W^{(3,3,2)}_{nmlq,2\omega} &= \frac{8}{\omega_{nl}(\omega_{nl}-2\omega_{nm})(\omega_{nl}-2\omega_{nq})(\omega_{nl}-2\tilde{\omega})}, \\
W^{(4,3,1)}_{nmlq,\omega} &= \frac{1}{\omega_{mn}\omega_{mq}(2\omega_{mn}-\omega_{ln})(\omega_{mn}-\tilde{\omega})} + \frac{1}{\omega_{qn}\omega_{qm}(2\omega_{qn}-\omega_{ln})(\omega_{qn}-\tilde{\omega})}, \\
W^{(4,3,1)}_{nmlq,2\omega} &= \frac{8}{\omega_{ln}(\omega_{ln}-2\omega_{mn})(\omega_{ln}-2\omega_{qn})(\omega_{ln}-2\tilde{\omega})}.
\end{aligned} \tag{2.90}$$

Collecting the above results leads us to write the full 2PA susceptibility as

$$\chi^{\mathrm{abcd}} = \chi^{\mathrm{abcd}}_{\omega} + \chi^{\mathrm{abcd}}_{2\omega}, \tag{2.91}$$

where

$$\begin{aligned}
\chi^{\mathrm{abcd}}_{p\omega} =& \Big(\chi^{\mathrm{abcd}}_{1,1,p\omega} + \chi^{\mathrm{abcd}}_{1,2,p\omega} + \chi^{\mathrm{abcd}}_{1,3,p\omega} + \chi^{\mathrm{abcd}}_{2,1,p\omega} + \chi^{\mathrm{abcd}}_{2,2,p\omega} + \chi^{\mathrm{abcd}}_{2,3,p\omega} + \chi^{\mathrm{abcd}}_{3,1,p\omega} + \chi^{\mathrm{abcd}}_{3,2,p\omega} + \chi^{\mathrm{abcd}}_{3,3,1,p\omega} + \chi^{\mathrm{abcd}}_{3,3,2,p\omega} \\
& + \chi^{\mathrm{abcd}}_{4,1,p\omega} + \chi^{\mathrm{abcd}}_{4,2,p\omega} + \chi^{\mathrm{abcd}}_{4,3,1,p\omega} + \chi^{\mathrm{abcd}}_{4,3,2,p\omega} \Big),
\end{aligned} \tag{2.92}$$

with $p = 1, 2$. Using Fig. 2.1, we identify every element of the right branch that origins the respectably susceptibility term, this is

$$\rho^{(3)}_{eii} \rightarrow \chi^{(3)}_{2,1} + \chi^{(3)}_{2,2} + \chi^{(3)}_{1,1} + \chi^{(3)}_{1,2}, \tag{2.93}$$

$$\rho^{(3)}_{eie} \rightarrow \chi^{(3)}_{2,3} + \chi^{(3)}_{1,3}, \tag{2.94}$$

$$\rho^{(3)}_{eei} \rightarrow \chi^{(3)}_{3,2} + \chi^{(3)}_{4,2} + \chi^{(3)}_{3,1} + \chi^{(3)}_{4,2}, \tag{2.95}$$

$$\rho^{(3)}_{eee} \rightarrow \chi^{(3)}_{3,3,1} + \chi^{(3)}_{4,3,2} + \chi^{(3)}_{3,3,2} + \chi^{(3)}_{4,3,1}. \tag{2.96}$$

3 TWO-PHOTON ABSORPTION BULK SPECTROSCOPY

Outline

In order to calculate the 2PA susceptibility spectrum, the self-consistent ground state and the Kohn-Sham states were calculated in the DFT framework using the plane-wave ABINIT code [35]. In what follows, we calculate the results for 2PA using different pseudopotentials within several approximations, in order to determine which scheme gives the best results. For LDA, we used Troullier-Martins pseudopotentials [36] that are fully separable nonlocal pseudopotentials in the Kleinman-Bylander form [37] [LDA with norm-conserving pseudopotentials (LDA-PSPNC)]. To include the spin-orbit coupling (SOC) effect, we used Hartwigsen-Goedecker-Hutter (HGH) relativistic separable dual-space Gaussian pseudopotentials (LDA-HGH) [38]. To go beyond the LDA approximation, we use the generalized-gradient approximation (GGA) [39–41] and the meta-GGA (mGGA) [42].

We used 58415 $\boldsymbol{k}$-points in order to have well-converged results for the irreducible Brillouin zone (IBZ) integration, as given in Eq. (2.41), using the linear analytic tetrahedron method of Ref. [43]. Also, a cutoff energy of 24 Hartrees was used for the plane waves, and nine conduction bands (c) were used for the summations in Eq. (2.41). BeTe, diamond, GaP, GaAs, GaSb, Ge, InAs, InSb, Si CdTe, ZnS and ZnSe have eight valence bands (v), all the semiconductors have been studied with their corresponding experimental lattice constant a_0 and band-gap E_g, as shown in 3.2 Table 3.1 for a non-SOC calculation, and in Table 3.2 for a SOC calculation. For GaAs, Si and GaP, there are experimental data with which we compare our theoretical results and discuss them in detail; for all the other semiconductors mentioned above we only present the 2PA spectra as obtained within the SOC approach.

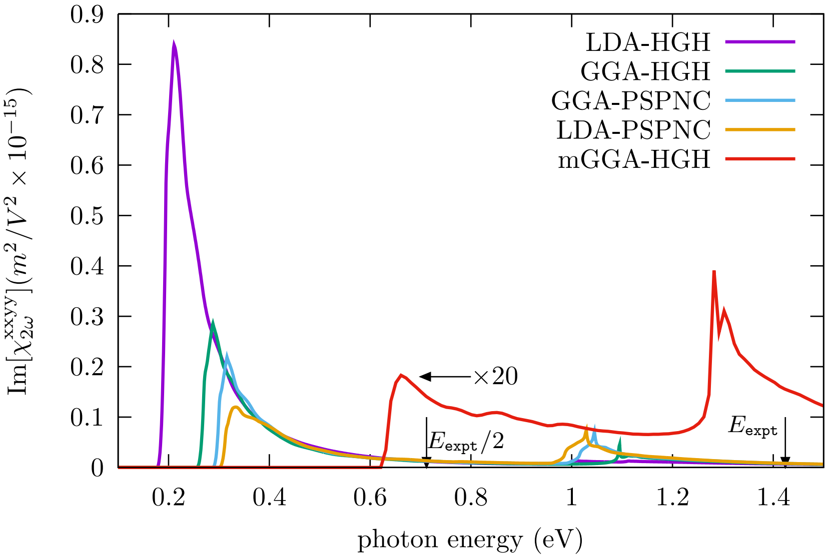

Figure 3.1: Im[$\chi_{2\omega}^{xxyy}$] for GaAs using different pseudopotentials. $E_g = 1.424$ eV is the experimental energy gap of GaAs, and $E_g/2$ is half the gap where 2PA becomes finite. No spin-orbit coupling is used in these results.

We start by comparing the results for $\chi_{2\omega}^{\mathrm{abcd}}(-\omega; -\omega, -\omega, \omega)$, using the several pseudopotential schemes described in the first paragraph of this section. All the semiconductors studied in this work are fcc, and thus, the only components that are different from zero due to their cubic F-43m space group are the $xxyy$, $xyyx$ and $xxxx$ (and the cyclic $x \to y \to z$ change). From here on, we suppress the $(-\omega; -\omega, -\omega, \omega)$ argument for ease of presentation. We chose only the $xxyy$ component as an example; on one hand, it gives the largest value for $\chi_{2\omega}^{\mathrm{abcd}}$, and on the other hand it conveys the same conclusions that the $xxxx$ and $xyyx$ components lead to. We chose GaAs, since the 2PA for this semiconductor has been recently measured [2], and it is a representative example of all the semiconductors used in this study. In Fig. 3.1, we show Im[$\chi_{2\omega}^{xxyy}$] vs the photon energy ($\hbar\omega$) for GaAs using the LDA-HGH, GGA-HGH, GGA-PSPNC, LDA-PSPNC, and mGGA-HGH. This sequence of pseudopotentials goes from the highest to the smallest magnitude of Im[$\chi_{2\omega}^{xxyy}$]. The energy value where Im[$\chi_{2\omega}^{xxyy}$] is abruptly finite corresponds to $E_g/2$, as expected then, Im[$\chi_{2\omega}^{xxyy}$] shows a first very well defined resonant peak, and then, other resonances that are below E_g. Also, the theoretical value of $E_g/2$ for each approach increases towards the experimental 2PA gap $E_{\mathtt{expt}}/2$. Indeed, we see that for mGGA-HGH, the 2PA gap $E_g/2 = 0.617$ eV is very similar to the experimental value of $E_{\mathtt{expt}}/2 = 0.707$ eV. As we see from Table 3.1, the mGGA-HGH gaps are much closer to the experimental values than the LDA gaps are. We also notice that the magnitude of Im[$\chi_{2\omega}^{xxyy}$] for mGGA-HGH is much smaller than for the other pseudopotentials. Due to the fact that mGGA-HGH gives the best energy gap E_g, in the following results we only use these pseudopotentials to calculate 2PA. In this section, we present the results without the inclusion of the SOC effect, leaving its inclusion to Sec. 3.1.1.

In Fig. 3.2, we show Im[χ^{abcd}] as a function of $\hbar\omega$, where the 2ω response starts being different

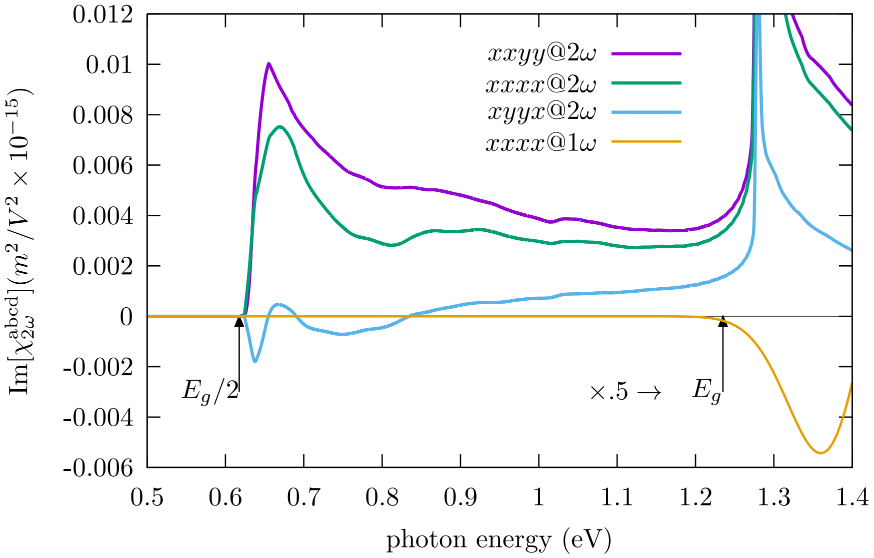

Figure 3.2: $\mathrm{Im}[\chi_{2\omega}^{\mathrm{abcd}}]$ for GaAs, where we see that the 2ω response starts at $E_g/2$, while the 1ω response starts at $E_g = 1.235$ eV, which is the mGGA gap.

from zero just at $E_g/2$ as expected, and then, it goes through a maximum and decreases as $\hbar\omega$ approaches E_g. Also, we see that $\mathrm{Im}[\chi_{2\omega}^{xxxx}]$ and $\mathrm{Im}[\chi_{2\omega}^{xxyy}]$ are positive, whereas $\mathrm{Im}[\chi_{2\omega}^{xyyx}]$ is negative below E_g. In the same figure, we only show $\mathrm{Im}[\chi_{1\omega}^{xxxx}]$, as it is the largest of the three components related to 1ω resonances, as explained in the section 2.4, particular in Eqs. (2.91) and (2.92). We see that $\mathrm{Im}[\chi_{1\omega}^{xxxx}]$ is finite around E_g, as it must, and although it is a factor of 2 larger than $\mathrm{Im}[\chi_{2\omega}^{\mathrm{abcd}}]$, $\mathrm{Im}[\chi_{1\omega}^{\mathrm{abcd}}]$, it does not contribute to 2PA below the gap E_g, which makes it unnecessary in this work.

As it is well known, the LDA schemes underestimated the energy gap E_g, as clearly seen in Fig. 3.1. To correct this deficiency within the scissors approximation, one needs to apply the scissors shift, as prescribed in Eqs. (2.42) and (2.43). For GaAs, a value of $\Sigma = 0.189$ eV is required to bring the mGGA-HGH gap to 1.424 eV, which is the experimental value at room temperature. We mention that this value of Σ is rather small as compared with what would be needed for the other pseudopotential schemes presented in Fig. 3.1. In Fig. 3.3, we show $\mathrm{Im}[\chi_{2\omega}^{\mathrm{abcd}}]$ for the nonscissored case, i.e., $\Sigma = 0$, and the scissored case of $\Sigma = 0.189\,\mathrm{eV}$. Both spectra are roughly the same, as if the scissors correction rigidly shifted the spectra from lower energies to higher energies; however, the scissors operator also lowers the intensity of the 2PA susceptibility by a factor of ~ 0.73. In Sec. 3.1, where the theoretical 2PA absorption is compared to experimental results, it is shown that the scissors correction yields the correct experimental values.

Eq. (2.92) shows all the terms that contribute to $\chi_{p\omega}^{\mathrm{abcd}}$, where $p = 1$ refers to the 1ω processes that are different from zero above the gap and thus, as explained before, are of no interest for this work. For $p = 2$, we get the 2ω processes that are different from zero below the gap, where $\chi_{1,1,2\omega}^{\mathrm{abcd}}$, $\chi_{1,2,2\omega}^{\mathrm{abcd}}$, $\chi_{2,1,2\omega}^{\mathrm{abcd}}$, $\chi_{2,2,2\omega}^{\mathrm{abcd}}$ are the terms that contribute the most to $\chi_{2\omega}^{\mathrm{abcd}}$, and which all come from transitions between two bands only. Indeed, the terms that involve transitions among three bands

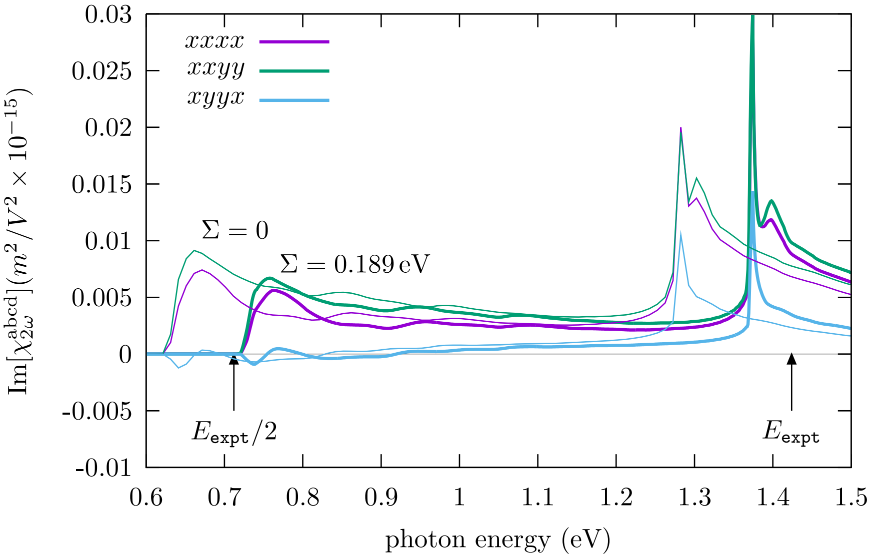

Figure 3.3: $\mathrm{Im}[\chi^{\mathrm{abcd}}_{2\omega}]$ for GaAs, with and without the contribution of the scissors operator. The experimental gap of GaAs at room temperature is 1.424 eV, and with $\Sigma = 0.189$ eV, it is enough to get the 2PA susceptibility to the experimental value $E_{\mathtt{expt}}/2$.

and four bands are negligible, as shown in Fig. 3.4, where we show $\chi^{xxyy}_{2\omega} = \chi^{xxyy}_{1,1,2\omega} + \chi^{xxyy}_{1,2,2\omega} + \chi^{xxyy}_{2,1,2\omega} + \chi^{xxyy}_{2,2,2\omega}$ corresponding to two bands, and $\chi^{xxyy}_{3\&4} = \chi^{xxyy}_{1,3,2\omega} + \chi^{xxyy}_{2,3,2\omega} + \chi^{xxyy}_{3,1,2\omega} + \chi^{xxyy}_{3,2,2\omega} + \chi^{xxyy}_{3,3,1,2\omega} + \chi^{xxyy}_{3,3,2,2\omega} + \chi^{xxyy}_{4,1,2\omega} + \chi^{xxyy}_{4,2,2\omega} + \chi^{xxyy}_{4,3,1,2\omega} + \chi^{xxyy}_{4,3,2,2\omega}$ corresponding to three bands and four bands; there, we see that these terms are a factor of 10^{-6} smaller, and therefore they can be neglected. We mention that calculating these terms takes a factor of ≈ 300 times longer than the calculation of $\chi^{\mathrm{abcd}}_{2\omega}$; the latter takes ≈ 210 min in 64 cores of an Intel processor for ≈ 58415 $\boldsymbol{k}$-points, which gives well converged results for the IBZ integration, as given in Eq. (2.41). Therefore, the fact that $\chi^{xxyy}_{3\&4}$ is negligible eases the burden of numerical calculation.

3.1 Comparison with experiments

In Ref. [2], the 2PA of GaAs, GaP and Si was experimentally measured using femtosecond pump–probe modulation spectroscopy. For GaAs, which is a direct-gap semiconductor, the measurements were done for photon energies $\hbar\omega$ such that $E_g/2 < \hbar\omega < E_g$, where E_g is the gap energy of GaAs. For GaP, which is an indirect-gap semiconductor, the measurements were done for photon energies $\hbar\omega$ such that $E_g/2 < \hbar\omega < E_g$, where E_g is the direct-gap energy of GaP. However, for Si, which is also an indirect-gap semiconductor, the measurements were done only for photon energies $\hbar\omega$ such that $E^i_g/2 < \hbar\omega < E^i_g$, where E^i_g the indirect-gap energy of Si. Therefore, for such photon energies, the indirect transitions are most likely due to phonon-assisted processes, and since our theoretical framework only considers direct transitions, it does not apply to this experimental situation. Nevertheless, we use the results for Si of Ref. [4] that were measured for photon $\hbar\omega$ such

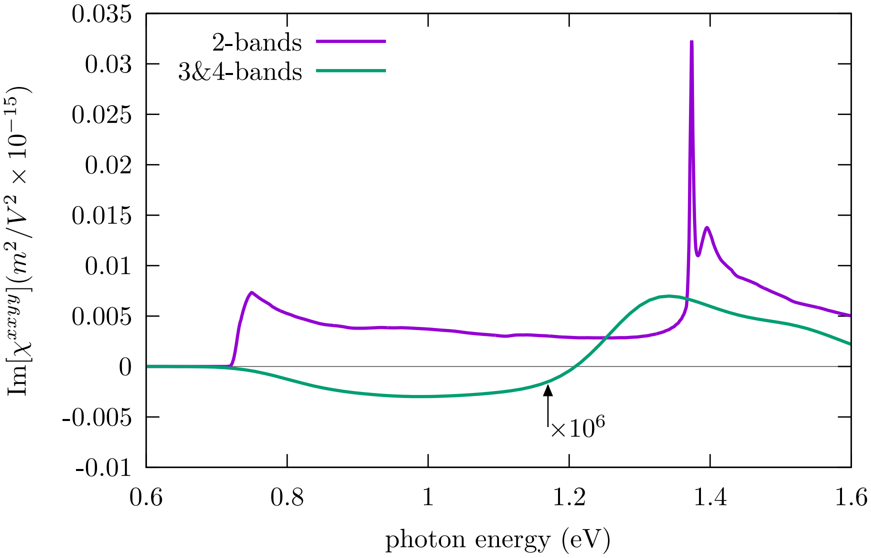

Figure 3.4: $\mathrm{Im}[\chi_{2\omega}^{xxyy}]$ for GaAs corresponding to transitions of two bands, and $\chi_{3\&4}^{xxyy}$ corresponding to transitions among three bands and four bands. The latter is smaller by a factor of 10^{-6}.

that $E_g/2 < \hbar\omega < E_g$, with E_g being the direct-gap energy of Si.

Phenomenologically the optical absorption is re presented as $\alpha = \alpha_0 + \beta I$ where α_0 is the linear absorption and β represents the third-order nonlinear absorption this means that the absorption depends on the light intensity and is modulated by the nonlinear absorption coefficient β, we need to express β through the nonlinear third order susceptibility. 2PA is characterized by a pump-probe $\beta_{11}^{\parallel}$ coefficient, where $\parallel$ indicates the co-polarized beams used in the experiment, and the subindex 11 means that the two photons have the same energy. As explained in Ref. [2], after solving the nonlinear wave equation on a plane-wave basis under the slowly varying field amplitude approximation, for a monochromatic and linearly polarized incident field, one gets a relation between the 2PA $\beta_{11}^{\parallel}$ coefficient and the imaginary part of third-order nonlinear susceptibility, as follows:

$$\beta_{11}^{\parallel}(\omega) = \frac{3\omega}{2\epsilon_0 n^2(\omega) c^2} \mathrm{Im}[\chi_{2\omega}^{XXXX}], \tag{3.1}$$

where $\chi_{2\omega}^{XXXX}$ is given in the XYZ laboratory coordinate system. Indeed, in the experiments, the beams propagate along $Z = 110$ in crystallographic coordinates, with $X = \bar{1}10$ and $Y = 001$, which defines a basis of linear polarization directions. Therefore, we have to rotate $\chi_{2\omega}^{\mathrm{abcd}}$ to the crystallographic coordinates by applying the following rotation:

$$\chi_{2\omega}^{\mathrm{ABCD}} = \mathcal{R}_A^a \mathcal{R}_B^b \mathcal{R}_C^c \mathcal{R}_D^d \chi_{2\omega}^{\mathrm{abcd}}, \tag{3.2}$$

using the rotation matrix that applies to the experimental conditions of Ref. [2], i.e.,

$$\mathcal{R} = \begin{bmatrix} -\cos\theta & \cos\theta & \sqrt{2}\sin\theta \\ \sin\theta & -\sin\theta & \sqrt{2}\cos\theta \\ 1 & 1 & 0 \end{bmatrix}, \tag{3.3}$$

where θ is the sample rotation angle in order to express Eq. (3.1) in terms of $\boldsymbol{\chi}_{2\omega}$ tensor components in crystallographic coordinates. This enables us to take advantage of the $\bar{4}3m$ (GaP and GaAs) or $m3m$ (Si) crystal symmetry, for which there are only three independent, nonvanishing components, $\chi_{2\omega}^{\mathrm{aaaa}}$, $\chi_{2\omega}^{\mathrm{aabb}} = \chi_{2\omega}^{\mathrm{abab}}$, and $\chi_{2\omega}^{\mathrm{abba}}$, where a$\neq$b. Then [2],

$$\beta_{11}^{\parallel}(\omega) = \frac{3\omega \mathrm{Im}[\chi_{2\omega}^{xxxx}(\omega)]}{32\epsilon_o n^2(\omega)c^2}\Big((3\cos(4\theta) - 4\cos(2\theta) - 7)\sigma(\omega) + 16\Big), \tag{3.4}$$

and

$$\sigma(\omega) = 1 - \frac{2\mathrm{Im}[\chi_{2\omega}^{xxyy}] + \mathrm{Im}[\chi_{2\omega}^{xyyx}]}{\mathrm{Im}[\chi_{2\omega}^{xxxx}]} \tag{3.5}$$

is known as the anisotropy parameter, with θ being the sample rotation angle, which, from Ref. [2], is equal to zero. Thus, the three independent components of $\mathrm{Im}[\chi_{2\omega}^{\mathrm{abcd}}]$ of a $\bar{4}3m$ or $m3m$ crystal contribute to the measurement of two-beam 2PA while rotating the sample about $Z = 110$ in copolarized geometry. Finally, $n(\omega) = \sqrt{\epsilon(\omega)}$ is the index of refraction with $\epsilon(\omega)$ being the dielectric function, which for the $\bar{4}3m$ and $m3m$ crystal symmetries $\epsilon(\omega) = \epsilon^{xx}(\omega) = \epsilon^{yy}(\omega) = \epsilon^{zz}(\omega)$.

In Fig. 3.5, we show the convergence of $\beta_{11}^{\parallel}(\omega)$ as a function of the number of $\boldsymbol{k}$ points required for the integration over the IBZ. We mention that as seen in Eqs. (3.4) and (3.5), $\beta_{11}^{\parallel}(\omega)$ depends on $\chi_{2\omega}^{xxxx}$, $\chi_{2\omega}^{xxyy}$ and $\chi_{2\omega}^{xyyx}$ and the index of refraction $n(\omega)$. As it turns out, $n(\omega)$ converges much faster than $\chi_{2\omega}^{\mathrm{abcd}}$, and a rather large number of $\boldsymbol{k}$ points are needed in order to get converged results for $\beta_{11}^{\parallel}(\omega)$. As a compromise for the numerical burden, we chose 58415 $\boldsymbol{k}$ points for the integration over the IBZ of the results shown below.

In Fig. 3.6, we show $\beta_{11}^{\parallel}(\omega)$ for the different pseudopotential schemes used in this work, all calculated with 58415 $\boldsymbol{k}$ points. Just as in Fig. 3.1, we see a similar spectral shape with the big difference that the result for mGGA-HGH now has the same order of magnitude as for the other approaches. This comes from the fact that $\beta_{11}^{\parallel}(\omega)$ is a ratio between $\chi_{2\omega}^{\mathrm{abcd}}$ and $n(\omega)$, and $n(\omega)$ is larger for LDA-HGH, GGA-HGH, GGA-PSPNC and LDA-PSPNC, than for mGGA-HGH, thus giving a similar magnitude for $\beta_{11}^{\parallel}(\omega)$.

In Fig. 3.7, we compare our results of $\beta_{11}^{\parallel}(\omega)$ with the corresponding experimental results of Ref. [2] for GaAs. The theoretical results have $\Sigma = 0.189$ eV, which corresponds to the scissors shift to bring the mGGA-HGH gap to the experimental gap, as given in Table 3.1. We mention that Σ shifts 2PA by $\Sigma/2$, since below the gap, only 2ω transitions are different from zero. As with the results presented in Fig. 3.3, where the scissors shift lowers the magnitude of $\chi_{2\omega}^{\mathrm{abcd}}$, the magnitude of $\beta_{11}^{\parallel}(\omega)$, also decreases as Σ increases; in this case, $n(\omega)$ also contributes to this effect, as it also decreases as Σ increases, and since $\beta_{11}^{\parallel}(\omega) \propto 1/n^2(\omega)$, as seen from Eq. (3.4), the overall effect of increasing Σ is that $\beta_{11}^{\parallel}(\omega)$ diminishes more than $\chi_{2\omega}^{\mathrm{abcd}}$ does. From Fig. 3.7, we find a reasonable

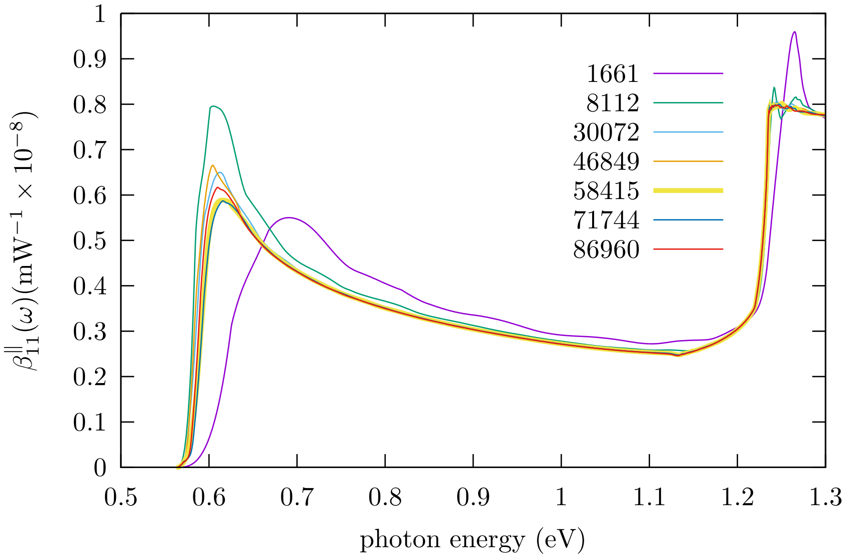

Figure 3.5: Convergence of $\beta_{11}^{\parallel}(\omega)$ as a function of the number of $\boldsymbol{k}$ points required for the integration over the IBZ. As a compromise for the numerical burden, we chose 58415 $\boldsymbol{k}$ points for the calculations.

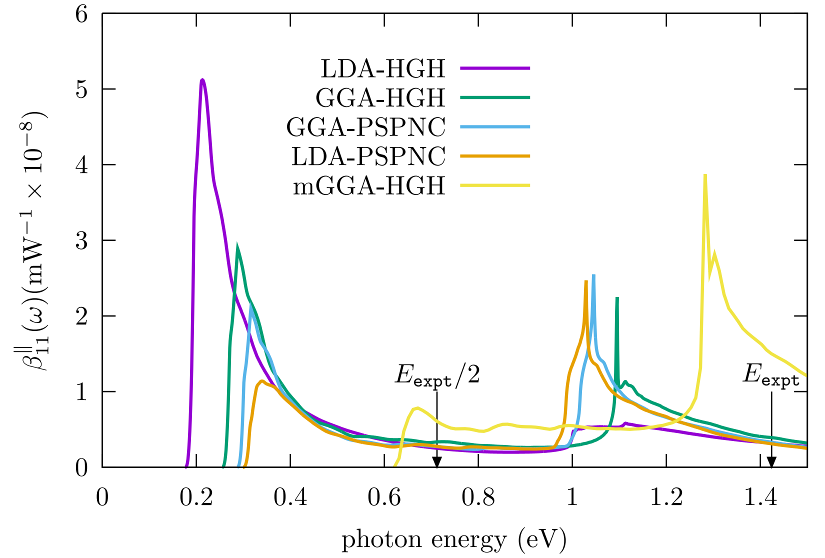

Figure 3.6: $\beta_{11}^{\parallel}(\omega)$ for the diferent pseudopotential schemes used in this work, calculated with 58415 $\boldsymbol{k}$ points for the integration over the IBZ.

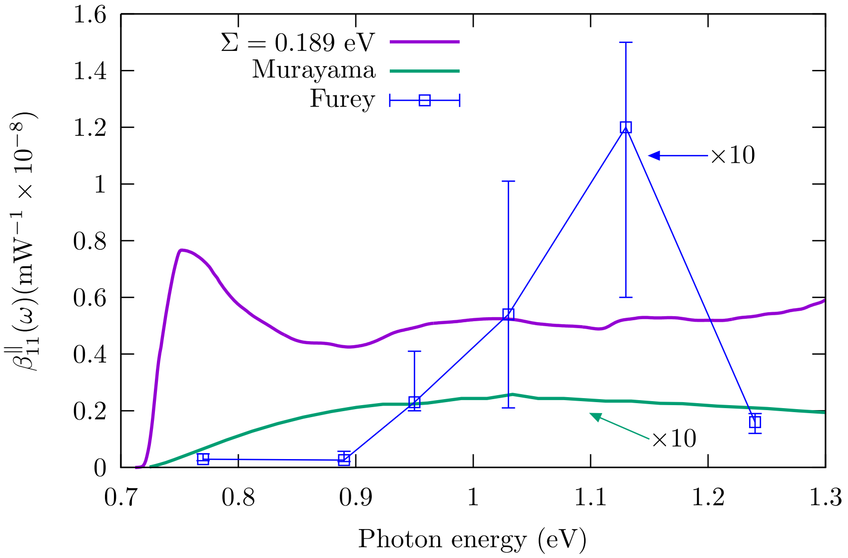

Figure 3.7: Theoretical 2PA $\beta^{\|}_{11}(\omega)$ coefficient for GaAs vs photon energy, where the scissors shift $\Sigma = 0.189$ eV takes the theoretical gap energy $E_g/2$ of the mGGA-HGH scheme to the experimental value. The theoretical results of Murayama and Nakayama [1] are shown by the green line. The squares are the experimental results for $\beta^{\|}_{11}(\omega)$ of Furey *et al.* [2]. See text for details.

match between the theoretical results and the experimental results, as far as the spectroscopic signature is concerned. To wit, there is a clear maximum in both, and although the width of the 2PA peak is not equal, the theoretical results clearly show a resonance in the response. Also, both the experimental and theoretical spectra are of the same order of magnitude. In Fig. 3.7, we also compare our results with the theoretical results of Murayama and Nakayama Ref. [1]. We see that the results of Murayama and Nakayama do not present a resonance and the maximum value is a factor of ~ 6 smaller than the experimental maximum value. Although the object of this article is not to analyze why Ref. [1] gives such results, we mention that their expression for $\mathrm{Im}[\chi^{\mathrm{abcd}}(-\omega; -\omega, -\omega, \omega)]$ diverges at $\omega = 0$, does not include the *intraband* $\hat{\boldsymbol{r}}_i$ contribution of the $\hat{\boldsymbol{r}}$ position operator, and only presents ω resonances. We emphasize that from Fig. 2.1, our expression for $\chi^{\mathrm{abcd}}_{2\omega}$ depends mainly on $\rho^{(3)}_{eii}$, which includes contributions from both $\boldsymbol{r}_i$ and $\boldsymbol{r}_e$, and that below the energy gap E_g, only 2ω resonances contribute, in contrast to the expression of Ref. [1]. As shown in Fig. 3.7, the 2ω resonance qualitatively matches the experimental results.

3.1.1 Spin-orbit coupling effects

In Fig. 3.8, we show $\beta^{\|}_{11}(\omega)$ vs photon energy with and without the inclusions of the spin-orbit coupling (SOC) interaction for GaAs. For this case we have used $\Sigma = 0.65$ eV (with SOC) and $\Sigma = 0.540$ eV (without SOC) as the scissors shift values needed to bring the theoretical with-SOC and without-SOC results to where the experimental 2PA rises from near to zero values to finite

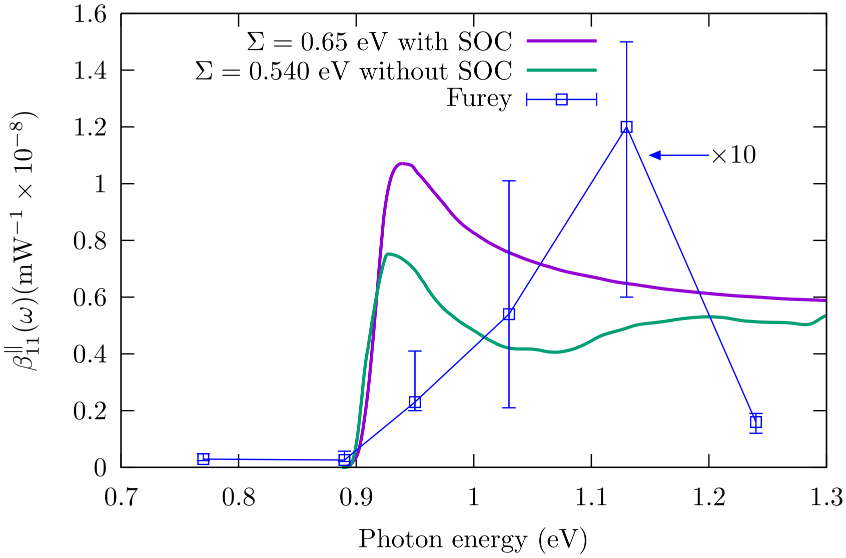

Figure 3.8: 2PA GaAs coefficient $\beta_{11}^{\|}(\omega)$ vs photon energy with and without spin-orbit coupling (SOC) effect. The blue squares are the experimental results of Furey *et al.* [2]. See text for details.

values. We see that the SOC theoretical spectrum shows a small shift to larger photon energies and a larger magnitude, as compared to the result without SOC. The second broad resonance obtained in the result without SOC for $\beta_{11}^{\|}(\omega)$ is absent in the results with SOC, and the magnitude of the SOC result is much closer to the experimental results shown in the same figure.

In Fig. 3.9, we compare our 2PA $\mathrm{Im}[\chi_{2\omega}^{\mathrm{abcd}}]$ for GaAs including SOC with the experimental results of Ref. [2] and those of Ref. [3]. As we did in Fig. 3.8, we use $\Sigma = 0.65$ eV to bring the theoretical SOC results to where the experimental 2PA rises from near-zero values to finite values. The results of Ref. [2] give $\mathrm{Im}[\chi_{2\omega}^{xxyy}] \approx \mathrm{Im}[\chi_{2\omega}^{xxxx}]$, and $\mathrm{Im}[\chi_{2\omega}^{xyyx}]$ is smaller, whereas for Ref. [3], the results are only for a photon energy of 1.3 eV, and $\mathrm{Im}[\chi_{2\omega}^{xxxx}] > \mathrm{Im}[\chi_{2\omega}^{xxyy}] \approx \mathrm{Im}[\chi_{2\omega}^{xyyx}]$. The relative size of our theoretical results follows $\mathrm{Im}[\chi_{2\omega}^{xxyy}] > \mathrm{Im}[\chi_{2\omega}^{xxxx}] > \mathrm{Im}[\chi_{2\omega}^{xyyx}]$; then, only $\mathrm{Im}[\chi_{2\omega}^{xxyy}]$ and $\mathrm{Im}[\chi_{2\omega}^{xyyx}]$ follow the experimental trend of Ref. [2]. We remark that the experimental values of $\mathrm{Im}[\chi_{2\omega}^{\mathrm{abcd}}]$ are inferred from the measurement of the $\beta_{11}^{\|}$ coefficient, and judging from the experimental error bars, they may be not precise. Finally, we see that the order of magnitude of the theoretical and experimental values for $\mathrm{Im}[\chi_{2\omega}^{\mathrm{abcd}}]$ are similar.

In Fig. 3.10, we compare our 2PA $\beta_{11}^{\|}(\omega)$ results for Si, with and without SOC, with the experimental results $\beta_{\mathrm{eff}}(\omega)$ of Ref. [4]. The values of Σ are those required to get the theoretical half gap of Si to its experimental value of 1.7 eV, as given in Table 3.1. Our results show an abrupt rise of $\beta_{11}^{\|}(\omega)$ just above $E_{\mathrm{expt}}/2$, and then, several resonances. The first one is a strong narrow resonance that starts just above 1.8 eV, raises sharply as the photon energy increases, and then it encounters a second sharp resonance, albeit with a smaller intensity; this second resonance is much stronger for the SOC case. Then, around 2.2 eV, both the SOC and the non-SOC spectra show signatures that resemble the experimental results, as far as the spectral features are concerned. Indeed, the

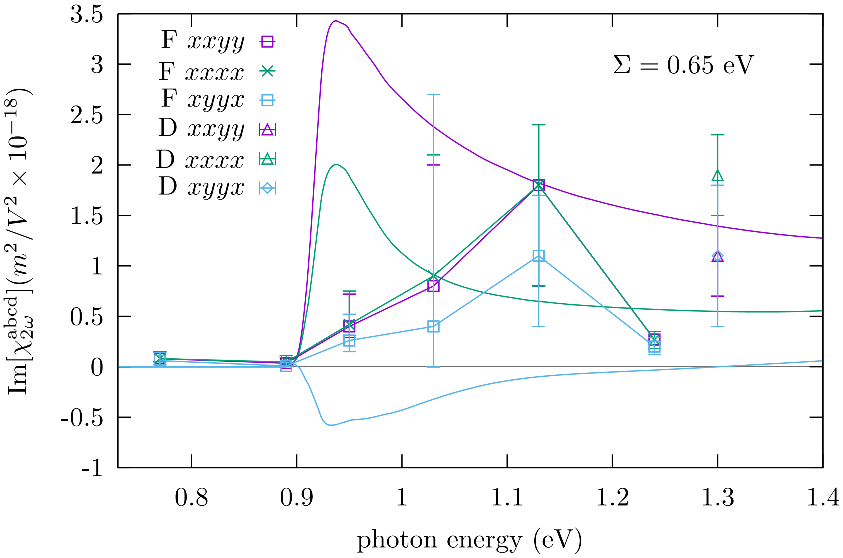

Figure 3.9: Theoretical 2PA $\text{Im}[\chi_{2\omega}^{\text{abcd}}]$, including SOC for GaAs, compared with the experimental results of Furey *et al.* [2] (F) and Dvorak *et al.* [3] (D). See text for details.

experimental results of Ref. [4], which cover a limited energy range, show a clear resonance that resembles our theoretical calculations, and the overall spectrum follows reasonably well the theoretical trend; we mention, though, that the SOC results better resemble the experimental spectrum. The magnitude of theoretical results differs from that of the experimental results. This could be related to the fact that $\beta_{\text{eff}}(\omega)$ was measured in such a way that the crystallographic contribution of the several components of $\chi_{2\omega}^{\text{abcd}}$ was not taken into account, thus giving a 2PA that comes from the experimental "averaging" of the mixing of different Si $\chi_{2\omega}^{\text{abcd}}$ components. Indeed, as explained in Ref. [4], an "effective" $\beta_{\text{eff}}(\omega)$ was extracted by measuring the intensity $I(\omega)$ dependence of an effective absorption coefficient $\alpha_{\text{eff}}(\omega)$, whose derivative with respect to $I(\omega)$ gives the 2PA $\beta_{\text{eff}}(\omega)$, whereas, in Ref. [2], it is the 2PA $\beta_{11}^{||}(\omega)$ of Eq. (3.4) which is measured. This could lead to the different magnitude of 2PA measured in the two experiments; nevertheless, the spectroscopic experimental signature is similar to our 2PA $\beta_{11}^{||}(\omega)$ theory.

Likewise, in Fig. 3.11, we show the 2PA $\beta_{11}^{||}(\omega)$ for GaP. The two values of Σ take the corresponding calculation without SOC and with SOC to the experimental 2PA gap. We see, at the onset of the two-photon transitions, a modest rise of the 2PA, followed by an almost constant 2PA and an intense and broad resonance at ~ 1.7 eV. In this case, the first two experimental points seem to follow the monotonic increase of the theoretical result, and the third experimental point misses the strong theoretical resonance. This shows how theory could guide the experiments; had the experiment been carried around 1.7 eV, the resonance could have been detected.

Finally, in Sec. 3.2, we show a comparison of 2PA $\beta_{11}^{||}(\omega)$ coefficient and $\text{Im}[\chi_{\text{aa}}(\omega)]$ for GaAs, Si and GaP, and most importantly, also, in Sec. 3.2, we show $\beta_{11}^{||}(\omega)$ for several semiconductors, where it is worth mentioning that the 2PA energy range spans from ~ 0.1 for InSb to ~ 6.5 eV

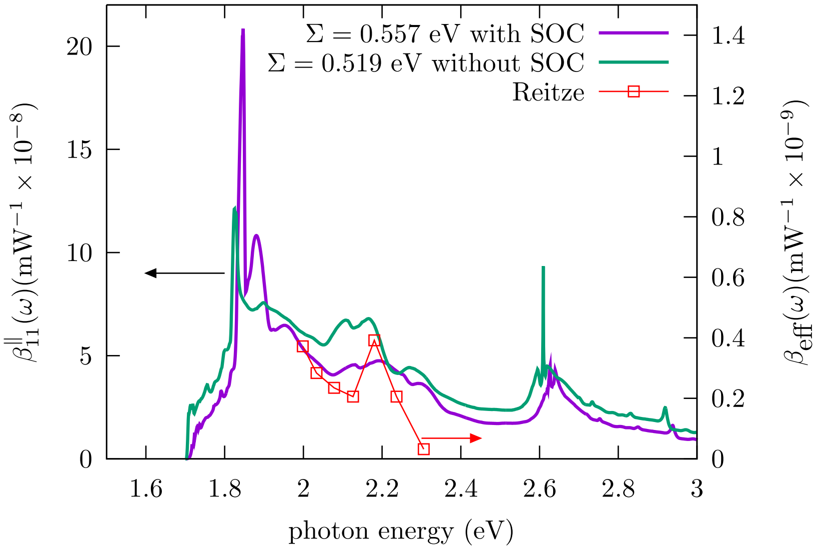

Figure 3.10: Theoretical $\beta^{\parallel}_{11}(\omega)$ (left axis) and experimental $\beta_{\mathrm{eff}}(\omega)$ (right axis) 2PA coefficient for Si vs $\hbar\omega$, where the red squares are the experimental results of Reitze *et al.* [4]. See text for details.

for diamond, and the intensity in $\mathrm{mW}^{-1}\times 10^{-8}$ goes from ~ 0.4 for ZnS to ~ 70 for InSb. Our theoretical formulation leads to results that would certainly enhance the applicability of 2PA, as it permits predictions that compare qualitatively well with available experiments.

3.1.2 Si band structure

In Fig. 3.12, we show the band structure for Si including SOC, where the thick-thin lines represent degenerated states due to high-symmetry lines in the Irreducible Brillouin Zone (IBZ). We mention that for the energy scale used in Fig. 3.12, the SOC-split bands, whose energy splitting is small, are not discernible. However, in Fig. 3.14 for GaAs, the SOC splited bands are readily seen. The arrows represent the $\hbar\omega$ photons, two of them per transition, that go from valence (v) to conduction bands (c), covering the energy range of the experimental data shown in Fig. 3.10, which goes from 2.05 eV to 2.35 eV. The 2ω transitions around Γ in the L-Γ-X path go from $v=2$ to degenerated $c=2\&3$, and from degenerated $v=3\&4$ to $c=1$, $c=2\&3$ and $c=4$, where we have used "'&" to denote the bands degeneracy. The next sets of transitions are those away from Γ along the Γ-X path. The first set goes from $v=3\&4$ to $c=2$, and then, there are two sets of transitions (violet-blue arrows) whose energy is $2.2\pm.05$ eV, with the first set going from $v=2$ to $c=1$ and the second set from $v=3\&4$ to $c=1$. Along K-Γ, valence bands $v=2,3$ and $v=4$, as well as conduction bands $c=1,2$ and $c=3$ are nondegenerated. The first set of transitions goes from $v=4$ to $c=1,2,3$, and then, a second set of transitions goes from $v=3,4$ to $c=1,2,3$. Finally, very close to Γ and the last path Γ-L, is the mirror image of L-Γ. A full view of the L-Γ-X-K-Γ-L path for the bands and its 2ω arrows is given in Fig. 3.13. All these transitions contribute to the theoretical spectrum shown in Fig. 3.10, within ± 0.15 eV of the experimental peak at 2.2 eV, and we see that most of

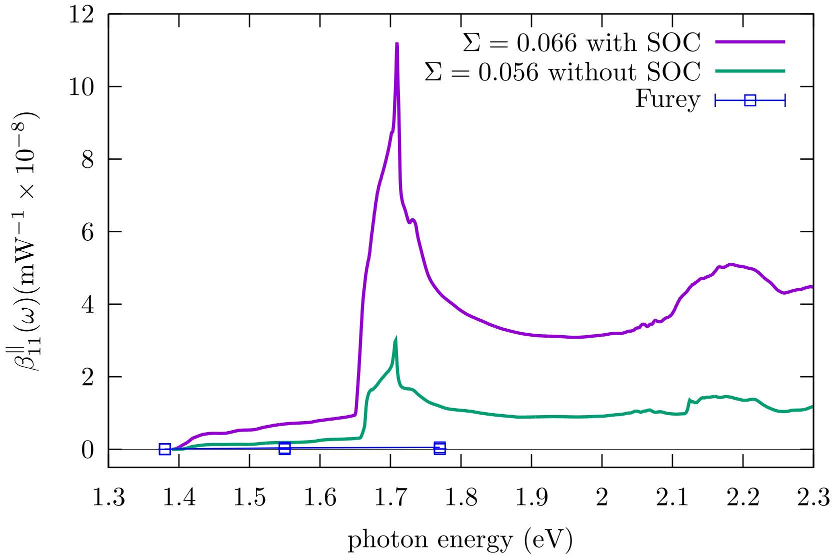

Figure 3.11: Theoretical and experimental $\beta^{\parallel}_{11}(\omega)$ 2PA coefficient for GaP vs $\hbar\omega$, with and without SOC. The squares are the experimental results of Furey *et al.* [2]. See text for details.

the transitions are away from the Γ point, as expected since the peak is away from where $\beta^{\parallel}_{11}(\omega)$ becomes finite close to the band-gap of Si. It is interesting to see that the peak at 2.2 eV comes from electronic transitions that originate among different bands and in different zones of the IBZ, where those close to X in the Γ-X path dominate. The same analysis was carried out for GaAs, and the band structure, along with the main results, is given in Fig. 3.14.

In Fig. 3.13, we show a full view of the band structure of Si along with the 2PA arrows around 2.2 ± 0.15 eV, and in Fig. 3.14, we show the band structure for GaAs around 0.94 ± 0.15 eV and 0.93 ± 0.15 eV, corresponding to the peak energies of the spectra in Fig 3.8 (the former is when SOC is included and, the latter when SOC is not included). The spin-split bands are very well seen in the top panels of Fig. 3.14. For these energies, the only transitions that contribute to $\beta^{\parallel}_{11}(\omega)$ are from $v = 1, 2, 3$ to $c = 1$.

3.2 Experimental lattice constant and experimental and theoretical band-gap energy values and additional results

In this section we show the results for 2PA spectroscopy for several fcc semiconductors. The calculated band-gap for every semiconductor is calculated using the pseudopotentias schemes used for spectroscopy calculations. In tables 3.1 and 3.2, we give the room-temperature experimental lattice constant a_0, in Bohrs, along with the experimental and theoretical band gaps energies E_g, in eV, for the semiconductors studied in this work, with and without SOC. For the indirect semiconductors, we only report the direct-gap. It is worth mentioning that the mGGA-HGH scheme overestimates

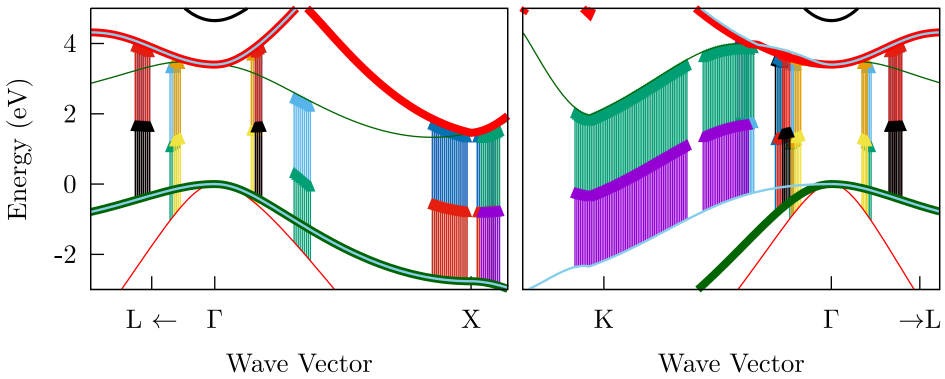

Figure 3.12: Band structure of Si for Σ = 1.32 eV, where each pair of arrows denote the corresponding 2ω transitions that contribute to 2PA around 2.2±0.15 eV, which is the peak energy of the spectrum of Fig 3.10. The two ω photons that are absorbed go from a valence band (red, green, cyan) to a conduction band (blue). See text for details.

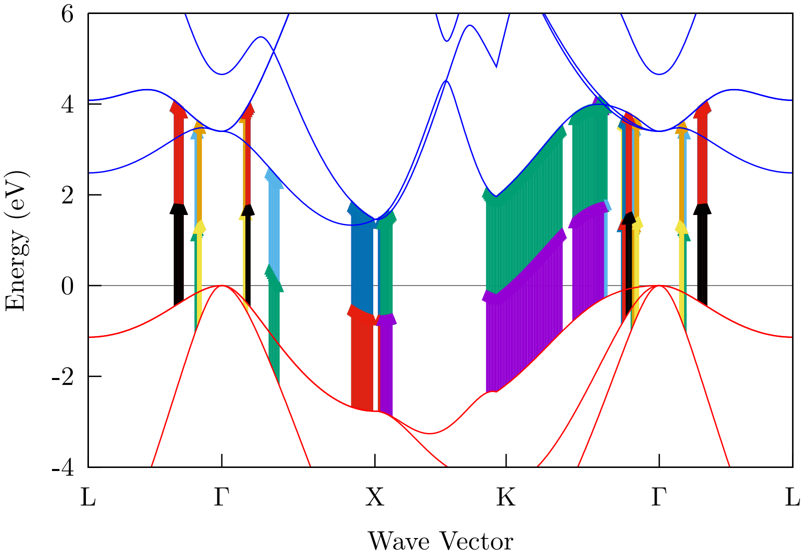

Figure 3.13: Band structure of Si for Σ = 0.519 eV, where each pair of arrows denote the corresponding 2ω transitions that contribute to 2PA around 2.2±0.15 eV, which is the peak energy of the spectrum in Fig 3.10. The two ω photons that are absorbed go from a valence band (red, green, cyan) to a conduction band (blue).

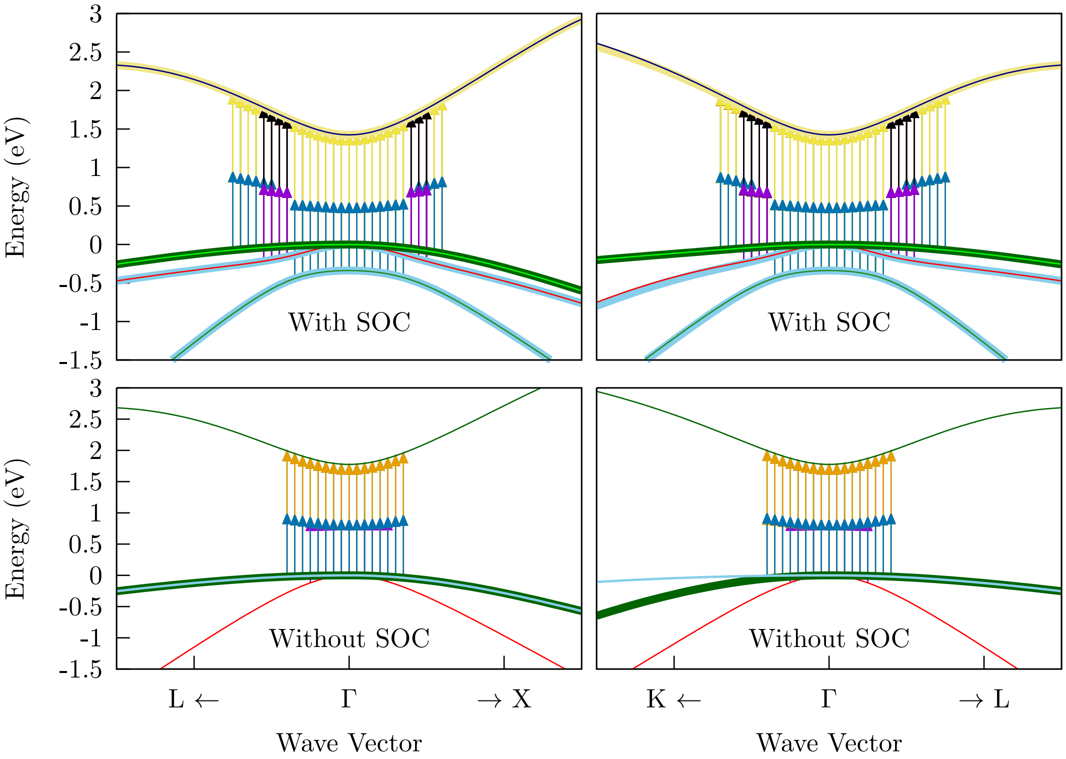

Figure 3.14: Band structure of GaAs, where the arrows denote the corresponding 2ω transitions that contribute to 2PA around 0.94 ±0.15 eV where SOC is included (top panels), and around 0.93 ±0.15 eV where SOC is not included (bottom panels). These energies correspond to the peak of the spectra shown in Fig 3.8. Each arrow represents the two ω photons that are absorbed, thus going from a valence band to a conduction band. See the text for details.

E_g for InSb, InAs, ZnS, CdTe and BeTe without SOC, and only for InAs and ZnS with SOC; this could be due to the fact that we are using room-temperature lattice constants instead of 0-K values.

In Fig. 3.15, we show a comparison of the 2PA coefficient $\beta^{\parallel}_{11}(\omega)$ and $\mathrm{Im}[\chi_{\mathrm{aa}}(\omega)]$ (whose abscissa is rescaled by $\hbar\omega/2$) for GaAs, Si and GaP. We see that although for Si and GaP $\beta^{\parallel}_{11}(\omega)$ and $\mathrm{Im}[\chi_{\mathrm{aa}}(\omega)]$ resemble each other only up to the first resonance, for GaAs there is no resemblance for most of the 2PA photon energies, and only they resemble each other just around E_{expt}, where 2PA would compete with the linear absorption, and thus is not interesting for 2PA. Also, except for the Si resonance $\sim$ 2.6 eV, we do not find a clear and compelling correlation between $\beta^{\parallel}_{11}(\omega)$ and $\mathrm{Im}[\chi_{\mathrm{aa}}(\omega)]$.

In Fig. 3.16, we show the spectra of the 2PA coefficient $\beta^{\parallel}_{11}(\omega)$ of several direct and indirect semiconductors, where the direct-band-gap E_g is used in the calculation. We show the spectra for energies $E_g/2 \leq \hbar\omega < E_g$, where only 2PA is present, and thus, the linear absorption does not intervene. The $\beta^{\parallel}_{11}(\omega)$ obtained for the different semiconductors, is arranged from the semiconductor

Direct semiconductors without SOC							
	a_0	E_g					
		Expt.	LDA-HGH	GGA-HGH	GGA-PSPNC	LDA-PSPNC	mGGA-HGH
GaAs	10.684	1.424	0.470	0.509	0.572	0.597	1.235
InSb	12.243	0.18	≈ 0	≈ 0	0.053	0.098	0.305
GaSb	11.519	0.75	0.099	0.113	0.203	0.260	0.613
InAs	11.448	0.345	≈ 0	≈ 0	0.113	0.128	0.522
ZnS	10.223	3.54	2.642	2.818	2.033	1.698	3.898
ZnSe	10.711	2.82	1.670	1.830	1.253	0.967	2.728
CdTe	12.24	1.5	1.029	1.168	0.7203	0.458	1.772
Indirect semiconductors without SOC							
Si	10.26	3.4	2.555	2.610	2.570	2.516	2.880
GaP	10.3	2.78	1.795	1.849	1.978	1.960	2.723
Diamond	6.74	6.5	5.677	5.743	5.664	5.593	5.865
Ge	10.69	0.805	≈ 0	≈ 0	0.007	0.091	0.516
BeTe	10.61	4.1	3.647	3.744	2.918	2.838	4.221

Table 3.1: Room-temperature experimental lattice constant a_0 in bohrs along with the experimental and theoretical direct-band-gap energies E_g in eV of the semiconductors studied in this work without SOC. For the indirect semiconductors, we only report the direct gap. We mention that for InSb, InAs and Ge the notation "≈ 0" means that the theoretical gaps are of the order of $\approx 10^{-11}$ eV.

with the highest value (InSb) to the semiconductor with the lowest value (ZnSe). It is worth mentioning that the 2PA energy range spans from ~ 0.1 for InSb to ~ 6.5 eV for diamond, and the intensity in mW$^{-1} \times 10^{-8}$ goes from ~ 0.4 for ZnS to ~ 70 for InSb. It should be clear that the particular characteristic of every material determines the spectral range of absorption and intensity. Moreover, the spectroscopy 2PA line shape depends on the electron dynamics, mainly that of the electrons in the last valence and first conduction bands, as explained above.

Direct semiconductors with SOC					
	a_0	E_g			
		Expt.	LDA-HGH	GGA-HGH	mGGA-HGH
GaAs	10.684	1.424	0.356	0.394	1.125
InSb	12.243	0.18	≈ 0	≈ 0	0.069
GaSb	11.519	0.75	≈ 0	≈ 0	0.385
InAs	11.448	0.345	≈ 0	≈ 0	0.412
ZnS	10.223	3.54	2.639	2.815	3.892
ZnSe	10.711	2.82	1.524	1.684	2.590
CdTe	12.24	1.5	0.732	0.869	1.493
Indirect semiconductors with SOC					
Si	10.26	3.4	2.515	2.569	2.843
GaP	10.3	2.78	1.785	1.838	2.714
Diamond	6.74	6.5	5.666	5.732	5.856
Ge	10.69	0.805	≈ 0	≈ 0	0.421
BeTe	10.61	4.1	3.297	3.393	3.892

Table 3.2: Room-temperature experimental lattice constant a_0 in bohrs along with the experimental and theoretical direct-band-gap energies E_g in eV of the semiconductors studied in this work with SOC. For the indirect semiconductors, we only report the direct gap. We mention that for InSb, GaSb, InAs and Ge the notation "≈ 0" means that the theoretical gaps are of the order of $\approx 10^{-11}$ eV.

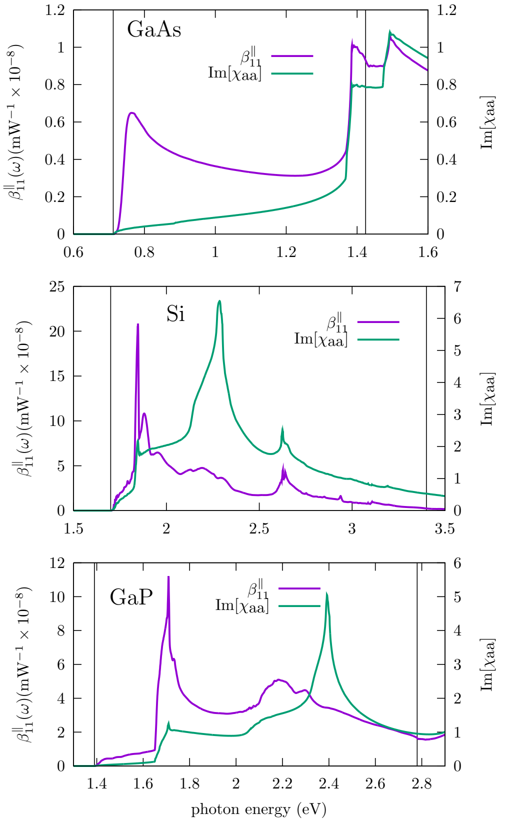

Figure 3.15: 2PA $\beta^{\parallel}_{11}(\omega)$ coefficient and Im$[\chi_{\text{aa}}(\omega)]$ (whose abscissa is rescaled by $\hbar\omega/2$) for GaAs, Si and GaP. The left vertical lines are at $E_{\text{expt}}/2$ whereas the right vertical lines are at E_{expt} of the corresponding material. See text for details.

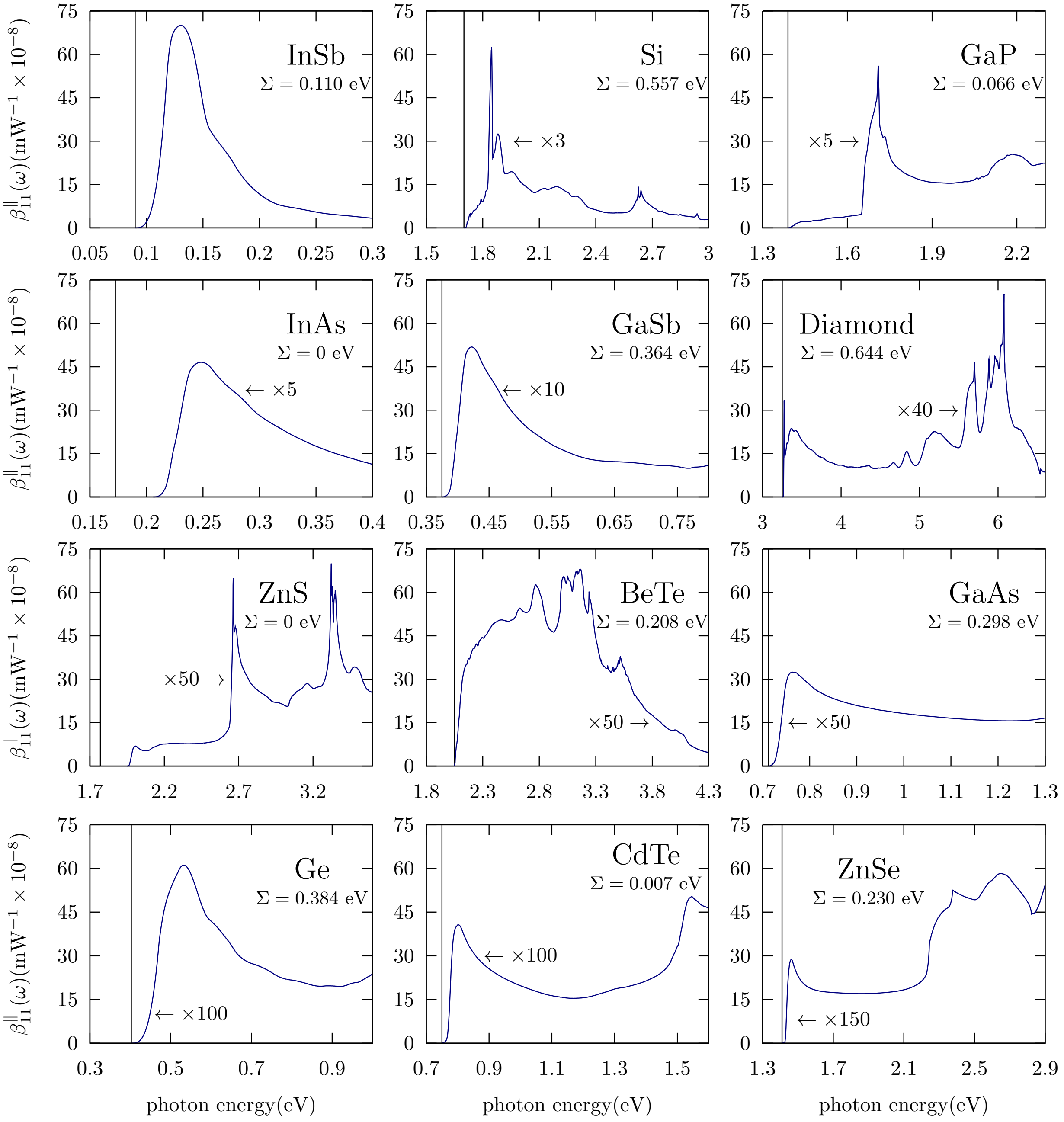

Figure 3.16: 2PA $\beta_{11}^{\parallel}(\omega)$ coefficient of Eq. (3.1) for several semiconductors as a function of photon energy $\hbar\omega$. The materials are oriented along (110) crystallographic direction, the incident beam is polarized in (100) direction. The scissors correction Σ (in eV) is shown for each material. The vertical black line is at $E_{expt}/2$. All the spectra calculated with mGGA-HGH including SOC.

4 2PA SURFACE RESPONSE

Outline

4.1 Theory

In this section, we derive the expressions for the microscopic current density of a given layer in the unit cell of a surface system [23]. The approach we use to study the surface of a semi-infinite semiconductor crystal is as follows. Instead of using a semi-infinite system, we replace it by the slab shown in Fig. 4.1. The slab consists of a front and back surface, and in between these two surfaces is the bulk of the system. In general the surface of a crystal reconstructs or relaxes as the atoms move to find equilibrium positions. This is due to the fact that the otherwise balanced forces are disrupted when the surface atoms do not find their partner atoms that are now absent at the surface of the system.

To take the reconstruction or relaxation into account, we take "surface" to mean the true surface of the first layer of atoms, and some of the atomic sub-layers adjacent to it. We chose the front and the back surfaces of the slab to be identical, rendering the total slab to be centrosymmetric. This way one could do a calculation for the whole slab and obtain $\chi_{2\omega}^{\mathrm{abcd}}(\omega)$ which would give the 2PA for the "whole slab" as well; the 2PA for the surface would be $\chi_{2\omega}^{S,\mathrm{abcd}}(\omega) = \chi_{2\omega}^{\mathrm{abcd}}(\omega)/2$, where the superscript S denotes surface. Nonetheless, it is very convenient to introduce a "cut function" [44], $\mathcal{C}^{\ell}(z)$ given by

$$\mathcal{C}^{\ell}(z) = \Theta(z - z_{\ell} + \Delta_{\ell}^{\mathrm{b}})\Theta(z_{\ell} - z + \Delta_{\ell}^{f}), \tag{4.1}$$

which is a top-hat cut function that selects a given layer of the slab, where Θ is the Heaviside function, $\Delta_{\ell}^{f/b}$ is the distance that the ℓ-th layer extends towards the front (f) or back (b) from its z_{ℓ} position and $\Delta_{\ell}^{f} + \Delta_{\ell}^{b}$ is the thickness of layer ℓ (see Fig. 4.1). Then, with $\mathcal{C}^{\ell}(z)$ we can calculate $\chi_{2\omega}^{\ell,\mathrm{abcd}}(\omega)$, for any given layer of the surface, subsurface and bulk of the slab. In principle one should be able to get that $\chi_{2\omega}^{\ell=\mathrm{bulk},\mathrm{abcd}}(\omega)$ is equal to $\chi_{2\omega}^{\mathrm{abcd}}(\omega)$ calculated for a bulk. In practice, the size of the slab needed to achieve this may be so large that the computation is not feasible. However, since the idea is to get the "surface" response, the cut function $\mathcal{C}^\ell(z)$ works just fine.

Now, we show how $\mathcal{C}^\ell(z)$ is introduced in the calculation of $\chi_{2\omega}^{\ell,\mathrm{abcd}}(\omega)$. The microscopic current density is given by

$$\mathbf{j}(\boldsymbol{r},t)=\mathrm{Tr}(\hat{\mathbf{j}}(\boldsymbol{r})\rho(\hat{t})), \tag{4.2}$$

where the operator for the electron current is

$$\hat{\mathbf{j}}(\boldsymbol{r})=\frac{e}{2}\left(\hat{\mathbf{v}}^\Sigma\left|\boldsymbol{r}\right\rangle\left\langle\boldsymbol{r}\right|+\left|\boldsymbol{r}\right\rangle\left\langle\boldsymbol{r}\right|\hat{\mathbf{v}}^\Sigma\right), \tag{4.3}$$

where $\hat{\boldsymbol{v}}^\Sigma$ is scissors corrected the electron velocity operator to be dealt with below. We define $\hat{\mu}\equiv\left|\boldsymbol{r}\right\rangle\left\langle\boldsymbol{r}\right|$ as the electron position operator and use the cyclic invariance of the trace to write

$$\begin{aligned}\mathbf{j}(\boldsymbol{r},t)=\mathrm{Tr}(\hat{\mathbf{j}}(\boldsymbol{r})\hat{\rho}(t)=\mathrm{Tr}(\hat{\rho}(t)\hat{\mathbf{j}}(\boldsymbol{r}))&=\frac{e}{2}\left(\mathrm{Tr}(\hat{\rho}\hat{\mathbf{v}}^\Sigma\hat{\mu})+\mathrm{Tr}(\hat{\rho}\hat{\mu}\hat{\mathbf{v}}^\Sigma)\right)\\&=\frac{e}{2}\sum_{n\boldsymbol{k}}\left(\left\langle n\boldsymbol{k}\right|\hat{\rho}\hat{\mathbf{v}}^\Sigma\hat{\mu}\left|n\boldsymbol{k}\right\rangle+\left\langle n\boldsymbol{k}\right|\hat{\rho}\hat{\mu}\hat{\mathbf{v}}^\Sigma\left|n\boldsymbol{k}\right\rangle\right)\\&=\frac{e}{2}\sum_{nm\boldsymbol{k}}\left\langle n\boldsymbol{k}\right|\hat{\rho}\left|m\boldsymbol{k}\right\rangle\left(\left\langle m\boldsymbol{k}\right|\hat{\mathbf{v}}^\Sigma\left|\mathbf{r}\right\rangle\left\langle\boldsymbol{r}|n\boldsymbol{k}\right\rangle+\left\langle m\boldsymbol{k}|\boldsymbol{r}\right\rangle\left\langle\boldsymbol{r}\right|\hat{\mathbf{v}}^\Sigma\left|n\boldsymbol{k}\right\rangle\right)\\&=\sum_{nm\boldsymbol{k}}\rho_{nm}(\boldsymbol{k};t)\mathbf{j}_{mn}(\boldsymbol{k};\boldsymbol{r}),\end{aligned} \tag{4.4}$$

where

$$\mathbf{j}_{mn}(\boldsymbol{k};\boldsymbol{r})=\frac{e}{2}\left(\left\langle m\boldsymbol{k}\right|\hat{\mathbf{v}}^\Sigma\left|\boldsymbol{r}\right\rangle\left\langle\boldsymbol{r}|n\boldsymbol{k}\right\rangle+\left\langle m\boldsymbol{k}|\boldsymbol{r}\right\rangle\left\langle\boldsymbol{r}\right|\hat{\mathbf{v}}^\Sigma\left|n\boldsymbol{k}\right\rangle\right), \tag{4.5}$$

are the matrix elements of the current operator, and we have used the fact that the matrix elements between states $\left|n\boldsymbol{k}\right\rangle$ are diagonal in $\boldsymbol{k}$, i.e. proportional to $\delta(\boldsymbol{k}-\boldsymbol{k}')$.

Integrating the current $\boldsymbol{j}(\boldsymbol{r},t)$ over the entire slab gives the averaged current density. If we want the contribution from only one region of the slab towards the total current, we can integrate $\mathbf{j}(\boldsymbol{r},t)$

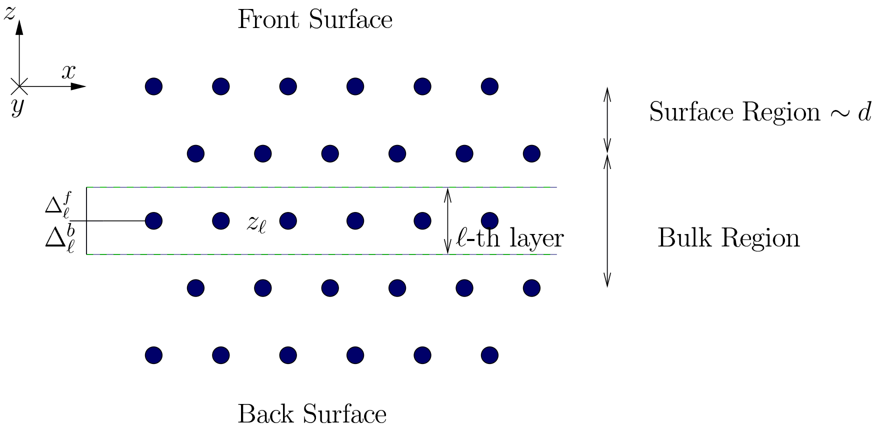

Figure 4.1: A sketch of a slab where the circles represent atoms, figure from [5].

over the desired region. The contribution to the current density from the ℓ-th layer of the slab is given by

$$\frac{1}{\Omega}\int d^3r\,\mathcal{C}^\ell(z)\,\boldsymbol{j}(\boldsymbol{r},t)\equiv\boldsymbol{J}^\ell(t),\tag{4.6}$$

where $\boldsymbol{J}^\ell(t)$ is the current of the ℓ-th layer. Therefore we define

$$e\boldsymbol{\mathcal{V}}^{\Sigma,\ell}_{mn}(\boldsymbol{k})\equiv\int d^3r\,\mathcal{C}^\ell(z)\,\mathbf{j}_{mn}(\boldsymbol{k};\boldsymbol{r}),\tag{4.7}$$

to write

$$J^{(N,\ell)}_a(t)=\frac{e}{\Omega}\sum_{mn\boldsymbol{k}}\mathcal{V}^{\Sigma,a,\ell}_{mn}(\boldsymbol{k})\rho^{(N)}_{nm}(\boldsymbol{k};t),\tag{4.8}$$

as the induced current of the ℓ-th layer, to order N in the external perturbation. The matrix elements of the density operator for $N=1,2,3$ are given by Eqs. (2.26), (2.30) and (2.34), respectively.

The Fourier component of the ℓ-th layer current of Eq. (4.8) is given by

$$J^{(N,\ell)}_{\mathrm{a}}(\omega)=\frac{e}{\Omega}\sum_{mn\boldsymbol{k}}\mathcal{V}^{\Sigma,\mathrm{a},\ell}_{mn}(\boldsymbol{k})\rho^{(N)}_{nm}(\boldsymbol{k};\omega),\tag{4.9}$$

and we proceed to give an explicit expression of $\boldsymbol{\mathcal{V}}^{\Sigma,\ell}_{mn}(\boldsymbol{k})$. From Eqs. (4.7) and (4.5) we obtain

$$\boldsymbol{\mathcal{V}}^{\Sigma,\ell}_{mn}(\boldsymbol{k})=\frac{1}{2}\int \mathrm{d}^3r\,\mathcal{C}^\ell(z)\Big[\langle m\boldsymbol{k}|\boldsymbol{v}^\Sigma|\boldsymbol{r}\rangle\langle\boldsymbol{r}|n\boldsymbol{k}\rangle+\langle m\boldsymbol{k}|\boldsymbol{r}\rangle\langle\boldsymbol{r}|\boldsymbol{v}^\Sigma|n\boldsymbol{k}\rangle\Big],\tag{4.10}$$

where dividing the pseudopotential of the Hamiltonian in local and non-local, we see that $\boldsymbol{v}^\Sigma=\boldsymbol{v}^\Sigma(\boldsymbol{r},\boldsymbol{r}')$ is a non-local operator. Using the well known property $\int d\boldsymbol{r}\,|\boldsymbol{r}\rangle\,\langle\boldsymbol{r}|=1$, we obtain

$$\begin{aligned}\langle m\boldsymbol{k}|\,\hat{\mathbf{v}}^\Sigma(\mathbf{r},\boldsymbol{r}')\,|\boldsymbol{r}\rangle&=\int d^3r''\,\langle m\boldsymbol{k}|\,\hat{\mathbf{v}}^\Sigma(\mathbf{r},\boldsymbol{r}')\,|\boldsymbol{r}''\rangle\,\langle\boldsymbol{r}''|\,|\boldsymbol{r}\rangle=\int d^3r''\,\langle m\boldsymbol{k}|\boldsymbol{r}''\rangle\,\hat{\mathbf{v}}^\Sigma(\mathbf{r},\boldsymbol{r}')\,\langle\boldsymbol{r}''|\boldsymbol{r}\rangle\\&=\int d^3r''\psi^*_{m\boldsymbol{k}}(\boldsymbol{r}'')\hat{\mathbf{v}}^\Sigma(\mathbf{r},\boldsymbol{r}')\delta(\boldsymbol{r}''-\boldsymbol{r})\\&\overset{\text{IBP}}{=}-\int d^3r''\hat{\mathbf{v}}^\Sigma(\mathbf{r},\boldsymbol{r}')\delta(\boldsymbol{r}''-\boldsymbol{r})\psi^*_{m\boldsymbol{k}}(\boldsymbol{r}'')=\hat{\mathbf{v}}^{\Sigma*}(\mathbf{r},\boldsymbol{r}')\psi^*_{m\boldsymbol{k}}(\boldsymbol{r}),\end{aligned}\tag{4.11}$$

where IBP means integrating by parts, and we used $\hat{\mathbf{v}}^{\Sigma*}(\mathbf{r},\boldsymbol{r}')=-\hat{\mathbf{v}}^\Sigma(\mathbf{r},\boldsymbol{r}')$; also

$$\langle\boldsymbol{r}|\hat{\mathbf{v}}^\Sigma(\mathbf{r},\boldsymbol{r}')|n\boldsymbol{k}\rangle=\int d^3r''\,\langle\boldsymbol{r}|\,\hat{\mathbf{v}}^\Sigma(\boldsymbol{r},\boldsymbol{r}')\,|\boldsymbol{r}''\rangle\,\langle\boldsymbol{r}''|n\boldsymbol{k}\rangle=\int d^3r''\,\langle\boldsymbol{r}|\boldsymbol{r}''\rangle\,\langle\boldsymbol{r}''|n\boldsymbol{k}\rangle)\hat{\mathbf{v}}^\Sigma(\boldsymbol{r},\boldsymbol{r}')=\psi_{n\boldsymbol{k}}(\boldsymbol{r})\hat{\mathbf{v}}^\Sigma(\boldsymbol{r},\boldsymbol{r}'),\tag{4.12}$$

where we used the fact that the operator $\mathbf{v}^\Sigma(\boldsymbol{r},\boldsymbol{r}')$ does not act on $\boldsymbol{r}''$, $\langle\boldsymbol{r}|n\boldsymbol{k}\rangle=\psi_{n\boldsymbol{k}}(\boldsymbol{r})$ and $\langle m\boldsymbol{k}|\boldsymbol{r}\rangle=\psi^*_{m\boldsymbol{k}}(\boldsymbol{r})$. Therefore, Eq. (4.10) reduces to

$$\begin{aligned}\boldsymbol{\mathcal{V}}^{\Sigma,\ell}_{mn}(\boldsymbol{k})&=\frac{1}{2}\int \mathrm{d}^3r\,\mathcal{C}^\ell(z)\Big[\,\langle\boldsymbol{r}|n\boldsymbol{k}\rangle\,\langle m\boldsymbol{k}|\boldsymbol{v}^\Sigma|\boldsymbol{r}\rangle+\langle m\boldsymbol{k}|\boldsymbol{r}\rangle\,\langle\boldsymbol{r}|\boldsymbol{v}^\Sigma|n\boldsymbol{k}\rangle\,\Big]\\&=\frac{1}{2}\int \mathrm{d}^3r\,\mathcal{C}^\ell(z)\Big[\psi_{n\boldsymbol{k}}(\boldsymbol{r})\hat{\mathbf{v}}^{\Sigma*}\psi^*_{m\boldsymbol{k}}(\boldsymbol{r})+\psi^*_{m\boldsymbol{k}}(\boldsymbol{r})\hat{\mathbf{v}}^\Sigma\psi_{n\boldsymbol{k}}(\boldsymbol{r})\Big]\\&=\int \mathrm{d}^3r\,\psi^*_{m\boldsymbol{k}}(\boldsymbol{r})\left[\frac{\mathbf{v}^\Sigma\mathcal{C}^\ell(z)+\mathcal{C}^\ell(z)\mathbf{v}^\Sigma}{2}\right]\psi_{n\boldsymbol{k}}(\boldsymbol{r})\\&=\int \mathrm{d}^3r\,\psi^*_{m\boldsymbol{k}}(\boldsymbol{r})\boldsymbol{\mathcal{V}}^{\Sigma,\ell}\psi_{n\boldsymbol{k}}(\boldsymbol{r}),\end{aligned}\tag{4.13}$$

where we used the hermitian property of $\boldsymbol{v}^{\Sigma}$, i.e. $\int \psi^* \hat{F}\phi\, dx = \int dx(\hat{F}\psi)^*\phi\, dx$ with $\hat{F} = \boldsymbol{v}^{\Sigma}$, and defined

$$\boldsymbol{V}^{\Sigma,\ell}(z) \equiv \frac{\boldsymbol{v}^{\Sigma}\mathcal{C}^{\ell}(z) + \mathcal{C}^{\ell}(z)\boldsymbol{v}^{\Sigma}}{2}, \tag{4.14}$$

where the superscript ℓ is inherited from $\mathcal{C}^{\ell}(z)$. We see that the replacement

$$\hat{\boldsymbol{v}}^{\Sigma} \to \hat{\boldsymbol{\mathcal{V}}}^{\Sigma,\ell}(z) = \left[\frac{\hat{\boldsymbol{v}}^{\Sigma}\mathcal{C}^{\ell}(z) + \mathcal{C}^{\ell}(z)\hat{\boldsymbol{v}}^{\Sigma}}{2}\right], \tag{4.15}$$

is all that is needed to change the velocity operator of the electron $\hat{\boldsymbol{v}}^{\Sigma}$ to the new velocity operator $\boldsymbol{\mathcal{V}}^{\Sigma,\ell}(z)$ that implicitly takes into account the contribution of the region of the slab given by $\mathcal{C}^{\ell}(z)$. From Appendix A,

$$\boldsymbol{\mathcal{V}}^{\Sigma}_{nm}(z) = \frac{\omega^{\Sigma}_{nm}}{\omega^{\mathrm{LDA}}_{nm}}\boldsymbol{\mathcal{V}}^{\mathrm{LDA}}_{nm}(z), \tag{4.16}$$

just as it happens for the bulk calculation. With this expression we can easily calculate

$$\begin{aligned}
\left(\mathcal{V}^{\Sigma,a,\ell}_{nm}(z)\right)_{;k^b} &= \left(\frac{\omega^{\Sigma}_{nm}}{\omega^{\mathrm{LDA}}_{nm}}\mathcal{V}^{\mathrm{LDA},a,\ell}_{nm}(z)\right)_{;k^b} \\
&= \frac{\omega^{\Sigma}_{nm;k^b}}{\omega^{\mathrm{LDA}}_{nm}}\mathcal{V}^{\mathrm{LDA},a,\ell}_{nm}(z) - \frac{\omega^{\Sigma}_{nm}}{(\omega^{\mathrm{LDA}}_{nm})^2}\mathcal{V}^{\mathrm{LDA},a,\ell}_{nm}(z)\omega^{LDA}_{nm;k^b} + \frac{\omega^{\Sigma}_{nm}}{\omega^{\mathrm{LDA}}_{nm}}\mathcal{V}^{\mathrm{LDA},a,\ell}_{nm;k^b}(z) \\
&= \frac{\Delta^{b}_{nm}}{\omega^{\mathrm{LDA}}_{nm}}\left(1 - \frac{\omega^{\Sigma}_{nm}}{\omega^{\mathrm{LDA}}_{nm}}\right)\mathcal{V}^{\mathrm{LDA},a,\ell}_{nm}(z) + \frac{\omega^{\Sigma}_{nm}}{\omega^{\mathrm{LDA}}_{nm}}\mathcal{V}^{\mathrm{LDA},a,\ell}_{nm;k^b}(z),
\end{aligned} \tag{4.17}$$

In this way we can obtain the contribution from layer ℓ with the knowledge of LDA matrix elements only.

To limit the response to one surface, the equivalent of Eq. (4.15) was proposed in Ref. [44] and later used in Refs. [45], [46], [47], and [48] also in the context of SHG. The layer-by-layer analysis of Refs. [49] and [50] used Eq. (4.1), limiting the current response to a particular layer of the slab and used to obtain the anisotropic linear optical response of semiconductor surfaces. However, the first formal derivation of this scheme is presented in Ref. [51] for the linear response, and here in this chapter, for the optical 2PA response of semiconductors.

From above procedure, we simply take Eq. 2.41 to write that, [52]

$$\begin{aligned}
\mathrm{Im}[\chi^{\ell,\mathrm{abcd}}_{2\omega}] = \frac{\pi e^4}{\hbar^3}\int \frac{d\boldsymbol{k}}{8\pi^3}\sum_{vc}\Bigg(&\frac{16\Delta^{\mathrm{d}}_{cv}(\boldsymbol{k})\mathrm{Im}[r^{\mathrm{c}}_{cv;k^{\mathrm{b}}}(\boldsymbol{k})\mathcal{V}^{\Sigma,\ell,\mathrm{a}}_{vc}(\boldsymbol{k})]}{\omega^4_{cv}(\boldsymbol{k})} - \frac{32\Delta^{\mathrm{b}}_{cv}(\boldsymbol{k})\Delta^{\mathrm{d}}_{cv}(\boldsymbol{k})\mathrm{Im}[\mathcal{V}^{\Sigma,\ell,\mathrm{a}}_{vc}(\boldsymbol{k})r^{\mathrm{c}}_{cv}(\boldsymbol{k})]}{\omega^5_{cv}(\boldsymbol{k})} \\
&- \frac{8\mathrm{Im}[\mathcal{V}^{\Sigma,\ell,\mathrm{a}}_{vc;k^{\mathrm{d}}}(\boldsymbol{k})r^{\mathrm{c}}_{cv;k^{\mathrm{b}}}(\boldsymbol{k})]}{\omega^3_{cv}(\boldsymbol{k})} + \frac{16\Delta^{\mathrm{b}}_{cv}(\boldsymbol{k})\mathrm{Im}\big[r^{\mathrm{c}}_{cv}(\boldsymbol{k})\mathcal{V}^{\Sigma,\ell,\mathrm{a}}_{vc;k^{\mathrm{d}}}(\boldsymbol{k})\big]}{\omega^4_{cv}(\boldsymbol{k})}\Bigg)\delta(\omega_{cv}(\boldsymbol{k}) - 2\omega),
\end{aligned} \tag{4.18}$$

where we have dropped the z argument as it should be understood that the z dependence is actually given by the "position" of the ℓ-th layer. Finally, we calculate the surface susceptibility as

$$\boldsymbol{\chi}^{S}_{2\omega} \equiv \sum_{\ell=1}^{N} \boldsymbol{\chi}^{S,\ell}_{2\omega}, \tag{4.19}$$

where $\ell = 1$ is the first layer right at the surface, and $\ell = N$ is the bulk-like layer at a distance $\sim d$ from the surface as seen in Fig. 4.1, such that

$$\boldsymbol{\chi}^{S,\ell=N}_{2\omega} = \boldsymbol{\chi}^{S,\text{bulk}}_{2\omega}, \tag{4.20}$$

as explained above. We can use Eq. (4.19) for either the front or the back surface. We remark that the value of N is not universal, which means that the slab needs to have enough atomic layers for Eq. (4.20) to be satisfied and at the same time to give converged results for $\boldsymbol{\chi}^{S}_{2\omega}$; in practice though, such value of N may be numerically difficult to achieve and one has to look for a "reasonable" fulfilment of Eq. (4.20).

4.2 Results for Si and GaAs surfaces

To present the 2PA spectroscopy results obtained for surfaces and 2D materials is important to recall that TPA surface susceptibility tensor of Eq. (4.18), considers the same matrix elements as the bulk susceptibility of Eq. (2.41). As described in chapter 3 the only contributing term to 2PA surface susceptibility is ρ^{3}_{eii} circled in Fig. 2.1. This term is 2ω dependent and considers transitions between two bands only. As showed chapter 3, the 1ω along with the three and four band-transitions terms are also negligible for surfaces and 2D materials in the range of interest $E_g/2 < \hbar\omega < E_g$.

The self-consistent ground state and the Kohn-Sham states were calculated in the DFT framework using the plane-wave ABINIT code [35]. In what follows we calculate the results for 2PA using meta-Generalized Gradient Approximation (mGGA) pseudopotentials [42] scheme that as showed in the previous chapter gives the best results. [52]

We used ≈ 1000 $\mathbf{k}$-points in order to have well converged results for the irreducible Brillouin zone (IBZ) integration, as given in Eq. (4.18), using the linear analytic tetrahedron method of Ref. [43]. Also, a cut-off energy of 10 Ha was used for the plane waves, and 30 conduction bands (c) were used for the summations in Eq. (4.18). We calculated 2PA susceptibility for three different surface structures and for four 2D chalcogenide structures using SOC interaction.

In Fig. 4.2 we show the calculated $\text{Im}[\chi^{xxxx}_{2\omega}]$ spectra of GaAs-1×1(110):Sb surface, this material consist of GaAs layer terminated with 2 Sb atoms, in this case we have 12 Ga and 12 As atoms to form the surface. We compare the half-slab calculation of above surface with the bulk calculation for GaAs. The GaAs-1×1(110):Sb surface spectra shows a shifted band-gap to high energies from the bulk spectra, the $E_g/2$ of GaAs bulk is 0.6 eV, and 0.8 eV for the surface. This means, that the gap shift of the surface is 0.4 eV to higher energies. It is remarkable that both spectra are of the same order of magnitude, but there are a noticeable difference between the spectral shape. The bulk calculation presents well localized peak resonances after half band-gap with a thin bandwidth followed by a zone of broad resonances, and finally another resonance after band-gap. Instead, the surface spectra presents a broad resonance that grows slowly forming a broad bandwidth where 2PA

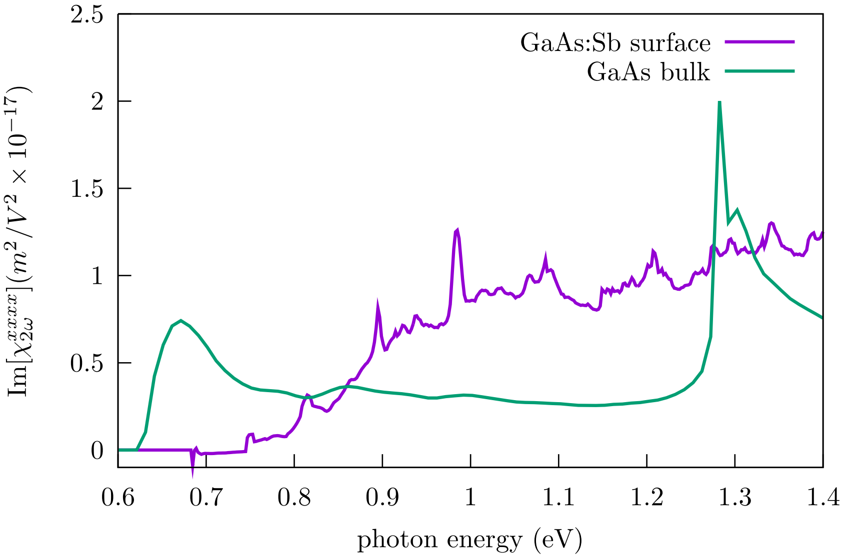

Figure 4.2: Comparison of $\mathrm{Im}[\chi^{xxxx}_{2\omega}]$ between GaAs-1 × 1-(110):Sb surface and bulk calculation. The surface material consist of 12 GaAs layers terminated with Sb atoms.

could be generated in a continuous way with an intensity larger than that of bulk GaAs. Moreover, there are thin local resonances not seen in the bulk material. All in all, this surface has several advantages against bulk structure that could be used for possible scientifical and technological applications.

The $\mathrm{Im}[\chi^{xxxx}_{2\omega}]$ spectrum of a clean GaAs-(1 × 1)-110 surface is presented in Fig. 4.3. In this case there are 22 atoms, which 11 are Ga and 11 are As forming an array with 11 layers. A remarkable difference among the spectra of Fig. 4.3 for GaAs-1 × 1-(110) and that of Fig. 4.2 for GaAs:Sb; for the latter we obtained a 2PA peak-shaped spectrum with a fast growth at the start of the half band-gap (0.06 eV) and a decrease when the energy goes towards the gap. Thus, this surface shows a 2PA spectrum with only one broad resonance. We see that the 2PA maximum intensity for the GaAs clean surface is ~ 20 and ~ 33 larger than that of GaAs bulk and GaAs:Sb surface respectively; moreover is the largest 2PA intensity of all the surfes studied in this thesis. Additionally, the bandwidth of GaAs clean surface is very small ~ 0.02 eV and falls in an energy range that corresponds to the tera Hertz (THz) spectral region from 0.06 eV to 0.18 eV; the use of THz will be very convenient for non-invasive 2PA medical applications.

In Fig. 4.4 the corresponding results for Si bulk and the Si-1×1(111):H surface are presented. The Si surface structure consists of 14 layers of which the top and bottom atoms are H, the remaining 12 layers are Si. Indeed, H passivates the Si surface atoms thus rendering a “bulk-like” surface structure. In this case, the band-gap of both bulk and surface starts at 2.84 eV, and thus they have the same half-band gap. The Si bulk spectra is explained in chapter 3, and here we only contrasted it with the surface 2PA calculation. The bulk spectra has a big maximum just above the half-band gap besides several resonances at higher energies, instead the surface spectra shows

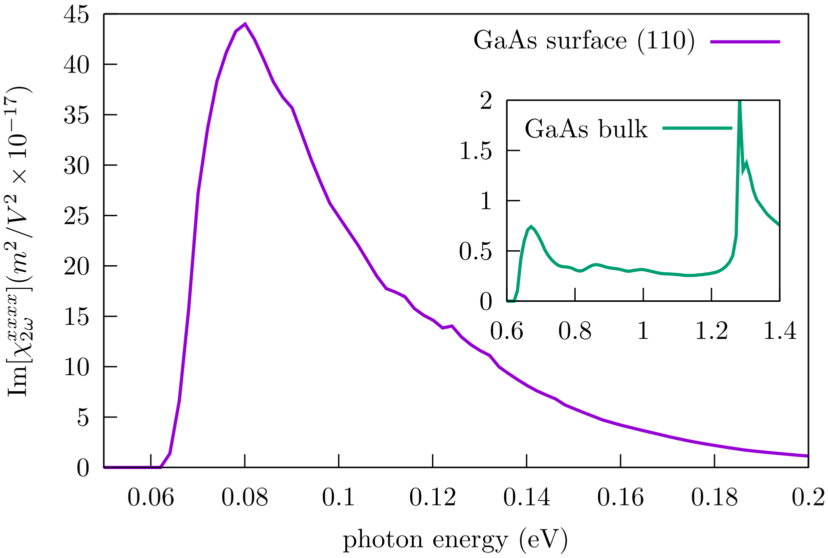

Figure 4.3: $\mathrm{Im}[\chi_{2\omega}^{xxxx}]$ of GaAs (110) clean surface. The surface material consists of 11 layers of GaAs (110). To compare between magnitude of response a inset of GaAs bulk is shown.

a broad resonance of almost the same intensity. We notice that the intensity of surface and bulk responses have the same order of magnitude above 1.8 eV. Additionally, is important to note the large bandwidth of surface spectra, which have a slow decrease when photon energy is near of E_g, is also presented in all bulk calculations as expected.

Last but not least, in Fig. 4.5 the calculations of 2PA susceptibility for 2D chalcogenides are presented. The studied materials are GeS, GeSe, SnS and SnSe, this group of materials have a range of $\mathrm{Im}[\chi_{2\omega}^{xxxx}]$ magnitudes that goes from 50 to 5 $\mathrm{m}^2/\mathrm{V}^2 \times 10^{-18}$, being the biggest intensity for GeSe mono-layer. Also, in Fig. 4.5 the spectra of bulk Si and bulk GaAs are presented in order to compare them with the results of the mono-layer 2D chalcogenides. We see that the 2D chalcogenides present a more complex 2PA spectra, this means that the spectrum have several intense and localized resonances. This behaviour comes from the complex electronic band structure of these materials. The susceptibility spectra of the 2D chalcogenides cover the range from ∼0.6 to ∼3.5 eV allowing to use of this wide spectral range in potential 2PA nano-optoelectronic applications.

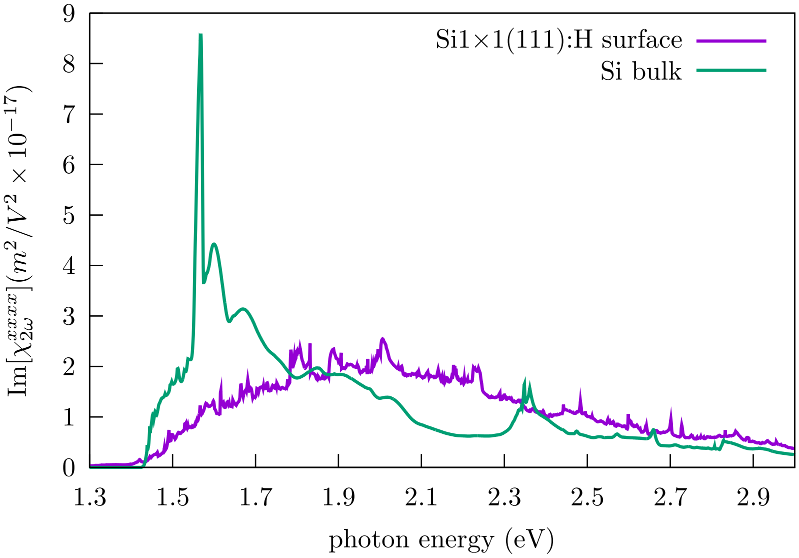

Figure 4.4: Comparison of $\mathrm{Im}[\chi^{xxxx}_{2\omega}]$ between Si1×1(111):H surface and bulk calculation. The surface material consist of 12 Si array terminated with H is presented.

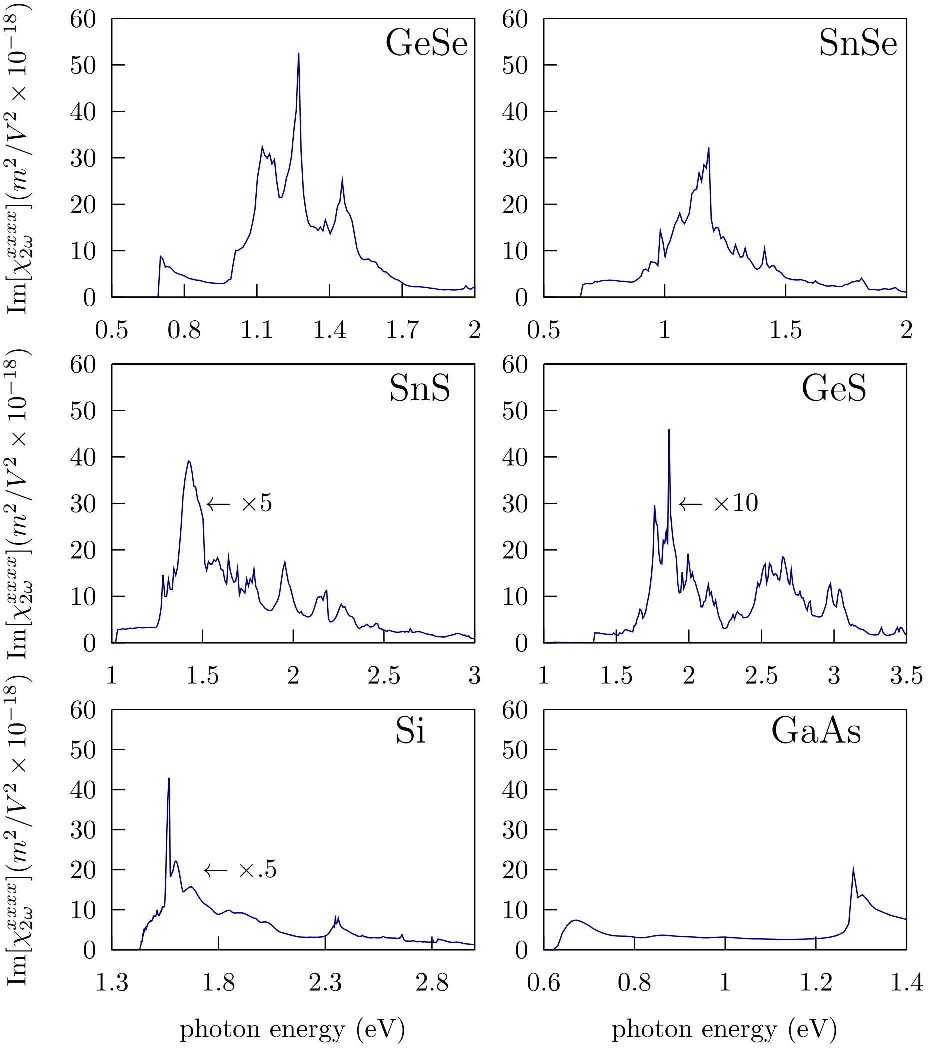

Figure 4.5: Calculations of $\mathrm{Im}[\chi_{2\omega}^{xxxx}]$ for mono-layer SnS, SnSe, GeS and GeSe chalcogenide materials. For comparison, we also show the spectra of bulk Si without the scissors shift and bulk GaAs of Fig. 3.3.

5 Conclusion

With the independent-particle approach, we have presented a theoretical derivation of two-photon absorption (2PA) from semiconductors based on the length gauge formalism, where the contribution of the *intraband* $\boldsymbol{r}_i$ part and the *interband* $\boldsymbol{r}_e$ part of the position operator $\boldsymbol{r}$ are properly accounted for and the scissors operator is included. Using time-reversal symmetry, we obtained an expression for $\chi^{\mathrm{abcd}}(-\omega;-\omega,-\omega,\omega)$ that avoids nonphysical divergences presented in previous calculations when $\omega \to 0$ [1]. Within the independent-particle approximation, *ab initio* band structure calculations using several pseudopotential schemes that include the SOC interaction were used to calculate the 2PA coefficient, $\beta_{11}^{\|}(\omega)$, below the band gap of several semiconductors. In particular the $\beta_{11}^{\|}(\omega)$ was calculated for GaAs, Si and GaP, and compared with available experimental results. Using different values of the scissors correction, we were able to reproduce the experimental results qualitatively, showing that our calculations follow the trend of the experimental spectra signatures reported in GaAs and Si, giving a resonant behavior in the spectrum of $\beta_{11}^{\|}(\omega)$ for $E_{g/2} < \hbar\omega < E_g$. The spectrum reported for GaAs mainly comes from the last valence band to the first conduction band around the Γ point of the IBZ; in contrast, for Si there are transitions from the second, third, and fourth valence bands to the second, third, fourth, and fifth conduction bands, which are spread over the IBZ, in particular, along the Γ-X path, thus explaining the complexity of the 2PA spectrum for this material. Moreover, the 2ω and 1ω terms of $\chi^{\mathrm{abcd}}(-\omega;-\omega,-\omega,\omega)$ are analyzed to obtain a complete third-order optical response. The position matrix elements are distinguished in the *intraband* r_i part and the *interband* r_e part, allowing us to disregard numerically negligible terms in $\chi^{\mathrm{abcd}}(-\omega;-\omega,-\omega,\omega)$ that come from three- and four-band transitions. Additionally, we formulated the theoretical derivation for surface 2PA susceptibility, that includes the correct implementation of cut function to obtain the surface response. We calculated 2PA susceptibility for three surface structures GaAs-1×1(110):Sb, Si-1×1(111):H and clean GaAs-1×1-(110). We obtained the 2PA susceptibility spectra in the range of $E_g/2 < \hbar\omega E_g$ and compared the surface spectra with the corresponding bulk calculations. We found a remarkable widening of bandwidth for GaAs-1×1(110):Sb and Si-1×1(111):H structures compared with the corresponding bulk response, and for clean GaAs-1×1-(110) surface the spectral shape shows a resonance in the tera-Hertz region which enables the use of this material in non-invasive medical applications. Moreover, we calculated the 2PA susceptibility for four 2D materials: GeSe, SnSe, SnS and GeS, such materials are commonly used in optoelectronic devices and our study motivates the experimental investigation of 2PA of 2D structures. To strengthen our results, a full GW calculation, which goes beyond the scissors approximation, would be able to produce a band structure that, through our expression for $\chi^{\mathrm{abcd}}(-\omega;-\omega,-\omega,\omega)$, could match the experiment on firmer grounds; however, the large number of **k** points needed to achieve convergence (∼60 000) represents a numerical challenge in its own terms. Moreover, it would be desirable to go beyond the independent-particle approximation and develop the 2PA theory including the electron-hole interaction. However, including the electron-hole interaction even for the linear response is a very demanding problem, not only with regard to the theoretical part, but also with regard to the numerical computation, as described in Refs. [30, 53]; this would constitute a very challenging problem that ought to be pursued in the future. Nonetheless, our results show the correct order of magnitude and spectral features with which an adequate semiconductor could be chosen for myriad of applications of 2PA. Thus our predictions of 2PA that cover both a wide spectral range and a wide intensity range for the semiconductors which are commonly used in semiconductor technology will certainly motivate 2PA experimental investigation for these materials.

Final Remarks

In closing, we want to emphasize the main contributions of this thesis. First of all, an unprecedented theoretical derivation of 2PA for bulk and surface materials was presented. For Si, GaAS and GaP semiconductors the comparison with experimental data of calculated spectroscopy is presented, and was found that the results from our derived theory compares quite well to the experimental spectra. To the best of our knowledge, our *ab initio* calculations are the most accurate up to date, and, for some materials it is the first time that a calculation like this has been presented. Consequently, our results of 2PA that cover both a wide spectral range and a wide intensity range for the semiconductors will certainly motivate 2PA experimental investigation for these materials. Even more, our predictions suggest which materials with the best 2PA characteristics could be used in the development of scientific and technological applications. Finally, as future prospects, we are going to calculate 2PA for other crystalline structures besides FCC, extending the calculation to more types semiconductors, and we intend to extend the calculation to the nonlinear third order susceptibility in order to obtain the nonlinear refractive index.

A Scissors renormalization for $\boldsymbol{\mathcal{V}}^{\Sigma}_{nm}$

To re-normalize $\boldsymbol{\mathcal{V}}^{\Sigma}_{nm}$ we start applying the cut function to position operator matrix elements, then

$$\begin{aligned}\langle n\mathbf{k}|\,\mathcal{C}(z)\mathbf{r}\,|m\mathbf{k}\rangle\,(E^{\Sigma}_{m}-E^{\Sigma}_{n}) &= \int d\mathbf{r}\,\psi^{*}_{n\mathbf{k}}(\mathbf{r})\mathcal{C}(z)\mathbf{r}(E^{\Sigma}_{m}-E^{\Sigma}_{n})\psi_{m\mathbf{k}}(\mathbf{r})\\ &= \int d\mathbf{r}\,\psi^{*}_{n\mathbf{k}}(\mathbf{r})\mathcal{C}(z)[\mathbf{r},H^{\Sigma}]\psi_{m\mathbf{k}}(\mathbf{r})\\ &= -i\int d\mathbf{r}\,\psi^{*}_{n\mathbf{k}}(\mathbf{r})\mathcal{C}(z)\mathbf{v}^{\Sigma}\psi_{m\mathbf{k}}(\mathbf{r}),\end{aligned} \tag{A.1}$$

since $(E^{\Sigma}_{m}-E^{\Sigma}_{n})=\omega^{\Sigma}_{mn}$ then

$$\langle n\mathbf{k}|\,\mathcal{C}(z)\mathbf{r}\,|m\mathbf{k}\rangle = i\frac{\boldsymbol{\mathcal{V}}^{\Sigma}_{nm}}{\omega^{\Sigma}_{nm}}, \tag{A.2}$$

we do the same for LDA electron position elements

$$\begin{aligned}\langle n\mathbf{k}|\,\mathcal{C}(z)\mathbf{r}\,|m\mathbf{k}\rangle\,(E^{\mathrm{LDA}}_{m}-E^{\mathrm{LDA}}_{n}) &= \int d\mathbf{r}\,\psi^{*}_{n\mathbf{k}}(\mathbf{r})\mathcal{C}(z)\mathbf{r}(E^{\mathrm{LDA}}_{m}-E^{\mathrm{LDA}}_{n})\psi_{m\mathbf{k}}(\mathbf{r})\\ &= \int d\mathbf{r}\,\psi^{*}_{n\mathbf{k}}(\mathbf{r})\mathcal{C}(z)[\mathbf{r},H^{\mathrm{LDA}}]\psi_{m\mathbf{k}}(\mathbf{r})\\ &= -i\int d\mathbf{r}\,\psi^{*}_{n\mathbf{k}}(\mathbf{r})\mathcal{C}(z)\mathbf{v}^{\mathrm{LDA}}\psi_{m\mathbf{k}}(\mathbf{r}),\end{aligned} \tag{A.3}$$

then

$$\langle n\mathbf{k}|\,\mathcal{C}(z)\mathbf{r}\,|m\mathbf{k}\rangle = i\frac{\boldsymbol{\mathcal{V}}^{\mathrm{LDA}}_{nm}}{\omega^{\mathrm{LDA}}_{nm}}, \tag{A.4}$$

comparing Eq. A.2 and Eq. A.4 we find

$$\boldsymbol{\mathcal{V}}^{\Sigma}_{nm} = \frac{\omega^{\Sigma}_{nm}}{\omega^{\mathrm{LDA}}_{nm}}\boldsymbol{\mathcal{V}}^{\mathrm{LDA}}_{nm}. \tag{A.5}$$

B DISCLAIMER

Part of the contents of this thesis are based on the article
Ab initio calculation of two-photon absorption in semiconductors,
by Alan Bernal Ramírez and Bernardo S. Mendoza,
published in Physical Review B **106**, 125201 (2022).

The "Reuse and Permissions License" granted by the American Physical Society on 17-Nov-2022 is reproduced in the next two pages.

American Physical Society
Reuse and Permissions License

17-Nov-2022

This license agreement between the American Physical Society ("APS") and Bernardo Mendoza Santoyo ("You") consists of your license details and the terms and conditions provided by the American Physical Society and SciPris.

Licensed Content Information

License Number:	**RNP/22/NOV/060115**
License date:	17-Nov-2022
DOI:	10.1103/PhysRevB.106.125201
Title:	Ab initio calculation of two-photon absorption in semiconductors
Author:	Alan Bernal Ramírez and Bernardo S. Mendoza
Publication:	Physical Review B
Publisher:	American Physical Society
Cost:	USD $ 0.00

Request Details

Does your reuse require significant modifications: No

Specify intended distribution locations:	Worldwide
Reuse Category:	Reuse in a thesis/dissertation
Requestor Type:	Author of requested content
Items for Reuse:	Whole Article
Format for Reuse:	Print and Electronic
Total number of print copies:	Up to 1000

Information about New Publication:

University/Publisher:	Centro de Investigaciones en Óptica, A.C/
Title of dissertation/thesis:	Ab-initio calculation of two-photon absorption for semiconductors
Author(s):	Alan Bernal Ramírez
Expected completion date:	Dec. 2022

License Requestor Information

Name:	Bernardo Mendoza Santoyo
Affiliation:	Individual
Email Id:	bms@cio.mx
Country:	Mexico

American Physical Society
Reuse and Permissions License

TERMS AND CONDITIONS

The American Physical Society (APS) is pleased to grant the Requestor of this license a non-exclusive, non-transferable permission, limited to Print and Electronic format, provided all criteria outlined below are followed.

1. You must also obtain permission from at least one of the lead authors for each separate work, if you haven't done so already. The author's name and affiliation can be found on the first page of the published Article.
2. For electronic format permissions, Requestor agrees to provide a hyperlink from the reprinted APS material using the source material's DOI on the web page where the work appears. The hyperlink should use the standard DOI resolution URL, http://dx.doi.org/{DOI}. The hyperlink may be embedded in the copyright credit line.
3. For print format permissions, Requestor agrees to print the required copyright credit line on the first page where the material appears: "Reprinted (abstract/excerpt/figure) with permission from [(FULL REFERENCE CITATION) as follows: Author's Names, APS Journal Title, Volume Number, Page Number and Year of Publication.] Copyright (YEAR) by the American Physical Society."
4. Permission granted in this license is for a one-time use and does not include permission for any future editions, updates, databases, formats or other matters. Permission must be sought for any additional use.
5. Use of the material does not and must not imply any endorsement by APS.
6. APS does not imply, purport or intend to grant permission to reuse materials to which it does not hold copyright. It is the requestor's sole responsibility to ensure the licensed material is original to APS and does not contain the copyright of another entity, and that the copyright notice of the figure, photograph, cover or table does not indicate it was reprinted by APS with permission from another source.
7. The permission granted herein is personal to the Requestor for the use specified and is not transferable or assignable without express written permission of APS. This license may not be amended except in writing by APS.
8. You may not alter, edit or modify the material in any manner.
9. You may translate the materials only when translation rights have been granted.
10. APS is not responsible for any errors or omissions due to translation.
11. You may not use the material for promotional, sales, advertising or marketing purposes.
12. The foregoing license shall not take effect unless and until APS or its agent, Aptara, receives payment in full in accordance with Aptara Billing and Payment Terms and Conditions, which are incorporated herein by reference.
13. Should the terms of this license be violated at any time, APS or Aptara may revoke the license with no refund to you and seek relief to the fullest extent of the laws of the USA. Official written notice will be made using the contact information provided with the permission request. Failure to receive such notice will not nullify revocation of the permission.
14. APS reserves all rights not specifically granted herein.
15. This document, including the Aptara Billing and Payment Terms and Conditions, shall be the entire agreement between the parties relating to the subject matter hereof.

BIBLIOGRAPHY

[1] Misao Murayama and Takashi Nakayama. Ab initio calculations of two-photon absorption spectra in semiconductors. *Physical Review B*, 52(7):4986–4997, August 1995.

[2] Brandon J. Furey, Rodrigo M. Barba-Barba, Ramon Carriles, Alan Bernal, Bernardo S. Mendoza, and Michael C. Downer. Im$\chi^{(3)}$ spectra of 110-cut GaAs, GaP, and Si near the two-photon absorption band edge. *Journal of Applied Physics*, 129(18):183109, May 2021. Publisher: American Institute of Physics.

[3] M.D. Dvorak, W.A. Schroeder, D.R. Andersen, A.L. Smirl, and B.S. Wherrett. Measurement of the anisotropy of two-photon absorption coefficients in zincblende semiconductors. *IEEE Journal of Quantum Electronics*, 30(2):256–268, 1994.

[4] D. H. Reitze, T. R. Zhang, Wm. M. Wood, and M. C. Downer. Two-photon spectroscopy of silicon using femtosecond pulses at above-gap frequencies. *J. Opt. Soc. Am. B*, 7(1):84–89, Jan 1990.

[5] Sean M. Anderson, Nicolas Tancogne-Dejean, Bernardo S. Mendoza, and Valérie Véniard. Theory of surface second-harmonic generation for semiconductors including effects of nonlocal operators. *Phys. Rev. B*, 91:075302, Feb 2015.

[6] Melvin J. Lax. *Symmetry principles in solid state and molecular physics / Melvin Lax.* Wiley, New York, 1974.

[7] Maria Göppert-Mayer. Über elementarakte mit zwei quantensprüngen. *Annalen der Physik*, 401(3):273–294, 1931. https://onlinelibrary.wiley.com/doi/pdf/10.1002/andp.19314010303.

[8] W. Denk, J. H. Strickler, and W. W. Webb. Two-photon laser scanning fluorescence microscopy. *Science*, 248(4951):73–76, April 1990.

[9] En-Shinn Wu, James H. Strickler, W. R. Harrell, and Watt W. Webb. Two-photon lithography for microelectronic application. In John D. Cuthbert, editor, *Optical/Laser Microlithography V*, volume 1674, pages 776 – 782. International Society for Optics and Photonics, SPIE, 1992.

[10] Shoji Maruo, Osamu Nakamura, and Satoshi Kawata. Three-dimensional microfabrication with two-photon-absorbed photopolymerization. *Optics Letters*, 22(2):132–134, January 1997. Publisher: Optical Society of America.

[11] S Kawata, HB. Sun, T Tanaka, and K Takada. Finer features for functional microdevices. *Nature*, 412(6848):697–698, August 2001.

[12] Lee W. Tutt and Thomas F. Boggess. A review of optical limiting mechanisms and devices using organics, fullerenes, semiconductors and other materials. *Progress in Quantum Electronics*, 17(4):299–338, January 1993.

[13] Dimitri A. Parthenopoulos and Peter M. Rentzepis. Three-Dimensional Optical Storage Memory. *Science*, 245(4920):843–845, August 1989. Publisher: American Association for the Advancement of Science.

[14] Kazuya Ogawa. Two-photon absorbing molecules as potential materials for 3d optical memory. *Applied Sciences*, 4(1):1–18, 2014.

[15] Julie Schmitt, Valérie Heitz, Angélique Sour, Frédéric Bolze, Hussein Ftouni, Jean-Francois Nicoud, Lucia Flamigni, and Barbara Ventura. Diketopyrrolopyrrole-porphyrin conjugates with high two-photon absorption and singlet oxygen generation for two-photon photodynamic therapy. *Angewandte Chemie International Edition*, 54(1):169–173, 2015.

[16] Brandon J. Furey, Benjamin J. Stacy, Tushti Shah, Rodrigo M. Barba-Barba, Ramon Carriles, Alan Bernal, Bernardo S. Mendoza, Brian A. Korgel, and Michael C. Downer. Two-Photon Excitation Spectroscopy of Silicon Quantum Dots and Ramifications for Bio-Imaging. *ACS Nano*, 16(4):6023–6033, April 2022. Publisher: American Chemical Society.

[17] Ke Wei, Zhongjie Xu, Runze Chen, Xin Zheng, Xiangai Cheng, and Tian Jiang. Temperature-dependent excitonic photoluminescence excited by two-photon absorption in perovskite $CsPbBr_3$ quantum dots. *Opt. Lett.*, 41(16):3821–3824, Aug 2016.

[18] T Ogawa and Y Kanemitsu. *Optical Properties of Low–Dimensional Materials*. WORLD SCIENTIFIC, January 1996.

[19] D. C. Hutchings and E. W. Van Stryland. Nondegenerate two-photon absorption in zinc blende semiconductors. *JOSA B*, 9(11):2065–2074, November 1992. Publisher: Optical Society of America.

[20] Claudio Aversa, J. E. Sipe, M. Sheik-Bahae, and E. W. Van Stryland. Third-order optical nonlinearities in semiconductors: The two-band model. *Physical Review B*, 50(24):18073–18082, December 1994.

[21] D. C. Hutchings and B. S. Wherrett. Theory of the Polarization Dependence of Two-photon Absorption in Zinc-blende Semiconductors. *Journal of Modern Optics*, 41(6):1141–1149, June 1994.

[22] D. C. Hutchings and B. S. Wherrett. Theory of anisotropy of two-photon absorption in zinc-blende semiconductors. *Physical Review B*, 49(4):2418–2426, January 1994. Publisher: American Physical Society.

[23] Claudio Aversa and J. E. Sipe. Nonlinear optical susceptibilities of semiconductors: Results with a length-gauge analysis. *Phys. Rev. B*, 52:14636–14645, Nov 1995.

[24] James L. P. Hughes and J. E. Sipe. Calculation of second-order optical response in semiconductors. *Physical Review B*, 53(16):10751–10763, April 1996. Publisher: American Physical Society.

[25] M. Murayama and T. Nakayama. Two-photon-absorption spectra originating from higher-energy transitions. *Physical Review B*, 49(8):5737–5740, February 1994. Publisher: American Physical Society.

[26] Misao Murayama and Takashi Nakayama. Symmetry-induced anisotropy of two-photon absorption spectra in zinc-blende semiconductors. *Physical Review B*, 55(15):9628–9636, April 1997.

[27] W.-R. Hannes and T. Meier. Higher-order contributions and nonperturbative effects in the nondegenerate nonlinear optical absorption of semiconductors using a two-band model. *Phys. Rev. B*, 99:125301, Mar 2019.

[28] D. J. Passos, G. B. Ventura, J. M. B. Lopes dos Santos, and J. M. Viana Parente Lopes. Nonlinear optical conductivity of a two-band crystal I. *Journal of Physics: Condensed Matter*, 33(46):465701, August 2021. Publisher: IOP Publishing.

[29] Indeed, the factor of 3 arises from the sum over the allowed frequency permutations as obtained from Eq. (2.3).

[30] Giovanni Onida, Lucia Reining, and Angel Rubio. Electronic excitations: density-functional versus many-body green's-function approaches. *Rev. Mod. Phys.*, 74:601–659, Jun 2002.

[31] E. N. Adams. The crystal momentum as a quantum mechanical operator. *The Journal of Chemical Physics*, 21(11):2013–2017, 1953.

[32] E. I. Blount, F. Seitz, and D. Turnbull. Solid state physics. *Advances in Research and Applications*, 13:305, 1962.

[33] Bernardo S. Mendoza and W. Luis Mochán. Ab initio theory of the drude plasma frequency. *J. Opt. Soc. Am. B*, 38(6):1918–1926, Jun 2021.

[34] J. L. Cabellos, Bernardo S. Mendoza, M. A. Escobar, F. Nastos, and J. E. Sipe. Effects of nonlocality on second-harmonic generation in bulk semiconductors. *Phys. Rev. B*, 80:155205, Oct 2009.

[35] The ABINIT code is a common project of the Universitè Catholique de Louvain, Corning Incorporated, and other contributors (URL http://www.abinit.org). Xavier Gonze, Bernard Amadon, Gabriel Antonius, Frédéric Arnardi, Lucas Baguet, Jean-Michel Beuken, Jordan Bieder, François Bottin, Johann Bouchet, Eric Bousquet, Nils Brouwer, Fabien Bruneval,

Guillaume Brunin, Théo Cavignac, Jean-Baptiste Charraud, Wei Chen, Michel Côté, Stefaan Cottenier, Jules Denier, Grégory Geneste, Philippe Ghosez, Matteo Giantomassi, Yannick Gillet, Olivier Gingras, Donald R. Hamann, Geoffroy Hautier, Xu He, Nicole Helbig, Natalie Holzwarth, Yongchao Jia, François Jollet, William Lafargue-Dit-Hauret, Kurt Lejaeghere, Miguel A. L. Marques, Alexandre Martin, Cyril Martins, Henrique P. C. Miranda, Francesco Naccarato, Kristin Persson, Guido Petretto, Valentin Planes, Yann Pouillon, Sergei Prokhorenko, Fabio Ricci, Gian-Marco Rignanese, Aldo H. Romero, Michael Marcus Schmitt, Marc Torrent, Michiel J. van Setten, Benoit Van Troeye, Matthieu J. Verstraete, Gilles Zérah, Josef W. Zwanziger, Comput. Phys. Commun., **248**, 107042 (2020); Aldo H. Romero, Douglas C. Allan, Bernard Amadon, Gabriel Antonius, Thomas Applencourt, Lucas Baguet, Jordan Bieder, François Bottin, Johann Bouchet, Eric Bousquet, Fabien Bruneval, Guillaume Brunin, Damien Caliste, Michel Côté, Jules Denier, Cyrus Dreyer, Philippe Ghosez, Matteo Giantomassi, Yannick Gillet, Olivier Gingras, Donald R. Hamann, Geoffroy Hautier, François Jollet, Gérald Jomard, Alexandre Martin, Henrique P. C. Miranda, Francesco Naccarato, Guido Petretto, Nicholas A. Pike, Valentin Planes, Sergei Prokhorenko, Tonatiuh Rangel, Fabio Ricci, Gian-Marco Rignanese, Miquel Royo, Massimiliano Stengel, Marc Torrent, Michiel J. van Setten, Benoit Van Troeye, Matthieu J. Verstraete, Julia Wiktor, Josef W. Zwanziger, Xavier Gonze J. Chem. Phys., **152**, 124102 (2020).

[36] N. Troullier and José Luís Martins. Efficient pseudopotentials for plane-wave calculations. *Phys. Rev. B*, 43:1993–2006, Jan 1991.

[37] Leonard Kleinman and D. M. Bylander. Efficacious form for model pseudopotentials. *Phys. Rev. Lett.*, 48:1425–1428, May 1982.

[38] C. Hartwigsen, S. Goedecker, and J. Hutter. Relativistic separable dual-space gaussian pseudopotentials from h to rn. *Phys. Rev. B*, 58:3641–3662, Aug 1998.

[39] John P. Perdew. Density-functional approximation for the correlation energy of the inhomogeneous electron gas. *Phys. Rev. B*, 33(12):8822–8824, June 1986.

[40] G. Ortiz and P. Ballone. Correlation energy, structure factor, radial distribution function, and momentum distribution of the spin-polarized uniform electron gas. *Phys. Rev. B*, 50(3):1391–1405, July 1994.

[41] G. Ortiz and P. Ballone. Erratum: Correlation energy, structure factor, radial distribution function, and momentum distribution of the spin-polarized uniform electron gas [Phys. rev. b50, 1391 (1994)]. *Phys. Rev. B*, 56(15):9970–9970, October 1997.

[42] E. Räsänen, S. Pittalis, and C. R. Proetto. Universal correction for the becke–Johnson exchange potential. *The Journal of Chemical Physics*, 132(4):044112, January 2010.

[43] F. Nastos, J. Rioux, M. Strimas-Mackey, Bernardo S. Mendoza, and J. E. Sipe. Full band structure LDA and $\mathbf{k} \cdot \mathbf{p}$ calculations of optical spin-injection. *Phys. Rev. B*, 76:205113, Nov 2007.

[44] Lucia Reining, R. Del Sole, M. Cini, and Jiang Guo Ping. Microscopic calculation of second-harmonic generation at semiconductor surfaces: As/Si(111) as a test case. *Physical Review B*, 50(12):8411–8422, 1994-09-15.

[45] B. S. Mendoza, A. Gaggiotti, and R. Del Sole. Microscopic theory of second harmonic generation at Si(100) surfaces. *Physical Review Letters*, 81(17):3781–3784, 1998.

[46] Bernardo S. Mendoza, Maurizia Palummo, Giovanni Onida, and Rodolfo Del Sole. Ab initio calculation of second-harmonic-generation at the Si(100) surface. *Physical Review B*, 63(20):205406, 2001-04-18.

[47] H. Sano, G. Mizutani, W. Wolf, and R. Podloucky. Ab initio study of linear and nonlinear optical responses of Si(111) surfaces. *Phys. Rev. B*, 66:195338, Nov 2002.

[48] J. E. Mejía, B.S. Mendoza, and C. Salazar. Layer-by-layer analysis of second harmonic generation at a simple surface. *Revista Mexicana de Física*, 50(2):134–139, 2004.

[49] Conor Hogan, Rodolfo Del Sole, and Giovanni Onida. Optical properties of real surfaces from microscopic calculations of the dielectric function of finite atomic slabs. *Physical Review B*, 68(3):035405, 2003-07-01.

[50] C. Castillo, Bernardo S. Mendoza, W. G. Schmidt, P. H. Hahn, and F. Bechstedt. Layer-by-layer analysis of surface reflectance anisotropy in semiconductors. *Physical Review B*, 68(4):041310, 2003-07-30.

[51] Bernardo Mendoza, F. Nastos, N. Arzate, and J. Sipe. Layer-by-layer analysis of the linear optical response of clean and hydrogenated Si(100) surfaces. *Physical Review B*, 74(7):075318, 2006-08.

[52] Alan Bernal Ramírez and Bernardo S. Mendoza. Ab initio calculation of two-photon absorption in semiconductors. *Phys. Rev. B*, 106:125201, Sep 2022.

[53] Sean M. Anderson, Bernardo S. Mendoza, Giorgia Fugallo, and Francesco Sottile. Plasmon dispersion in graphite: A comparison of current ab initio methods. *Phys. Rev. B*, 100:045205, Jul 2019.